Development and characterization of a microscope based on pump-probe spectroscopy: A valuable tool for the study of photoactivated drugs *in cellulo*

seit 1558

Friedrich-Schiller-Universität Jena

Dissertation

zur Erlangung des akademischen Grades doctor rerum naturalium
(Dr. rer. nat.)

vorgelegt dem Rat der Chemisch-Geowissenschaftliche Fakultät der
Friedrich-Schiller-Universität Jena

von M.Sc. Alejandro De la Cadena
Pérez-Gallardo

Gutachter:

1. .....
2. .....
3. .....

Tag der Verteidigung: .....

"The seeker after the truth is not one who studies the writings of the ancients and, following his natural disposition, puts his trust in them, but rather the one who suspects his faith in them and questions what he gathers from them, the one who submits to argument and demonstration, and not to the sayings of a human being whose nature is fraught with all kinds of imperfection and deficiency. Thus the duty of the man who investigates the writings of scientists, if learning the truth is his goal, is to make himself an enemy of all that he reads, and, applying his mind to the core and margins of its content, attack it from every side. He should also suspect himself as he performs his critical examination of it, so that he may avoid falling into either prejudice or leniency."

Al Haytham

Table of contents

List of figures

Chapter 1

Introduction

A trend in the history of science is the development and/or exploitation of the ideas, concepts and theories of certain scientific field to satisfy the demands of another one which at first glance might not appear related at all, e.g. the estimation of the age of earth by geology to provide support to evolutionary ideas in biology in the end of the nineteenth century [1]. By the time this manuscript was written, this trend is recognized in the necessity of the field of pharmaceutical medicine of new tools and techniques for the study of newly developed drugs and cellular markers synthesized in response to the necessity to counteract the so called *civilization diseases* that afflict modern (and mainly developed) societies. In this thesis the reader will not find the description of the synthesis of a panacea or a lumophore with an incredible quantum yield and zero cytotoxic effects but a way to observe - at least in code - how an alien chemical species to cells when introduced into such cells interacts, evolves and is affected by the complex cellular environment. This acquired knowledge can be complemented by the possibility to determine in which cellular compartment the probed drug, which might or not be endowed with emissive states, is allocated.

During the 1960s the ability of *cis*-platin to hinder DNA replication by forming DNA adducts inducing the activation of apoptosis was systematically recognized [2]. The effectiveness of Platinum-based drugs against some types of cancer [3], together with the induced side effects [4], motivated the study and development of alternative anti-cancer drugs based on metal complexes others than Platinum-based ones and, in some cases, aiming not only to DNA but proteins as target structures [5–15]. In this context, a sub-branch of the modern medicinal inorganic chemistry arose, focusing its efforts on the development of drugs activated by light, i.e. the so called photoactivated chemotherapy [16], where, in principle, both spatial and temporal control over the cytotoxicity of the drug is achieved by triggering a set of chemical reactions upon photoexcitation. In this way, the reactive species would be confined only to illuminated regions and restricted in time by the interval

the reachable molecules are exposed to the light source. This method has shown notoriety as anticancer treatment for its respectable effectiveness and reduced side effects. Moreover, the versatility of metal complexes in the biosciences is revealed when such complexes are chemically "tuned", resulting in non-toxic and strong emissive species, whose localization over the cellular compartments can be controlled with their ligand fields, showing some advantages over standard organic cellular markers, which enable them as potential candidates for targeting biomolecules, as for example DNA [17].

The advent of the development of photoactivated chemotherapeutic agents and emissive probes based on metal complexes demands tools and techniques capable to provide a glimpse on the first events after photoexcitation in the very final target site of the drugs, i.e. the cell, in order to understand how the local environment would affect the molecular physics of the drug and therefore its properties as either lumophore or therapeutic agent. Optical microscopic techniques are key elements on the mentioned research field to record noninvasively the compartments where the drugs are preferentially located inside the cells. Such information is of vital importance for the characterization of the drug, since it can provide support to determine which path the drugs take, how the cells uptake them and of course where they accumulate the most. In addition, for therapeutic agents, knowledge of the spatial distribution of the drug inside the cell can facilitate the determination of its action mechanism against certain pathogens. Modern optical systems are capable to routinely reach the diffraction limit (ca. $\lambda/2$) providing images with exquisite high detail of individual compartments of cells. The most relevant techniques regarding spatial resolution, i.e. practically below the Abbe limit, are: saturated structural illumination microscopy [18], reversible saturable optical linear fluorescence transitions microscopy [19], stimulated emission depletion microscopy [20], evanescence or near field microscopy [21] and photoactivated localization microscopy [22]. These set of novel and outstanding microscopy techniques can indeed be used to determine where the drugs are allocated in the cells if (and only if) the drugs are emissive species. This situation turns problematic for the research of drugs whose final application is to serve as therapeutic agents rather than just stain certain compartments of cells: the researcher would remain blind, in terms of cellular localization of the investigated drug. In addition, such techniques would explore only the relaxation of excited molecules from their emissive state to their corresponding ground state, providing no hints on how the complex cellular environment might affect the physics of the drugs along the entire excited-state topology. Thus, to observe how the dye evolves in time after photoexcitation as function of its location inside the cell, the optical microscope needs to be equipped with all the necessary instrumentation to enable it with time resolved capabilities.

A practical way to obtain this system is to combine a laser scanning microscope (LSM) with the simplest of all the time resolved nonlinear techniques: pump-probe spectroscopy. In such a way, the most notorious characteristics of the mentioned techniques, i.e. the (relative) high spatial resolution of the LSM and the high temporal resolution of the pump-probe spectroscopy, produce a hybrid and powerful tool capable to image doped cells with chemical contrast as function of time. The TAM (acronym of transient absorption microscope) allows the researcher to performed pointillistic pump-probe spectroscopy on the target site of the drug, studying solely the molecules confined in the volume conformed by the pump and probe beams in the focal point of the microscope, resulting -in most cases- in kinetics traces drastically different to corresponding experiments performed with the standard pump-probe set-up in solution.

The work at hand presents the description of the construction and characterization of a microscope mixed with the nonlinear pump-probe technique and its application in the study of photoactivated chemotherapeutic agents and lumophores based on Ruthenium(II) polypyridine complexes *in cellulo*. The results obtained with such a system show how powerful and useful is to imaging eukaryotic cells doped with emissive and non-emissive species, with the possibility to keep record of the ultrafast evolution of photoexcited molecules. Thus, over the pages of this work it can be recognized that both the results presented and the TAM are references for incoming applications, e.g. the ultrafast study of metal-based complexes *in cellulo* and the hybridization of super-resolution microscopic techniques with transient absorption spectroscopy.

This thesis is structured in the following way. An introduction to the subject discussed in this thesis was given to communicate the motivation of this work, see Chapter 1. A complete chapter, Chapter 2, was devoted to describe the theoretical fundaments of the physics behind the transient absorption microscope discussed, including a review on the pump-probe theory, the image formation for both the linear and non-linear case and a brief description of the theory of the nonlinear optical parametric processes used to generate the pump and probe beams of the transient absorption microscope. In Chapter 3 a brief discussion of the physics as well as the cellular uptake of the samples under study was given. A discussion of the technical details of the transient absorption microscope and its components was given in Chapter 4, with a final discussion of the results gathered, Chapter 5.

Chapter 2

Theory

In this chapter a theoretical description of the intrinsic physics of the experimental techniques employed to obtain the experimental results of this thesis is given. A brief introduction to pump-probe spectroscopy is provided in Section 2.1, followed by an introduction to nonlinear spectroscopy, Section 2.2, follows the theory popularized by Mukamel and co-workers [23]. The density matrix formalism and its evolution over time after optical perturbation inducing changes in a material is discussed in Section 2.3. In order to carry out the experimental work presented chapter 4.1, second-order nonlinear wave-mixing processes were employed: Second harmonic generation (SHG), sum-frequency generation (SFG) as well as difference-frequency generation (DFG). SHG processes were key elements for the construction of optical parametric amplifiers (based on DFG processes), the optical devices employed to produce the probe and pump beams necessary for pump-probe microspectroscopy, whereas SFG processes were employed to determine the temporal resolution of the TAM. For these reasons sections 2.4 and 2.5 of this chapter will be devoted to describe the physics of parametric processes from the classical and quantum mechanical perspectives. In the end of this chapter, Section 2.6, the imaging fundaments are reviewed in order to proceed with a discussion on nonlinear microscopy. All the ideas contained in the mentioned sections converge on a description of the pump-probe image formation.

2.1 Pump-probe spectroscopy: an overview

Pump-probe spectroscopy, the simplest of a broad set of ultrafast nonlinear spectroscopic techniques, is a very powerful and versatile tool used to study photoinduced dynamics of molecular systems in the time domain [24–28]. It has been used to describe ultrafast dynamics and relaxation rates of molecular systems in a broad range of environments, from solutions[29, 30], proteins and biological systems [31–38] to solid [39–44] and in the gas [45–

47] phase. This technique is based on a Michelson-interferometer whose light beams consist of (uncorrelated) femtosecond train pulses [25]. One branch of the interferometer guides an intense beam, the pump, to the sample with the purpose to photo-excite chemical species. The other branch of the interferometer brings a second (delayed) beam, the probe, to the non-equilibrated sample with the objective of explore the photo-induced changes provoked by the pump beam. The intensity of the probe beam is weaker than the corresponding intensity of the pump beam as multiphoton processes are of no interest for pump-probe spectroscopy and should be avoided. Pump-probe experiments can be classified according to the probe energy. When the probe beam is a weak version of the pump beam, i.e. it has the same energy as the pump beam, the system is termed "degenerated", on the other hand, when the photons of the probe beam have a different energy of that from the photons of the pump beam the system is named "non-degenerate" or two color pump-probe set-up [48].

The evolution of the photoinduced species can be followed by changing the delay time between the pump and probe pulses, thus this technique can be seen as snapshot-like spectroscopy, since it samples a state of a particular molecular system in a precise temporal moment given by the delay time between pump and probe pulses [49]. An obvious way to quantify this changes is by measuring at a specific delay time τ the absorption of the probe beam right after it has gone through the perturbated sample and compare it with the absorption obtained in the absence of a pump pulse. Therefore, in order to calculated the *transient absorption* of the probe beam, it is necessary to measure both the intensity $\check{I}_{probe}(\lambda,\tau)$ of the probe beam after it has propagated through a perturbated sample and the corresponding intensity $I_{probe}(\lambda,\tau)$ obtained when the probe beam has propagated through an unperturbed sample. If the Beer-Lambert law is invoked, the differential absorbance of the probe beam is given by:

$$\Delta A(\lambda,\tau) = -\log_{10}\left(\frac{\check{I}_{probe}(\lambda,\tau)}{I_{probe}(\lambda,\tau)}\right) \equiv \sum_{i=1} E(\lambda,i)\,C(i,\tau)\,l \tag{2.1}$$

The matrix C contains the concentration profiles of the i^{th} transient species as function of the delay time while the matrix E holds their differential molar absorptivities (or spectra). l denotes the thickness of the sample. As can be seen on Equation 2.1, every single differential absorption measurement has implicitly spectroscopic and kinetics information, i.e. E and C [50–53]. Extraction of these quantities can be achieved by applying model-based analysis. When a kinetics model describing the evolution of the reaction is not available, as first approximation, the data can be fitted through a sum of exponential decays using a *global analysis model*. This is done assuming that the species under study undergo a consecutive elementary reaction described by a differential equation whose solution is given by an

exponential function, i.e. sequential first-order reactions. Furthermore, the species are assumed to not interact between each other and that the evolution of all the species is parallel in time. The number of exponentials, j, with their respective rate constants k_j, for the fit should be consistent with the physical behavior of the sample, since a big number of exponential functions will indeed fit the data "well". Such fit will, however, lack physical reliability. Then, the concentration for the i^{th} species can be expressed as $C(i,\tau) = \sum_j \mathrm{e}^{\left(-k_j\tau\right)}$.

On the other hand, when there is a priori knowledge about the kinetics of the system, a *target analysis* can be applied [52]. For this it is only necessary to compute the ordinary differential equations describing the system, setting the initial conditions, i.e. the initial concentrations of the species and the first guesses of the rate constants k_j, followed by a numerical integration [50, 52, 54, 55]. Once the concentration profiles have been obtained, it is possible to get the differential molar absorptivities matrix using the *pseudo inverse* of the concentration profiles, i.e. $E = \Delta A \left(C^T C\right)^{-1} C^T$ [55]. Using directly the inverse of C is not a possibility since it is not a square matrix, as this would imply an equal number of species and time delay points [50–52, 54–58].

To illustrate the lines discussed above, on Figure 2.1 Panel A, a plot of typical experimental transient-absorption data is presented. In practice this is the type of data the experimentalist would deal with. Since usually no information about matrices E and C is at hand, the pump-probe spectroscopist needs to extract this information from the data, which implies the solution of an inverse problem [52]: get the matrices E and C from the experimentally obtained ΔA matrix. Panel B of Figure 2.1 shows the spectra associated to the species involved in the evolution of the photoinduced dynamics while Panel C of the same figure shows the concentration profiles of the species. From Equation 2.1 the sum of the product of matrix E and matrix C, each depicted on Panel B and C respectively, of all the involved species i builds up the differential absorption ΔA.

In pump-probe spectroscopy Fourier limited laser pulses following a Gaussian temporal envelope in the femtosecond time regime[1], possessing temporal durations on the same time scale of molecular vibrational periods ($\approx 10^{-13}s$) [24] can be used to directly observe the photophysical processes occurring in the electronically excited molecules [24–26], such as energy and electron transfer, internal conversion (IC), intersystem crossing (ISC), including radiative and non-radiative processes, etc. In order to be able to resolve specific molecular dynamics, the employed laser pulses should be shorter than the investigated dynamics [26]. However, as narrower the temporal duration of the pulse, the broader its spectrum [59]. This imposes a compromise between temporal resolution and bandwidth, which should be taken into account when one seeks either temporal resolution or photo-selectivity since the shorter

[1] $1fs = 1 \times 10^{-15}s$.

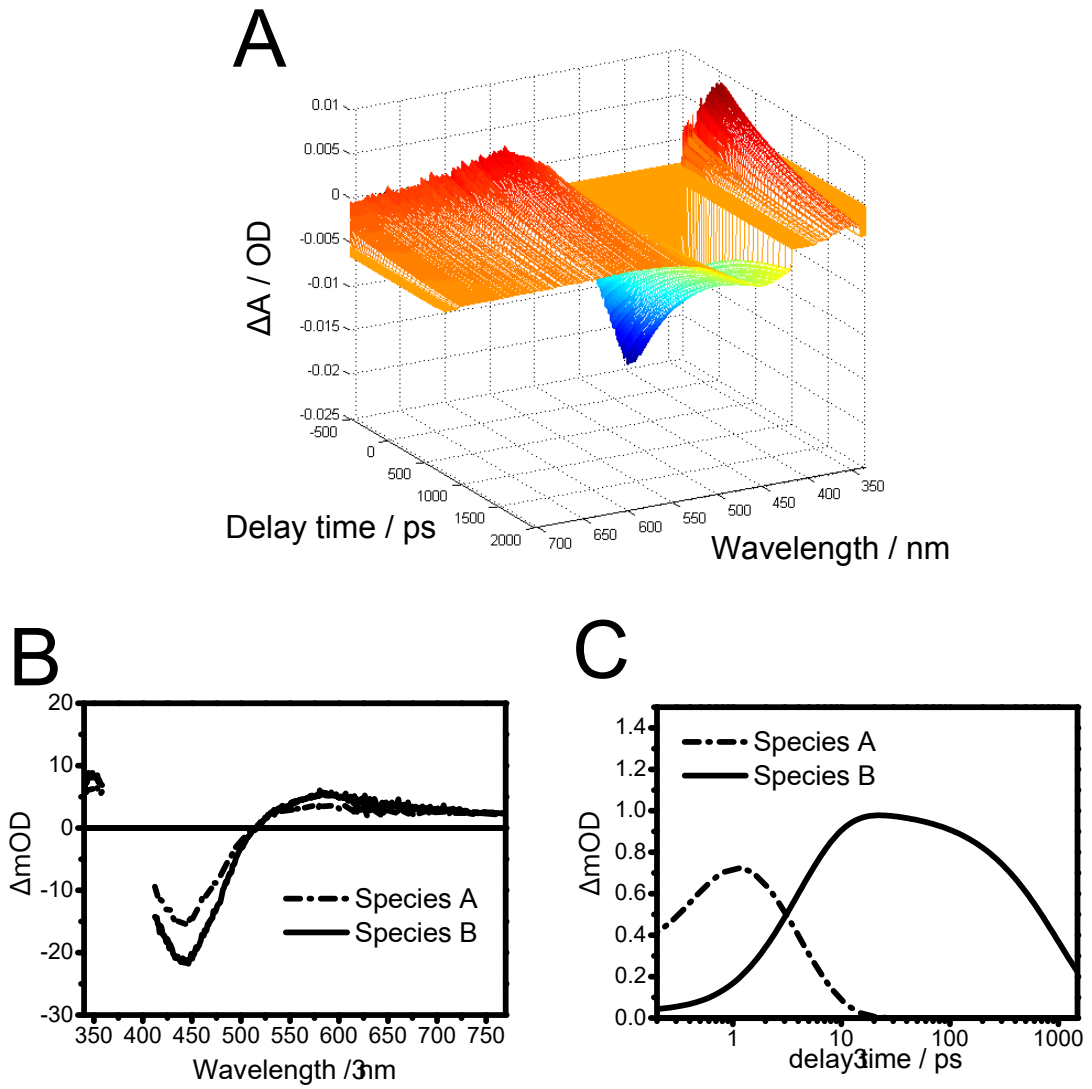

Fig. 2.1 A) Typical experimental data obtained with pump-probe spectroscopy. Results correspond to the ultrafast photoinduced dynamics of $[Ru(bpy)_2dppz]^{2+}$ *dissolved in a DNA solution. B) The differential molar absorptivities of the photo-induced species and C) their corresponding concentration profiles.*

the optical pulse the broader its spectrum which might induce the excitation of chemical species simultaneously [60]. In any case, the temporal resolution in pump-probe spectroscopy is always a critical parameter, as it determines the processes one would be able to analyze and it is determined by the width of the instrument response function (ISR), which is given by the (experimental) cross-correlation between pump and probe pulses [61–63], see Section 4.1 for a brief discussion on the experimental determination of the temporal resolution. Thus, the changes induced on the probe beam by any transient modulation of the material system provoked by the pump beam are given by the impulse response function of the material system convolved with the ISR. Furthermore, an additional parameter that is crucial and directly related to the temporal resolution of pump-probe spectroscopy is the minimum increment of the delay time τ. From the discussion above, can be state that pump-probe spectroscopy alongside femto-second light pulses opens-up the possibility to answer the question: “How do reactions proceed and what are their rates?”[24].

2.2 Introduction to nonlinear spectroscopy

The propagation of an optical perturbation in a material system, which is assumed to be non-magnetic, containing no net free charges ($\rho = 0$) neither free current densities ($\vec{J} = 0$), can be described with the Maxwell's equations. In the International System of Units (SI) the expressions for the electric field $\vec{E}$, the magnetic intensity $\vec{H}$, the electric displacement $\vec{D}$ and the the magnetic induction $\vec{B}$ in such material are [64, 65]:

$$\nabla \times \vec{E} = -\frac{\partial}{\partial t}\vec{B}, \quad \nabla \times \vec{H} = \frac{\partial}{\partial t}\vec{D}, \quad \nabla \cdot \vec{D} = 0, \quad \nabla \cdot \vec{B} = 0 \tag{2.2}$$

To describe the interaction of an electromagnetic field and matter it is necessary to split the material equations accompanying the Maxwell's equations, i.e. the electric displacement $\vec{D}$ and the magnetic induction $\vec{B}$, (each) into two parts [66]:

$$\begin{aligned} \vec{D} &= \varepsilon_0 \vec{E} + \vec{P} \\ \vec{B} &= \mu_0 \vec{H} + \vec{M} \end{aligned} \tag{2.3}$$

One part is the perturbation, the electric field $\vec{E}$ or the magnetic intensity $\vec{H}$, in the free space while the second part arises from the influence of the matter, namely the electric polarization $\vec{P}$ and the magnetic polarization $\vec{M}$. μ_0 and ε_0 are the magnetic permeability and the electric permittivity of the free space, respectively. From equation 2.3 it can be seen that the electromagnetic perturbation produces at a given volume element certain amount of polarization $\vec{P}$ [64, 65] [2]. When the electromagnetic perturbation is weak the induced polarization is a linear function of the applied $\vec{E}$, thus, diverse optical processes (termed "linear") might take place, e.g. absorption, propagation, refraction, etc. A different situation occurs when the material system is exposed to strong ($\vec{E} \geq 3 \times 10^3\ V/cm$) [67] electromagnetic fields: a nonlinear response of the polarization $\vec{P}$ might be induced, leading to a broad set of phenomena unobservable in the linear regime [67–69].

Nonetheless, if the values of the applied field are limited to have magnitudes that are not capable to ionize or generate laser ablation on the material system, the average atomic electric field ($\vec{E}_{atom} \approx 3 \times 10^8\ V/cm$) is still higher than the applied field, thus the perturbation is considered weak. The last statement allows the use of perturbation theory and as a consequence the polarization is expanded in terms of the incoming electric field [65, 67–69, 23]:

$$\vec{P}(r,t) = \sum_{l=1}^{\infty} \vec{P}^{(l)}(r,t) \tag{2.4}$$

[2] Recall that the material system we are dealing with has been assumed to be non-magnetic, i.e. $\vec{M} = 0$.

The term $l = 1$ correspond to $\vec{P}^{(1)}(r,t)$, which reflects the linear polarization, while $l \geq 2$ form the nonlinear polarization terms $\vec{P}^{(NL)}(r,t)$. Thus, in spectroscopies techniques with coherent nature, the incident electric fields act on the material system to form a *macroscopic* charge distribution undergoing coherent oscillations which are proportional to the tensorial electric susceptibility χ of the material:

$$\vec{P}^{(l)}(t) = \varepsilon_0 \chi^{(l)} \vec{E}(t)^l \tag{2.5}$$

Thus different spectroscopical techniques are classified accordingly to their dependence on the applied electric fields, e.g. first, second or third order nonlinear processes.

Using equations 2.3 one can verify [65] that the wave equation describing the propagation of the outgoing electromagnetic fields through a material that has been exposed to strong incoming electromagnetic fields is given by

$$\nabla^2 \vec{E}(\vec{r},t) - \frac{1}{\varepsilon_0 c^2} \frac{\partial^2}{\partial t^2} \vec{D}(\vec{r},t) = \frac{1}{\varepsilon_0 c^2} \frac{\partial^2}{\partial t^2} \vec{P}^{(NL)}(\vec{r},t) \tag{2.6}$$

The nonlinear polarization $\vec{P}^{(NL)}$ induced in the material system has a crucial role in the description of nonlinear optical phenomena, as can be inferred from Equation 2.6. The second derivative of the nonlinear polarization implies acceleration of electric charges with an inherent emission of electromagnetic radiation, therefore the time varying polarization can be seen as source of new wavelets of the electromagnetic field, which under special conditions can contain spectral components not present on the incident perturbation, e.g. second harmonic generation or white light super continuum [70–72]. Furthermore, pump-probe spectroscopy, the tool employed to characterize the ultrafast dynamics of photoinduced chemical reactions, is a nonlinear spectroscopical technique related to the third order nonlinear polarization, which is the most common nonlinear polarization since in isotropic materials, i.e. the majority of materials studied in chemical reaction dynamics, the even order susceptibilities disappear.[24, 49]

2.3 Third order nonlinear polarization

A semi-classical approach to calculate the third order polarization $\vec{P}^{(3)}$ induced by a strong electromagnetic perturbation is done by means of the Liouville-von Neumann equations and the density matrix formulation [23, 73–75]. In this hybrid approach, the material system is described quantum mechanically while the incident electromagnetic field is assumed to have a classical nature. The material system under study can be formed by a set of non-interacting identical molecules immersed in a bath (e.g. a solvent), where only the molecules

are resonant to the electromagnetic perturbation. Thus, the total Hamiltonian of this system can be expressed by

$$H = H_0 + H_{int}(t) \tag{2.7}$$

The molecular Hamiltonian H_0 describes a stationary system without coupling between states in absence of any external perturbation. This term, which contains the energies of the different states of the material system is extremely important for a spectroscopist, as it is the physical quantity interrogated by the employed spectroscopic technique.

If the dimensions of the molecules forming the probed system are smaller than the wavelength of the incident perturbation, the expression for the interaction Hamiltonian[3] of a single molecule positioned at r can be assumed simply as:

$$H_{int}(t) = -\mu E(r,t) \tag{2.8}$$

Where μ is the dipole moment operator constituted by the dipoles of all the particles[4] m (i.e. electrons and nuclei possessing an electric charge q_m) that conform the molecule and it is proportional to r:

$$\mu = \sum_{m=1} q_m(r - r_m) \tag{2.9}$$

Using the variables discussed above, alongside the reduced Planck constant $\hbar$ and the density matrix operator ρ, the Liouville-von Neumann equation can be expressed as:

$$\frac{\partial \rho(t)}{\partial t} = -\frac{i}{\hbar}[H, \rho(t)] - \Gamma\rho(t) \tag{2.10}$$

To describe the interactions of the molecule with the bath, e.g. by collisions, which lead to a subsequent relaxation, (phenomenological) relaxation terms Γ are often included to H. The terms contained in the matrix Γ are the relaxation rates of the populations (the diagonal terms of the density matrix) and the population transfer rates related to the coherences (the off-diagonal elements of the density matrix). Γ can be rationalize as a measure to express the time that would take to the molecule in recover its initial nature, i.e. before the perturbation [76, 77].

Where $\rho(t)$ is the outer product of the wavefunction $|\psi(t)\rangle$ describing a *pure state*[5]:

[3] Hereafter $\vec{P}$, $\vec{\mu}$, $\vec{r}$ and $\vec{E}$ will be considered scalar quantities as orientational effects will be neglected.

[4] Has been assumed that the molecule possess symmetry inversion and that the energy eigenstates keep a definite symmetry (i.e. even or odd), thus all the diagonal elements of $H_{int}(t)$ vanish.

[5] Here, only pure states will be considered, however it is possible to treat mixed states of molecular assembles using the density matrix formulation.

$$\rho(t) = |\psi(t)\rangle \langle\psi(t)| \tag{2.11}$$

From electrodynamics it is known that in the macroscopic domain, whose absolute lower limit will be considered as 10^2Å [64], the polarization is the expected value of the sum of all the molecular dipoles contributing to the molecular assemble, therefore the contribution of the molecule of interest to the macroscopic polarization will be $\langle\mu\rangle$. Now one of the most attractive properties of the density matrix is employed:

$$P(r,t) = \langle\mu\rangle = \mathrm{Tr}[\mu\rho(t)] \equiv \langle\mu\rho(t)\rangle \tag{2.12}$$

Equations 2.6, 2.10 and 2.12 form the *Coupled Maxwell-Liouville* equations and the field-matter interaction can be described entirely with them [23, 78].

Consider a molecule with three energetic states. Imagine that this molecule will be investigated with the archetypical pump-probe spectroscopy set-up, i.e. a photoinduced dynamics on the molecule is triggered by a femtosecond laser pulsed beam (the pump), whose energy would be assumed to solely match the difference between the energy of the first excited state and the ground state of the molecule, while the evolution of such photo-induced dynamics will be explored by a delayed pulsed laser beam (the probe). Before any interaction between the molecule and the laser beams, the molecule is assumed to be in thermal equilibrium and thus in its ground state $|0\rangle$. Furthermore, for this ideal molecule the transition dipole moments associated with energetic shifts from $|0\rangle$ to $|2\rangle$ are zero, making such transitions forbidden, see Figure 2.2 Panel A. The idealized pump-probe system used to study this molecule is depicted in Figure 2.2 Panel B, where the induced polarization is heterodyne detected (using the probe beam itself as a local oscillator). The last statement implies that the experimental geometry of the pump-probe set-up imposes a condition on the phase matching of the resultant wave vector of the probe beam: Either the sample has to interact twice with the pump pulse ($\vec{k}_{probe} = \vec{k}_{probe} + \vec{k}_{pump} - \vec{k}_{pump}$) or go through three interactions with the probe pulse ($\vec{k}_{probe} = \vec{k}_{probe} - \vec{k}_{probe} + \vec{k}_{probe}$). Due to the fact that the pump beam is very intense compared to the probe beam, the second phase matching condition is neglected. Moreover, the second phase matching condition is removed experimentally by measure with the pump-on and pump-off condition, as it involves saturation by the probe beam and does not provide useful information for the differential absorption ΔA [49, 23].

If we attempt to perform a pump-probe spectroscopy experiment, the average of the total electric field perturbing the molecule, i.e. a pump and a probe pulse, will be given by:

$$E(t) = \sum_j [E_j(t) \exp\left(-i\omega_j t + ik_j r\right) + c.c] \tag{2.13}$$

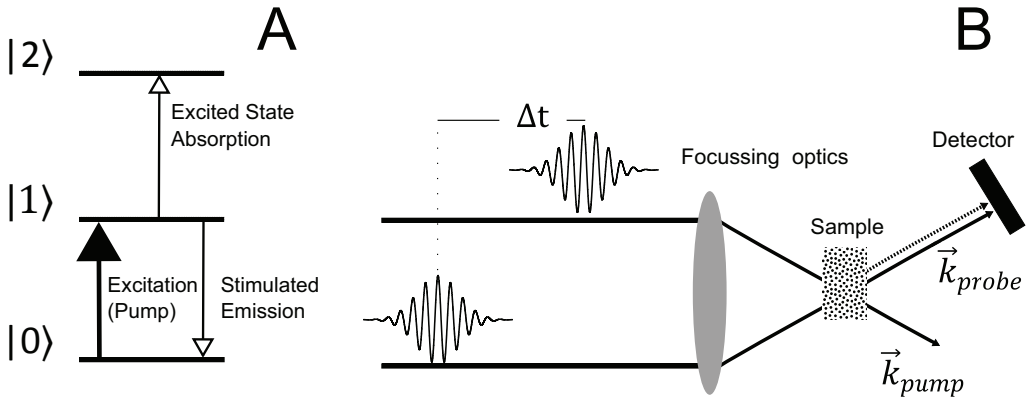

Fig. 2.2 A) Energy diagram of a three level molecule. During a pump-probe experiment this molecule is excited by an intense pump pulse, from this excited state it can either be re-excited or driven to the ground state (along side stimulated emission) by a probe pulse. B) The archetypical pump-probe spectroscopy set-up.

In the idealized pump-probe experiment mentioned above and depicted in Figure 2.2 panel B, j runs from pump to probe, $E_j(t)$ is the amplitude envelope of the electric field, ω_j and k_j represent, respectively, the frequency and the wavevector of the j^{th} pulse and $c.c$ denotes complex conjugated. Note that in the case $j = probe$ a delay time term might be included to the amplitude of the signal $E_{probe}(t)$. As the field described by Equation 2.13 represents the perturbation of the system, it has to be inserted into Equation 2.8.

Let's now consider perturbation of the molecule. If the terms $E_j(t)$ of equation 2.13 are chosen to keep a constant value over time, e.g. 1, the perturbation would consist of two optical traveling waves with frequencies given by ω_{pump} and ω_{probe}, see Figure 2.3, panels a-c. Before the perturbation interacts with the molecule, the latter is assumed to be in its ground state. As the perturbation carrying a frequency ω_{pump} evolves in time, the probability to find the molecule in its ground state decreases and parallel to this event, an increment on the probability to find the molecule on the first excited state is observed. From this first excited state, the probe pulse is able to bring the molecule to a second excited state. Subsequently it relaxes[6], the ground state recovers and the cyclic nature of the perturbation is mapped into the populations probabilities, see Figure 2.3 Panel A.

A more realistic approach to describe the pump-probe incoming field would be obtained by including the time ordering of the pulses and the pulsed nature of the perturbation, which means that the oscillations of Equation 2.13 need to be temporally confined by a Gaussian envelope function with a temporal width T_w, centered at t_0 and interact with the molecule sequentially, i.e. $E_j(t) \propto e^{(-\frac{t-t_0}{T_w})^2}$. Now consider that the same molecule is perturbated with time ordered oscillations following a Gaussian envelope. Again, the molecule stays in the

[6]This stems from the fact that $H^*_{nm} = H_{mn}$.

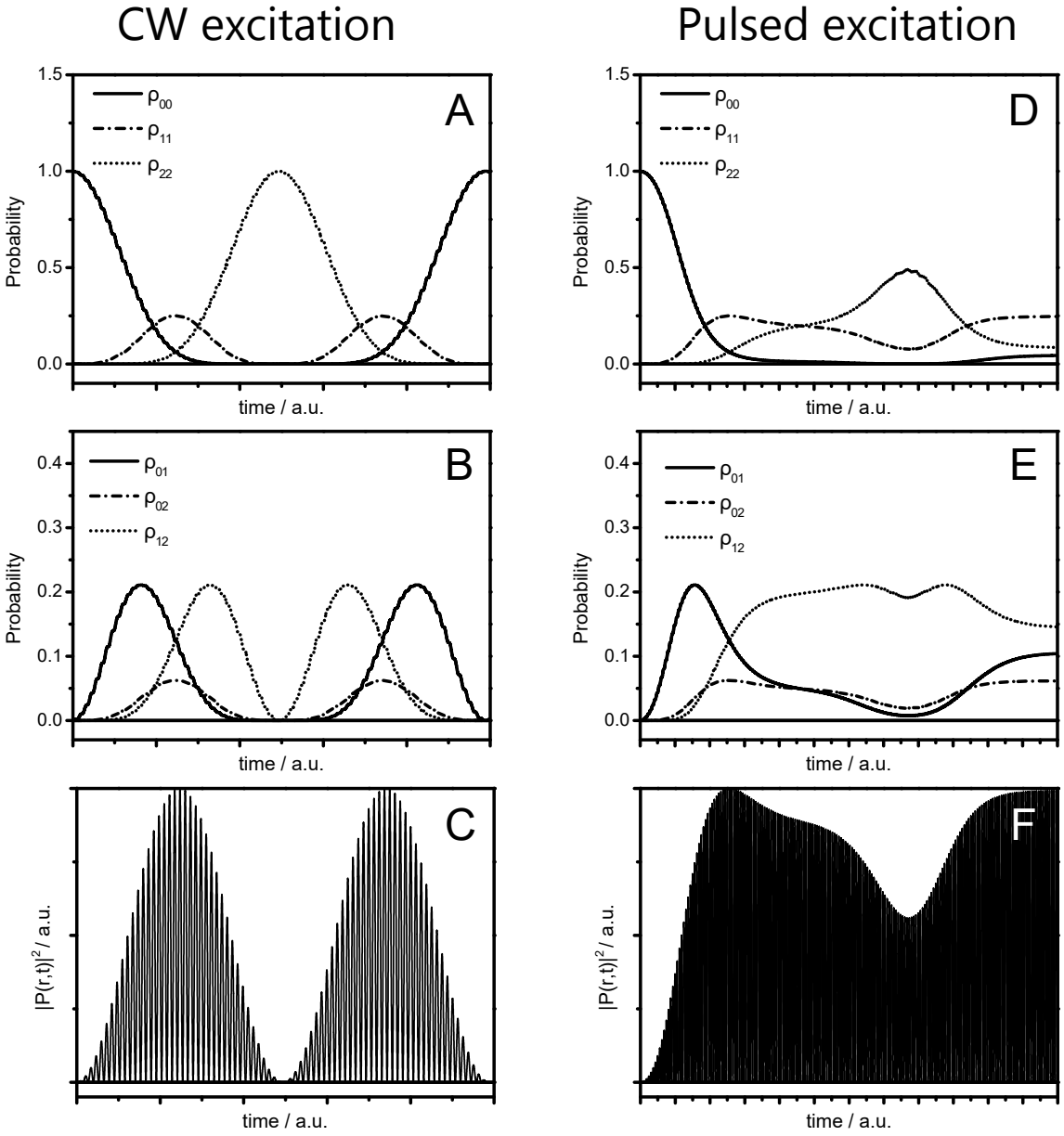

Fig. 2.3 Numerical solution of Equation 2.10 obtained with the Runge-Kutta method. Panel A (D) shows the evolution of the population terms of $\rho(t)$ while Panel B (E) depicts the evolution of the coherences. Panel C (F) shows the absolute value of the macroscopic polarization calculated with Equation 2.12. For this simulations was assumed that $\hbar\omega_{pump}$ was resonant only with the $|0\rangle \rightarrow |1\rangle$ transition, while $\hbar\omega_{probe}$ was assumed to be in resonance with $|0\rangle \rightarrow |1\rangle$ and $|1\rangle \rightarrow |2\rangle$ transitions, in addition, the transitions from $|0\rangle \rightarrow |2\rangle$ were forbidden. For panels A-C $E_j(t) = 1$ while for panels D-F $E_j(t) \propto e^{(-\frac{t-t_0}{Tw})^2}$.

ground state until the pump pulse disturbs it, see Figure 2.3 Panel D. The probability of the molecule to be in the ground state is depleted to increase the probability of occupation of the first excited state, which inherently adds probability to the second excited state. There is a time interval where nothing happens and that is because no external perturbation is being applied, thus the molecule evolves with H_0. The system is perturbated, again, with the probe field, whose maximum peak coincides with the maximum peak of the curve ρ_{22}.

So far, only the diagonal terms (or populations) of the density matrix have been discussed. These terms can be used to calculate the rates for absorption and stimulated emission and with them the total rate of spontaneous emission might be deduced [79]. However, it should be emphasized that here a semi-classical model is being applied and to be noted that the absence of a classical perturbation avoids energetic transitions, thus nullifying any possibility to explain spontaneous emission [80][7]. And even if a sample emits both, spontaneous and coherent radiation, here the only relevant signals are those whose origin is a coherent oscillation of μ, which from equation 2.12, are directly related to the off-diagonal elements of $\rho(t)$.

The evolution of the coherences, which indicate superposition or correlation between states, evolving under the two different excitations with different temporal confinements, i.e. $E_j(t) = 1$ and $\propto e^{(-\frac{t-t_0}{T_w})^2}$, are presented in Figure 2.3 Panels B and E respectively, while on the same Figure but on panels C and F the corresponding absolute values for the macroscopic polarization are plotted. Note that the coherences are zero when the population terms are maximum and vice versa. Furthermore, the trend exhibited by the coherences is also observed on the envelope of the absolute value square of the calculated macroscopic polarization: when a maximum is observed on the probability of the population terms, a minimum appears in the induced polarization, and vice versa, as predicted with Equation 2.12. Thus, perturbations to the material system induce *coherent* oscillations on the effective electric dipole moment which in turn give rise to *coherent* fluctuations on the macroscopic polarization of the material sample [73], and as shown in Equation 2.6 will serve as a source of *coherent* electromagnetic radiation, giving rise to a plethora of non-linear optical spectroscopy techniques [23], as for example four wave mixing (4WM), from which coherent anti Stokes-Raman spectroscopy (CARS) and pump-probe spectroscopy derive.

Note that the results of the polarization presented in Figure 2.3 Panels C and F, show the sum of the linear polarization term plus all the polarization harmonics induced by the different orders of the incoming electric field, see Equation 2.6. As mentioned, and reported elsewhere

[7] In order to be able to explain spontaneous emission one needs to the quantize the electromagnetic field, the molecular system and of course the interaction [81].

[82], pump-probe spectroscopy depends on $\vec{P}^{(3)}(r,t)$[8], this means that the material system interacts three times with the incident perturbation, and as discussed above, a condition imposed by the experimental geometry of pump-probe spectroscopy.

In order to calculate the third order polarization, the density matrix describing the material system needs to be expanded in terms of the incoming electric field and particularly $E(t)^3$.

To begin with, note that Equation 2.10 includes the total Hamiltonian $H(t)$, which is the sum of the molecular and the interaction Hamiltonians. As the molecular fields are considered stronger than the applied fields, perturbation theory can be used. Note that H_0 determines the stationary states of the system and H_{int} is a function of the (timed dependent) applied field, then a transformation from the so called Schrödinger (SP) picture to the interaction picture (IP) needs to be performed [83]. To this end $\rho(t)$ is set as:

$$\rho(t) = U_0^{\dagger}(t-t_0)\rho_{IP}(t)U_0(t-t_0) \tag{2.14}$$

Where the superscript † denotes hermitian conjugated and $U_0(t-t_0)$ is simply the solution to the eigenvalue problem of the (*time independent*) Hamiltonian H_0:

$$U_0(t-t_0) = \exp\left[-\frac{i}{\hbar}H_0(t-t_0)\right] \tag{2.15}$$

If Equations 2.14 and 2.15 are inserted into Equation 2.10 can be easily shown that the Liouville-von Neumann equation in the IP is given by:

$$\frac{\partial \rho_{IP}(t)}{\partial t} = -\frac{i}{\hbar}[H_{IP}(t), \rho_{IP}(t)] \tag{2.16}$$

With the perturbation, see Equation 2.8, in the interaction picture expressed as:

$$H_{IP}(t) = U_0^{\dagger}(t-t_0)H_{int}(t)U_0(t-t_0) \tag{2.17}$$

It is straight forward, but tedious, to show that when Equation 2.16 is integrated canonically, with a subsequent variable exchange between time points and time intervals of the integrals and assuming that the perturbation interacts with the sample at $t = 0$, the density matrix term corresponding to the third order interaction is given by:

[8]To keep the notation simple, the perturbated molecule will be located at $r = 0$. The electric field and the induced polarization will be defined as $E(t) \equiv E(r,t)$ and $P(t) \equiv P(r,t)$ respectively.

$$\rho_{IP}^{(3)}(t) = \int_0^\infty dt_3 \int_0^\infty dt_2 \int_0^\infty dt_1 E(t-t_3)E(t-t_3-t_2)E(t-t_3-t_2-t_1) \times \left(\frac{-i}{\hbar}\right)^3 [\mu(t_2+t_1),[\mu(t_1),[\mu(0),\rho(-\infty)]]] \tag{2.18}$$

Recall that the $\mu(\tau)$ are the dipole operators in the interaction picture, i.e. $\mu(\tau) = U_0^\dagger(\tau - t_0)\mu U_0(\tau - t_0)$. Also note that in the IP the electric dipole moment operators are time dependent. This is due to the fact that the molecular Hamiltonian H_0 still acts on the *perturbated* system. From Equation 2.18 is evident that (from right to left), the system begins with the value it had before any perturbation, i.e. its initial condition $\rho(-\infty)$. At $t = 0$ the system is perturbed for the very first time through a term proportional to $\mu(0)$, while the second and third interactions arrive after time intervals given by t_1 and $t_1 + t_2$ alongside terms $\mu(t_1)$ and $\mu(t_2)$, respectively.

To obtain the third order polarization it is only required to apply its definition from electrodynamics, see Equation 2.12, but now using only the density matrix corresponding to the third order interaction:

$$P(t)^{(3)} = \int_0^\infty dt_3 \int_0^\infty dt_2 \int_0^\infty dt_1 E(t-t_3)E(t-t_3-t_2)E(t-t_3-t_2-t_1)S(t_3,t_2,t_1)^{(3)} \tag{2.19}$$

Being $S(t_3,t_2,t_1)^{(3)}$ the third order nonlinear response function of the material system:

$$S(t_3,t_2,t_1)^{(3)} = \left(\frac{-i}{\hbar}\right)^3 \left\langle \sum_{\alpha=1}^{4} [R_\alpha(t_3,t_2,t_1) - R_\alpha^*(t_3,t_2,t_1)] \right\rangle \tag{2.20}$$

Where R_α are the *dipole correlation functions* [84]:

$$\begin{aligned} R_1(t_3,t_2,t_1) &= \mu(t_3+t_2+t_1)\mu(0)\rho(-\infty)\mu(t_1)\mu(t_2+t_1) \\ R_2(t_3,t_2,t_1) &= \mu(t_3+t_2+t_1)\mu(t_1)\rho(-\infty)\mu(0)\mu(t_2+t_1) \\ R_3(t_3,t_2,t_1) &= \mu(t_3+t_2+t_1)\mu(t_2+t_1)\rho(-\infty)\mu(0)\mu(t_1) \\ R_4(t_3,t_2,t_1) &= \mu(t_3+t_2+t_1)\mu(t_2+t_1)\mu(t_1)\mu(0)\rho(-\infty) \end{aligned} \tag{2.21}$$

$S(t_3,t_2,t_1)^{(3)}$, formed by R_α, contains all the microscopic information required to describe any measurement related to $P(t)^{(3)}$. Note that the physical interpretation of the Equations shown in 2.21 is that they describe a specific (sequential) evolution of the density matrix over three time periods. Taking as example R_4, a coherence (or off-diagonal element of the

density matrix) is created at $t = 0$, thus the system will evolve perturbation-free during a time period t_1 when a second perturbation is made to the system, again the system propagates for a time period $t_1 + t_2$, when a third perturbation occurs. The last interaction occurring at $t_1 + t_2 + t_3$[9] has to bring the density matrix to a population state. In other words: the first three interactions, i.e. those occurring in a time interval $t < t_1 + t_2 + t_3$, "do something" to the material system and alters the density matrix. At $t = t_1 + t_2 + t_3$ the coherences of that perturbated density matrix will emit radiation whose overall frequency and wave-number will be given by the sum of those corresponding to the incident radiation. The last paragraph can be summarized in Figure 2.4. A similar treatment can be given to the rest of R_α [49].

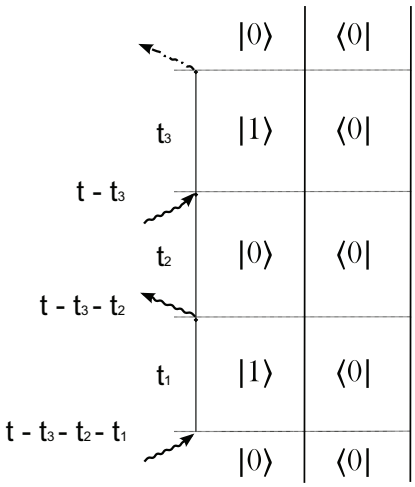

Fig. 2.4 The double-sided Feynman diagram for R_4. Note that the wavy arrow for the interaction at $t_1 + t_2 + t_3$ is different. This emphasizes the fact that the nature of this perturbation is distinct to those occurring at $t = 0$, $t = t_1$ and $t = t_1 + t_2$ and results from $\mathrm{Tr}[\mu\rho(t)]$.

As can be seen on Figure 2.4, a diagrammatic description of the different phenomena occurring during a spectroscopic experiment can be obtained. These diagrams allow to "visualize" and follow the evolution of the material system, described by the density matrix subjected to the electric fields [23, 49, 74]. The diagrams can also depict the contributions to a specific nonlinear signal, e.g. excited state absorption or stimulated emission, from a particular state of the system. Each diagram is termed as "doubled sided Feynman diagram" and is composed by two parallel lines. The left one represents the ket of the density matrix while the right one the bra. In these diagrams, the time runs from bottom to top (vertically) and the interactions with the fields are depicted as wavy arrows. To reduced the number of terms in Equation 2.19, only resonant terms of the incident electric fields will be considered, i.e. either the field contributes to the perturbation with $e^{-i\omega_j t + ik_j r}$ or with $e^{i\omega_j t - ik_j r}$ but not

[9] The origin of this perturbation arises from the trace performed to the product $\mu\rho$.

both terms, see Equation 2.13. This is the so called rotating wave approximation (RWA), where the apportation of the "fast oscillating" terms on Equation 2.19 are neglected. Thus, an arrow pointing to the right of a Feynman diagram denotes an electric field contributing to the perturbation a factor $\propto e^{-i\omega_j t+ik_j r}$ while an arrow pointing to the opposite direction represents an electric field with a factor $\propto e^{i\omega_j t-ik_j r}$. When the wavy arrows point inwards, the system is excited while in the case of outgoing arrows the system emits coherent radiation [23, 73, 75].

In order to derive the Feynman diagrams for pump-probe spectroscopy, a time ordering between the incoming fields should be defined. Note that the phase matching condition of the pump-probe signal ($\vec{k}_{probe} = \vec{k}_{probe} + \vec{k}_{pump} - \vec{k}_{pump}$) dictates that the sample has to interact twice with the pump field (no two pump pulses). Therefore time ordering of the pump fields is not possible, which means they will be assumed to arrive at the same time. However, the probe field is assumed to be the last field perturbing the system. An immediate result of the phase matching condition and the RWA is the fact that only[10] six terms survive to describe the phenomena occurring during pump-probe spectroscopy, see Figure 2.5 [23, 49, 73, 75].

[10]Two additional terms have to be included if pump and probe pulses overlap in time.

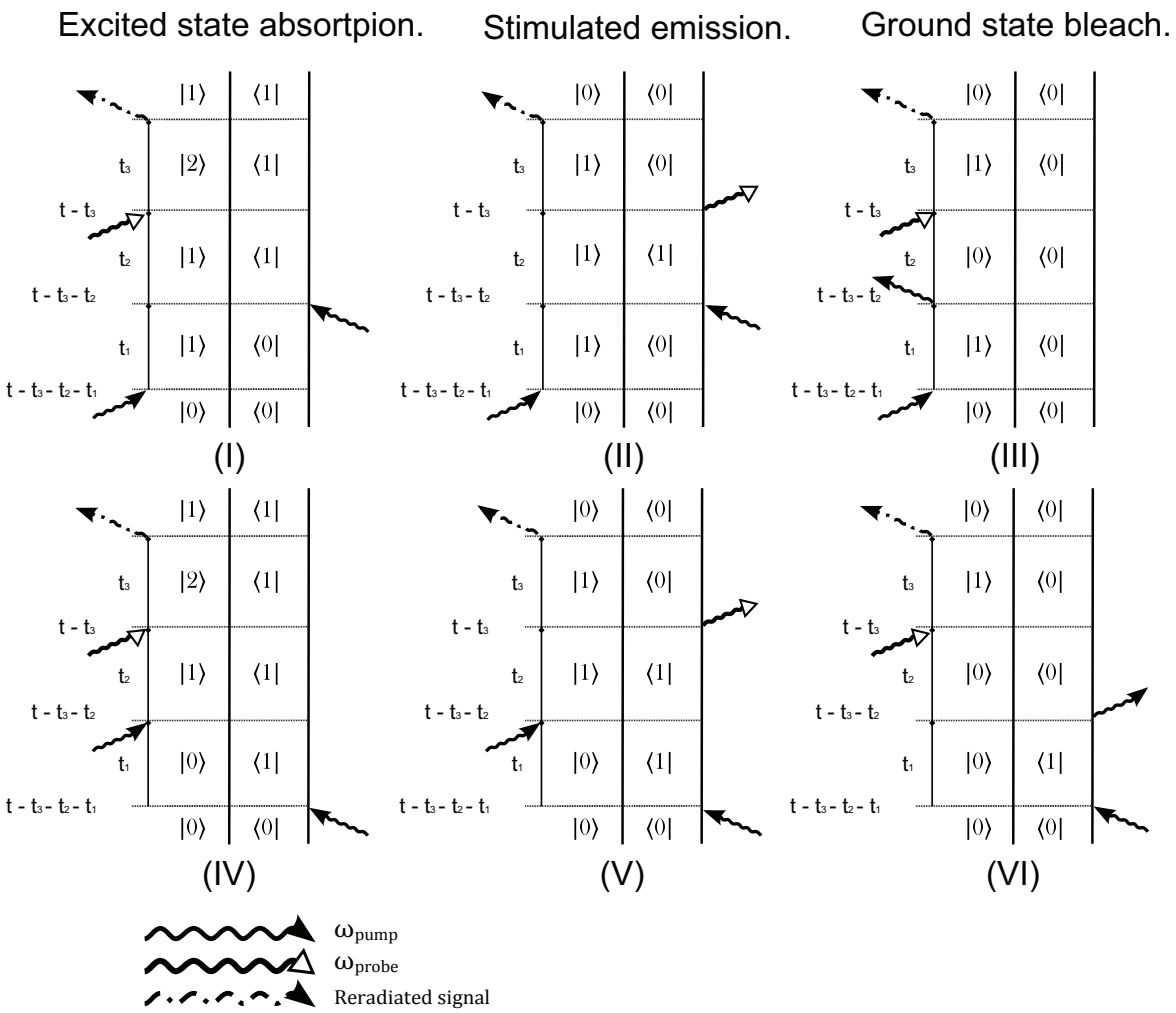

Fig. 2.5 The double sided Feynman diagrams that depict the dynamics of a three level material system, see Figure 2.2 Panel A, studied with pump-probe spectroscopy. Recall that, for pump-probe spectroscopy, $S(t_3,t_2,t_1)^{(3)}$ is conformed by the sum of the terms shown in panels I-VI, therefore the third order polarization in a pump-probe spectroscopy experiment includes the summation of the terms depicted in panels I-VI. Note how in diagrams I and VI a pump pulse brings the molecular system to an excited state. From there the probe pulse takes the system to the next level. From diagrams II and V can be seen how the pump pulse excites the system whereas the probe pulse brings it down. Diagrams III and VI show how the system is brought to the ground state after interacting with the pump pulse. Therefore, diagrams I and VI describe excited state absorption (ESA), II and V stimulated emission (SE) whereas diagrams III and VI depict ground state bleach (GB).

The mean average energy loss of the probe pulse when it propagates through the optical medium is given by:

$$\frac{\partial}{\partial t}\langle H_{int}(t)\rangle = \mathrm{Tr}\left[\frac{\partial}{\partial t}H_{int}(\omega_{probe},t)\rho(t)^{(3)}\right] = -\frac{\partial}{\partial t}E_{probe}(\omega_{probe},t)P(t)^{(3)} \tag{2.22}$$

The absorption signal at the probe frequency, i.e. ω_{probe}, can be estimated by averaging Equation 2.22 over an optical cycle with a subsequent integral over t. If the incoming pulses are decomposed into Fourier components the induced polarization can be expanded as:

$$P(t)^{(3)} = \sum_s P(\omega_s,t)^{(3)}\exp(-i\omega_s t) + c.c \tag{2.23}$$

Where ω_s can be any combination of the pump and probe frequencies ω_j. Recall that the incoming average electric field of the probe beam is defined as

$$E_{probe}(\omega_{probe},t) = E(\omega_{probe},t)\exp\left(-i\omega_{probe}t\right) + E^*(\omega_{probe},t)\exp\left(i\omega_{probe}t\right) \tag{2.24}$$

If the envelope of the probe beam is assumed to vary slowly compared to its optical frequency, i.e.:

$$\frac{\partial}{\partial t}E(\omega_{probe},t) \ll \omega_{probe}E(\omega_{probe},t) \tag{2.25}$$

the derivative of the probe beam can be approximated as:

$$\frac{\partial}{\partial t}E_{probe}(t) \approx -i\omega_{probe}\left[E(\omega_{probe},t)\exp\left(-i\omega_{probe}t\right) - E^*(\omega_{probe},t)\exp\left(i\omega_{probe}t\right)\right] \tag{2.26}$$

Inserting Equations 2.23 and 2.26 into Equation 2.22 followed by an average over an optical cycle, to further integrate on time (to account the slow response of the optical detector) the power of the differential absorption signal is obtained:

$$\Delta A(\omega_{probe},\tau) = 2\Im\,\omega_{probe}\int_0^\infty dt E^*(\omega_{probe},t)P(\omega_{probe},t)^{(3)} \tag{2.27}$$

Where $\Im$ denotes the imaginary part of the complex number. Note that Equation 2.27 contains the product of the complex envelope of the probe beam with the polarization induced by an external applied field containing a pump and a probe pulse (the probe pulse has a delay τ with respect to the pump). Here it is evident that the envelope of the probe beam is nothing else than the "local oscillator" and $P(\omega_{probe},t)^{(3)}$ the signal of interest of a heterodyne

detection system, as the pump-probe spectroscopy set-up shown on Figure 2.2. Therefore ΔA corresponds to "the total probe absorption in the presence of pump minus the probe absorption in the absence of the pump" [23, 49, 73, 75].

2.4 Coupled wave equations

SHG, SFG and DFG rely on the second order nonlinear polarization, see Equation 2.5, and can be observed exclusively in non-centrosymmetric materials [65, 85, 86]. In nonlinear wave-mixing processes, the coupling between monochromatic optical waves results from a *non-resonant* response of the material to a distortion of its electronic cloud induced by the optical perturbation. This (nonlinear) response of the material, conducted within 10^{-15} to 10^{-16} seconds, allows the transfer of energy between the involved fields [86]. Should be mentioned that the re-emitted field will carry a substantial strength if and only if the induced oscillating dipoles in the material remain in phase, a condition resulted from energy and momentum conservation of light known as phase matching.

From electrodynamics it is known that any optical field is conformed by an infinite superposition of monochromatic Fourier components, thus the propagation of every single frequency component of the field must be taken into account in *dispersive* materials [64]. To study nonlinear wave-mixing processes in second order nonlinear crystals, Equation 2.6 is expressed in the following way:

$$\left[\nabla\times(\nabla\times)+\frac{\varepsilon(\omega_n)}{c^2}\frac{\partial^2}{\partial t^2}\right]E_n(r,t)=-\frac{4\pi}{c^2}\frac{\partial^2}{\partial t^2}P_n^{(2)}(r,t) \tag{2.28}$$

Where $\varepsilon(\omega)$ is the linear dielectric constant[11], c denotes the speed of light in the free space, $P_n^{(2)}$ is the second order polarization, defined in Equation 2.5 and E_n represents the applied field. E_n is assumed to be propagating in the z direction with a linear polarization and is given by

$$E_n(z,t)=A_n(z)\exp\left[i(k_nz-\omega_nt)\right]+c.c. \tag{2.29}$$

Here k_n and ω_n represent the wave vector and the input frequency carrier respectively, whereas $A_n(z)$ stands for a slowly varying envelope. Invoking the infinite plane wave approximation and the slowly varying approximation Equation 2.29 can be reduced to the nonlinear coupled-wave equation, see Equation 2.30. In the infinite plane wave approximation, as its name suggests, it is assumed that all the interacting waves are infinite plane waves whereas in the slowly varying approximation it is assumed that the fractional change[12] in A_n over a distance of the order of an optical wavelength is negligible [65, 85, 86].

$$\frac{\partial A_n(z,t)}{\partial z}=\frac{ik_n}{2\varepsilon(\omega_n)}\left[P_n^{(2)}(z,t)\right]\exp\left(-ik_nz\right) \tag{2.30}$$

[11] $\varepsilon(\omega)=\varepsilon_0\varepsilon_r$, with ε_0 being the free space permittivity and ε_r the relative dielectric constant.
[12] $[A_n(t_2)-A_n(t_1)]/A_n(t_1)$

From Equation 2.30 it is evident how the re-emitted field is coupled to the other interacting fields in a nonlinear material through the second order polarization $P_n^{(2)}$. Thus, Equation 2.30 allows to describe nonlinear wave-mixing processes in an affable way. For example, consider the experimental set-up shown on Figure 2.6 Panel A: A coherent incident monochromatic field E_1 with a wave vector k_1, oscillating at ω_1, containing photons with energy $h\nu_1$, propagates through a nonlinear crystal. Due to the nonlinear response of the material, a second field E_2 with a carrier frequency $\omega_2 = 2\omega_1$ is generated. The re-emitted field E_2, or the second harmonic of the fundamental field, is also monochromatic and coherent. It is assumed that the crystal of the set-up shown in Figure 2.6 panel A is a lossless non-centrosymmetric medium, with a large effective second order susceptibility and a considerably high resistance to optical damage.

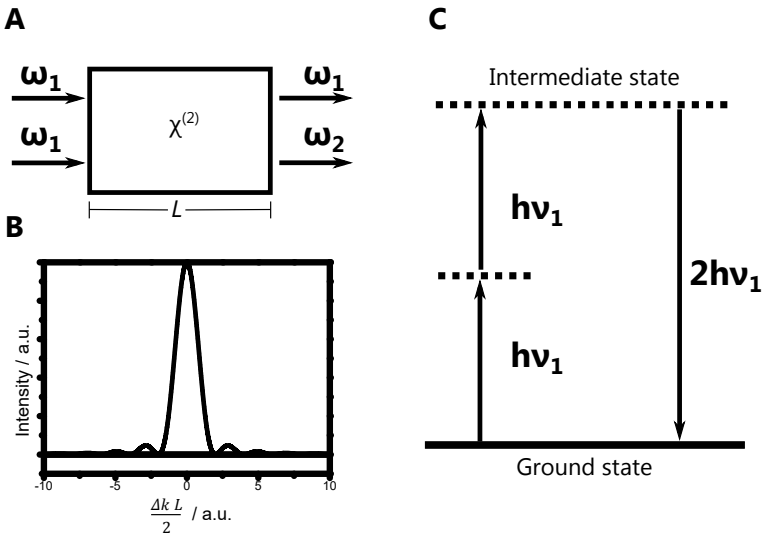

Fig. 2.6 A) Experimental geometry required for SHG. An intense field propagates through a non-centrosymmetric crystal inducing its second harmonic, i.e. a field oscillating twice as fast as the fundamental. B) SHG efficiency as function of Δk. C) Energy level representation of SHG.

The change on the amplitudes (A_1 and A_2) of the fields E_1 and E_2, involved in the nonlinear interaction over the z axis in the nonlinear crystal, can be calculated by computing the respective coupled-wave equations:

$$\begin{aligned} \frac{\partial A_1}{\partial z} &= \Lambda_1 A_1^* A_2 \exp\left[-iz(2k_1 - k_2)\right] \\ \frac{\partial A_2}{\partial z} &= \Lambda_2 A_1^2 \exp\left[iz(2k_1 - k_2)\right] \end{aligned} \tag{2.31}$$

Here Λ_1 and Λ_2 contain constant factors. The difference term in the exponential of Equations 2.31 is the phase matching condition Δk for SHG. In nonlinear crystals, the efficiency of the generated field can be modified by tuning Δk, see Figure 2.6 panel B and

Equation 2.33. In the particular case of birefringent crystals, this tuning is achieved by just moving their optical axis[13]. The last statement is a consequence of the following equality:

$$\Delta k = 2k_1 - k_2 = \frac{4\pi}{\lambda_1}\left[n(\omega_1) - n(\omega_2)\right] \tag{2.32}$$

$n(\omega)$ is the refractive index perceived by a field with a carrier frequency ω. Assuming that the amplitude of the fundamental field E_1 is strong enough for being affected by the non-linear interaction, A_1 can be treated as a constant. In this approximation, which is called the undepleted fundamental beam approximation[14], the intensity of the second harmonic beam for the set-up shown on Figure 2.6 panel A is straight forward calculated [65, 85, 86]:

$$I_2 \propto \left[I_1 \mathrm{sinc}\left(\frac{\Delta k L}{2}\right)\right]^2 \tag{2.33}$$

where I_1 is the intensity of the fundamental beam.

From the point of view of quantum optics, SHG (which is a particular case of SFG) is a two step process. Firstly, two *photons* of the fundamental beam interact with the molecular assemble of the nonlinear material. These quanta of light take the molecular assemble to a virtual or intermediate state, which is not an Eigenstate of the molecular assemble. Secondly, due to the interaction between the fundamental photons and the material, the density of photons in their initial modes is affected, causing the annihilation of two $h\nu_1$ photons and the creation of one $h\nu_2 = 2h\nu_1$ photon during the instantaneous relaxation of the molecular assemble, where both energy and momentum are conserved. Due to the Heisenberg's uncertainty principle the Eigenstates of the molecular assemble are not affected during the two steps necessary for SHG (and in general for second order nonlinear wave-mixing processes), since the steps described above occur simultaneously and instantaneously [87].

[13] In a particular type of nonlinear crystals, Δk can be tuned by changing the temperature of the crystals.

[14] In quantum optics is known as the parametric approximation.

2.5 Optical parametric amplification

The nature of the *creation* of light during the interaction of an electromagnetic field with a non-linear crystal is non-classical rather than classical. According to Strekalov and Leuchs [88] "*the term non-classical concerns light whose properties cannot be explained by classical electrodynamics and which requires invoking quantum principles to be understood*". The (non-degenerate) optical parametric amplifier (OPA), an essential optical device for the research presented at hand, is the most colorful and evident manifestation, respect to other devices based on second order non-linear effects, of the discreteness of photons, due to the fact that the amplification of a weak *signal* beam occurs alongside the *creation* of a so called *idler* beam. For this reason a short description of the quantum mechanical model proposed by Louisell et al. [89], which was originally conceived for parametric amplification of radio waves and readily adapted to optical frequencies by Mollow and Glauber [90], will be given.

The main components of an OPA, see Figure 2.7 panel A, are two optical beams: a very intense one, the pump, which prompts the amplification process and the beam to be amplified, the signal, which is usually weak. The third main component of the OPA is a dielectric material, e.g. a second order non-linear crystal, where the amplification takes place. In this dielectric material the pump beam acts as a modulation source, coupling the already present signal mode to another inexistent electromagnetic mode, the idler. This coupling, induced by modulation of the dielectric constant of the material by the pump beam, results in an unceasing transfer of energy from the pump field to the signal and idler modes producing not only amplification of the (previously) weak signal beam but also *creation* and amplification of the idler beam [65, 85, 86, 89, 90]. It is worth mentioning that the signal beam keeps its initial phase. Thus, in order to fulfill the energy conservation law the sum of the frequencies of the coupled modes, i.e. the signal (ω_a) and idler (ω_b), must be equal to the frequency of the pump $\omega = \omega_a + \omega_b$, see Figure 2.7 panel B.

Before discussing the coupling of modes in the OPA, it is important to recall that the nature of a single uncoupled optical mode of the electromagnetic field can be described in the same way as a unitary mass harmonic oscillator, in which the electric and magnetic fields impersonate the canonical position and momentum [91]. Each oscillator is described by a non-Hermitian operator $\hat{a}$, termed as annihilation operator, and its adjoint $\hat{a}^\dagger$, known as the creation operator. These operators are mathematically expressed as

$$\hat{a} = \left(\frac{\hat{q}}{Q_0} + i\frac{\hat{p}}{P_0}\right), \quad \hat{a}^\dagger = \left(\frac{\hat{q}}{Q_0} - i\frac{\hat{p}}{P_0}\right) \tag{2.34}$$

Where $\hat{q}$ and $\hat{p}$ are operators acting, respectively, as canonical position and momentum of the mode whereas $Q_0 = \sqrt{2\hbar/\omega}$ and $P_0 = \sqrt{2\hbar\omega}$ are characteristic constants of the unitary

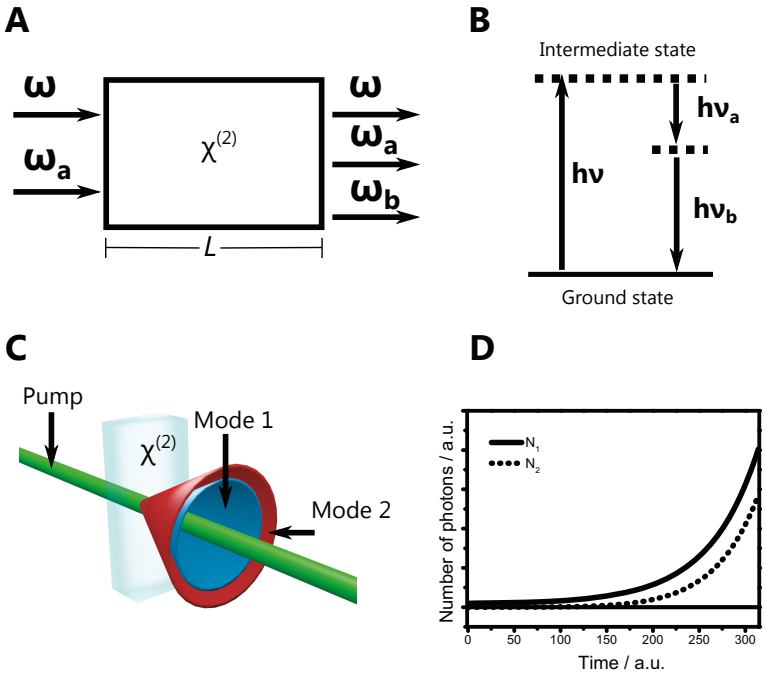

Fig. 2.7 A) Experimental geometry of the OPA. An intense pump field propagating through a non-centrosymmetric crystal, alongside a weak signal beam, would induce a coupling between two resonant modes. B) Energy level representation of the OPA. Note that the energy of the idler beam is given $h\nu_b = h\nu - h\nu_a$, therefore, this configuration is known as DFG. C) A schematic representation of the optical parametric fluorescence, where an intense pump beam creates colorful cones of light. D) Numerical solution to Equations 2.42. Note the exponential growth of the resonant modes which is symmetric along the process, fulfilling the conservation law of the number of quanta contained in the resonant modes.

mass oscillator. The quantization of the electromagnetic mode is achieved by setting the canonical variables, i.e. $\hat{q}$ and $\hat{p}$, as operators satisfying the commutations relations $[\hat{q},\hat{q}] = [\hat{p},\hat{p}] = 0$ and $[\hat{q},\hat{p}] = i\hbar$. Similarly, the annihilation and creation operators follow $[\hat{a}^\dagger,\hat{a}^\dagger] = [\hat{a},\hat{a}] = 0$ and $[\hat{a},\hat{a}^\dagger] = 1$. Therefore, the Hamiltonian of an independent or uncoupled electromagnetic mode can be expressed in terms of the annihilation and creation operators as [83]

$$\hat{H} = \hbar\omega\left(\hat{a}^\dagger\hat{a} + \frac{1}{2}\right) \tag{2.35}$$

The eigenstates of this Hamiltonian are the n-quantum states, which can be generated by the iterative action of the creation operator $\hat{a}^\dagger$

$$|n\rangle = \frac{\left(\hat{a}^\dagger\right)^n}{\sqrt{n!}}|0\rangle \tag{2.36}$$

and the annihilation operator $\hat{a}$

$$\sqrt{n}\,|n-1\rangle = \hat{a}\,|n\rangle \tag{2.37}$$

with the ground state $|0\rangle$ of the oscillator satisfying $\hat{a}\,|0\rangle = 0$, because there is no way for further annihilation as no quanta is present in this state. Since $\hat{H}$ is a Hermitian operator, the number states n are orthogonal, i.e. $\langle n_l | n_j \rangle = \delta_{l,j}$ and form a complete set of basis:

$$\sum_{n=0}^{\infty} |n\rangle \langle n| = 1 \tag{2.38}$$

In the OPA, the signal and idler modes also exhibit a dynamical behavior alike to a unitary mass harmonic oscillator therefore they can be described with annihilation and creation operators [89, 90], being $\hat{a}$ and $\hat{b}$ the annihilation operators for the signal and idler modes, respectively, and their corresponding adjoints. Thus, these operators must satisfy the following canonical commutations:

$$\left[\hat{a}(t), \hat{a}^{\dagger}(t)\right] = \left[\hat{b}(t), \hat{b}^{\dagger}(t)\right] = 1 \tag{2.39}$$

Since each of the radiation modes is independent of the others, in this case the signal and idler, the creation and annihilation operators of different oscillators commute:

$$\left[\hat{a}(t), \hat{b}(t)\right] = \left[\hat{a}(t), \hat{b}^{\dagger}(t)\right] = 0 \tag{2.40}$$

The pump beam, however, is assumed to be set in a high amplitude coherent state, making the omission of the depletion mechanism and quantum fluctuations feasible [92]. In addition, this approximation, namely, the parametric approximation, allows to treat the pump mode classically, i.e. as a c-number. Louisell et al. [89] demonstrated that the Hamiltonian for the parametric amplification process involving two coupled non-degenerated modes is given by

$$\begin{aligned} \hat{H}(t) =& \hbar\omega_a \hat{a}^{\dagger}(t)\hat{a}(t) + \hbar\omega_b \hat{b}^{\dagger}(t)\hat{b}(t) \\ & -\hbar\kappa \left[\hat{a}^{\dagger}(t)\hat{b}^{\dagger}(t)\exp(-i\omega t) + \hat{a}(t)\hat{b}(t)\exp(i\omega t)\right] \end{aligned} \tag{2.41}$$

where the coupling constant $\kappa \propto \chi^{(2)} E_p$, with E_p representing the amplitude of the pump field. As can be seen from Equation 2.41, the application of the intense "pump" field, oscillating at a frequency ω, will lead the resonant modes, i.e. the signal and idler, to endure forced and coupled oscillations. Other non-linear parametric processes can be explained by (almost) the same Hamiltonian shown in Equation 2.41 [91, 93, 94].

As a rule of thumb for the experimentalist, the amplification of the signal beam is readily obtained once the pump beam can create, by itself and in the absence of the signal beam, the

so called parametric fluorescence, where the creation of "cones" of quanta of different modes takes place, this is depicted in Figure 2.7 panel C [95].

To follow the time dependence of the operators $\hat{a}$ and $\hat{b}$, and their respective adjoints, they are expressed in terms of their corresponding Heisenberg´s equations of motion which, together with the commutation relations expressed in Equations 2.39 and 2.40, read:

$$\begin{aligned} i\hbar\frac{d\hat{a}(t)}{dt} &= \omega_a\hat{a}(t) - \kappa\hat{b}^\dagger(t)\exp(-i\omega t), \quad \frac{1}{i}\hbar\frac{d\hat{a}^\dagger(t)}{dt} = \omega_a\hat{a}^\dagger(t) - \kappa\hat{b}(t)\exp(i\omega t) \\ i\hbar\frac{d\hat{b}(t)}{dt} &= \omega_b\hat{b}(t) - \kappa\hat{a}^\dagger(t)\exp(-i\omega t), \quad \frac{1}{i}\hbar\frac{d\hat{b}^\dagger(t)}{dt} = \omega_b\hat{b}^\dagger(t) - \kappa\hat{a}(t)\exp(i\omega t) \end{aligned} \tag{2.42}$$

The Equations shown in 2.42 are very useful since the number operator $\hat{N}_a(t) \equiv \hat{a}^\dagger(t)\hat{a}(t)$ and $\hat{N}_b(t) \equiv \hat{b}^\dagger(t)\hat{b}(t)$, when measured, returns the eigenvalue of a particular n-sate, which can be rationalized as the number of quanta in that state [83]. Thus, with the numerical integration of Equations 2.42 and the definition of the number operators, the temporal evolution of the number of quanta (or photons) of the two modes in the OPA can be calculated, see Figure 2.7 panel D. Note how the photons contained in the idler mode starts with zero, growing exponentially and symmetrically with the signal beam.

To obtain an analytical description for the number of photons in the signal and idler modes, Mollow and Glauber proposed to obtain the second order derivative of the products $\hat{a}^\dagger(t)\hat{a}(t)$ and $\hat{b}^\dagger(t)\hat{b}(t)$, i.e. $\hat{N}_a(t)$ and $\hat{N}_b(t)$. By means of Equations 2.42 and a lengthy algebraic calculation the next expressions are obtained:

$$\begin{aligned} \frac{d^2}{dt^2}\hat{N}_a(t) &= 2\kappa^2\left[2\hat{N}_a(t) + 1 - \hat{M}\right] \\ \frac{d^2}{dt^2}\hat{N}_b(t) &= 2\kappa^2\left[2\hat{N}_b(t) + 1 + \hat{M}\right] \end{aligned} \tag{2.43}$$

where $\hat{M} = \hat{N}_a(0) - \hat{N}_b(0)$. Since $\hat{M}$ commutes with the Hamiltonian, $\hat{M}$ is a constant of motion of the system, i.e. it does not change over time, which means that the difference of quanta contained in the two modes remains constant. Thus, it is a trivial matter to show that the solutions for 2.43 include hyperbolic functions, similar[15] to those obtained with the classical description:

[15]It should be noted that in the classical description of the coupling between optical fields in non-linear materials presented above, the propagation coordinate is the independent variable whereas in the quantum model discussed the independent variable is the time.

$$\begin{aligned}\hat{N}_a(t) &= \frac{d\hat{N}_a(0)}{dt}\frac{1}{2\kappa}\sinh(2\kappa t) + \left[\hat{N}_a(0) + \frac{1}{2}(1-\hat{M})\right]\cosh(2\kappa t) - \frac{1}{2}(1-\hat{M}) \\ \hat{N}_b(t) &= \frac{d\hat{N}_b(0)}{dt}\frac{1}{2\kappa}\sinh(2\kappa t) + \left[\hat{N}_b(0) + \frac{1}{2}(1+\hat{M})\right]\cosh(2\kappa t) - \frac{1}{2}(1+\hat{M})\end{aligned} \tag{2.44}$$

2.6 Linear and Nonlinear microscopy

2.6.1 Imaging fundamentals

Consider a coherent monochromatic optical perturbation propagating in space. The perturbation is traveling along the (positive) z direction, as depicted in Figure 2.8, and is assumed that such perturbation satisfies the wave equation, its frequency ω is known and that it is described by:

$$u(x,y,t) = \Re\{U(x,y)\exp(-j\omega t)\} \tag{2.45}$$

Due to the fact that the temporal evolution of $u(x,y,t)$ is already known, the space phasor $U(x,y)$ complements the information contained on $u(x,y,t)$ by describing the distribution of the perturbation in space. Let us assume that during its propagation the perturbation encounters a diffracting aperture located on a plane (x_1,y_1) which is normal to z. Relying on the fact that every point of the wave front of the perturbation is the result of a wavelets superposition (as suggested by the Huygens principle), the disturbance reaching a point on a second plane (x_2,y_2) can be computed using the Fresnel approximation of the diffraction integral [96, 97]:

$$U_2(x_2,y_2) = \frac{\exp(jkz)}{j\lambda z}\iint_{-\infty}^{\infty} U_1(x_1,y_1)\exp\left(\frac{jk}{2z}\left[(x_2-x_1)^2+(y_2-y_1)^2\right]\right)dx_1\,dy_1 \tag{2.46}$$

Where $U_1(x_1,y_1)$ and $U_2(x_2,y_2)$ are complex functions of position describing the field distribution on the planes (x_1,y_1) and (x_2,y_2) respectively. It can be verified that Equation 2.46 is derived from the Rayleigh-Sommerfield diffraction formula by using the binomial expansion theorem. Another practical form of Equation 2.46 can be obtained if the exponential containing the quadratic image coordinate terms is factored out from the integrand:

$$\begin{aligned} U_2(x_2,y_2) = \frac{\exp(jkz)}{j\lambda z}\exp\left[\frac{jk}{2z}\left(x_2^2+y_2^2\right)\right]\iint_{-\infty}^{\infty} U_1(x_1,y_1)\left\{\exp\left[\frac{jk}{2z}\left(x_1^2+y_1^2\right)\right]\right\} \\ \exp\left[\frac{-jk}{z}(x_2x_1+y_2y_1)\right]dx_1\,dy_1 \end{aligned} \tag{2.47}$$

This alternative form of the Fresnel diffraction integral is very useful to describe the distribution of the perturbation on the focal plane of a lens.

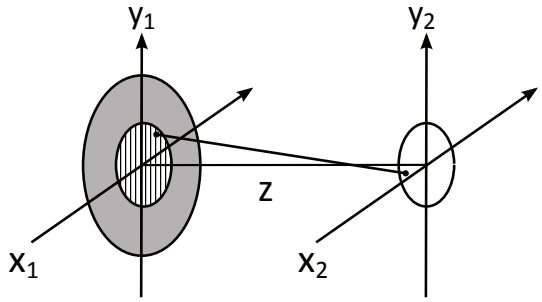

Fig. 2.8 Assumed diffraction geometry. A diffracting aperture is located on the plane (x_1, y_1). Once the disturbance has propagated over this aperture the incident radiation will be diffracted on the observation plane formed by (x_2, y_2).

In order to describe the image formation process, it is necessary to mention the effects induced by one of the fundamental components of an optical system: the lens. Due to the fact that a lens is constructed with a dielectric material whose refractive index is higher than the refractive index of the free space and that it possesses two spherical surfaces, an electromagnetic perturbation propagating through a lens suffers a phase delay. From this, any incoming perturbation $U_i(x,y)$ that propagates through a lens located in the plane (x,y) would result in an ongoing transformed perturbation [96–98]:

$$U_o(x,y) = U_i(x,y)P(x,y)\exp\left[\frac{-jk}{2f}\left(x^2+y^2\right)\right] \tag{2.48}$$

Where f is the focal length of the lens and $P(x,y)$ is the pupil function used to account for its finite dimensions. The pupil function with a perfect radial symmetry is defined as:

$$P(x,y) = \text{circ}\,(r) = \begin{cases} 1, & \text{if } r \leq \sqrt{x^2+y^2} \\ 0, & \text{if } r > \sqrt{x^2+y^2} \end{cases} \tag{2.49}$$

r is the radius of the pupil. For future reference, the Fourier transform of the (radially symmetric) pupil function is

$$\mathscr{F}\{\text{circ}\,(r)\} = \frac{J_1(2\pi\rho)}{\rho} \tag{2.50}$$

being $\rho = \sqrt{\xi^2+\eta^2}$. ξ and η are, respectively, the abscissas and ordinates of an arbitrary plane while J_1 a Bessel function of first order.

Consider a transparency located in the plane (x_1, y_1) and assume that it is illuminated uniformly with a unitary monochromatic plane wave. The amplitude transmittance $t(x_1, y_1)$ of the transparency will propagate through space over a distance d_1 and will reach a lens located

on a second plane (x_2, y_2). Subsequently the lens will focus the light onto an observation plane (x_3, y_3), as shown in Figure 2.9.

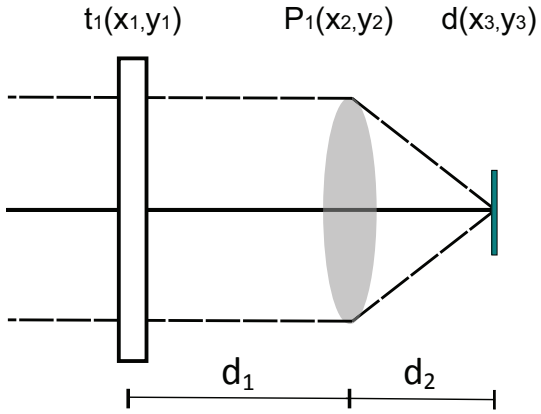

Fig. 2.9 Fundamental imaging geometry. The transmitted light from an illuminated transparency is collected and focused on an observation screen by a lens.

Using Equation 2.46 twice and including the phase transformation induced by the lens to the propagating perturbation, the radiation reaching the plane (x_3, y_3) on Figure 2.9 can be expressed as:

$$\begin{aligned} U_3(x_3,y_3) = &-\frac{\exp\left[jk\left(d_1+d_2\right)\right]}{\lambda^2 d_1 d_2}\iiiint_{-\infty}^{\infty} t(x_1,y_1)P(x_2,y_2) \\ &\times \exp\left\{-jk\left[x_2\left(\frac{x_1}{d_1}+\frac{x_3}{d_2}\right)+y_2\left(\frac{y_1}{d_1}+\frac{y_3}{d_2}\right)\right]\right\} \\ &\times \exp\left[\left(\frac{jk}{2d_1}\right)\left(x_1^2+y_1^2\right)\right]\exp\left[\left(\frac{jk}{2d_2}\right)\left(x_3^2+y_3^2\right)\right] \\ &\times \exp\left[\left(\frac{jk}{2}\right)\left(x_2^2+y_2^2\right)\left(\frac{1}{d_1}+\frac{1}{d_2}-\frac{1}{f}\right)\right] dx_2\,dy_2\,dx_1\,dy_1 \end{aligned} \tag{2.51}$$

If the *"lensmaker equation"* is recognized in the fourth exponential of the integrand of Equation 2.51 and assuming that the condition $1/d_1 + 1/d_2 = 1/f$ is fulfilled, followed by integration over the second plane, i.e. (x_2, y_2), Equation 2.51 can be recast as [96, 97]:

$$\begin{aligned} U_3(x_3,y_3) = &-\frac{\exp\left[jk\left(d_1+d_2\right)\right]}{\lambda^2 d_1 d_2}\iint_{-\infty}^{\infty} t(x_1,y_1)h(X,Y) \\ &\times \exp\left[\left(\frac{jk}{2d_1}\right)\left(x_1^2+y_1^2\right)\right]\exp\left[\left(\frac{jk}{2d_2}\right)\left(x_3^2+y_3^2\right)\right] dx_1\,dy_1 \end{aligned} \tag{2.52}$$

With $X = x_1 + \frac{x_3}{M}$ and $Y = y_1 + \frac{y_3}{M}$. Then, $h(X,Y)$ is simply the Fourier transform of the pupil function:

$$h(X,Y) = \iint_{-\infty}^{\infty} P(x_2,y_2) \exp\left\{-\frac{jk}{d_1}\left[(x_2X) + (y_2Y)\right]\right\} dx_2\, dy_2 \tag{2.53}$$

Where M is the magnification of the optical system and is defined as:

$$M = -\frac{d_2}{d_1} \tag{2.54}$$

A fundamental effect for the imaging theory is observed if the transparency consists of a single *point-like* object, i.e. $t(x_1,y_1) = \delta(x_1)\delta(y_1)$. After substitution of the point-object transmittance in Equation 2.52, followed by integration over (x_1,y_1), it is clear that the image of a point object, termed the point spread function (PSF), is nothing else than the Fourier transformation of the pupil function multiplied by a constant. The intensity distribution on the image plane will be given by the jinc function, see Equation 2.50, and in turn, it will form an Airy-disk pattern. This effect determines the minimum distances between objects an optical system, e.g. a microscope or telescope, is able to resolve [66].

On a high quality imaging system the intensity distribution resulted by an arbitrary point source on the object plane, i.e. the absolute square of the PSF, must be spatially distributed around the corresponding exact image produced by such punctual source. If this condition were not fulfilled, the imaging system would produce blurred images. Then, assuming that only a small portion on the object plane truly contributes to the formed image, the exponential term with object coordinates (x_1,y_1) on Equation 2.52 can be replaced as follows [96]:

$$\exp\left[\frac{jk}{2d_1}\left(x_1^2 + y_1^2\right)\right] \rightarrow \exp\left[\frac{jk}{2d_1}\left(\frac{x_3^2 + y_3^2}{M^2}\right)\right] \tag{2.55}$$

This allows to further simplify Equation 2.52 since with this assumption only two terms depend on the object coordinates. The obtained expression to describe the field distribution on the image plane is outstanding due to the fact that it consists of just an integral convolution between the object and the PSF of the system multiplied by quadratic phase factors. This implies that every point in the object plane would be replaced on the image plane by a blurred image of that point:

$$\begin{aligned} U_3(x_3,y_3) = &-\frac{\exp\left[jkd_1\left(1+M\right)\right]}{\lambda^2 d_1^2 M} \exp\left[\frac{jk}{2d_1 M}\left(1+\frac{1}{M}\right)\left(x_3^2 + y_3^2\right)\right] \\ &\iint_{-\infty}^{\infty} t(x_1,y_1) h(X,Y)\, dx_1\, dy_1 \end{aligned} \tag{2.56}$$

The imaging process can be classified accordingly to the statistical nature of the detected light, i.e. fluctuations on the intensity amplitude and phase [99, 100]. When the illumination impinging on the detector, located at the image plane, is coherent the intensity distribution on the image plane can be expressed as:

$$I(x_3, y_3) = |h \otimes t|^2 \tag{2.57}$$

while for the case of incoherent illumination the intensity is given by:

$$I(x_3, y_3) = |h|^2 \otimes |t|^2 \tag{2.58}$$

where the symbol "$\otimes$" denotes convolution. Nonetheless, the coherence degree on the imaging process depends on several factors, including the sample-object itself, the size and type of detector and the properties of the optical elements conforming the system [101].

It is important to mention that imaging with a pulsed laser beam, whose individual pulses time duration has magnitudes on the femtosecond time scale, might be different to imaging with a continuous and monochromatic laser beam since in the former the (intensity) diffraction pattern is the sum of all the contributions from the different spectral components of the pulse, resulting on a spatial distribution of the intensity in close regions of the focus, i.e.: dispersion might play an important roll on the diffraction of pulsed illumination [101, 102]. Two effects appear due to the chromaticity of the lens and have direct impact on the pulse shape. Such effects are the propagation time difference (PTD) and group velocity dispersion (GVD). PTD induces a chirp to the light pulse that depends on the radial coordinates of the lens aperture while GVD sets a constant chirp on the pulse (see Figure 2.10). The induced chirp on the pulse also affects the performance of systems with time resolving capabilities, e.g. a pump-probe micro-spectroscopy set-up, since the temporal resolution is decreased as the temporal width of the pulses involved in the experiment is stretched. Due to the fact that the chromaticity of the optical system influences the diffraction of the incoming pulse, PTD might be reduced or neglected if aberration free optics are employed, e.g. by means of achromatic doublets [103, 104]. To avoid GVD, and thus cancel its effects on diffraction, pre-chirping or dispersion compensation of the incoming pulse needs to be implemented on the system [101–104].

2.6.2 The laser scanning microscope

On a laser scanning microscope (LSM) light is focused onto an object sample producing a diffraction limited spot, where the transmitted intensity corresponding to that particular object point is recorded, digitized and stored as an element of a 2-D matrix which in turn

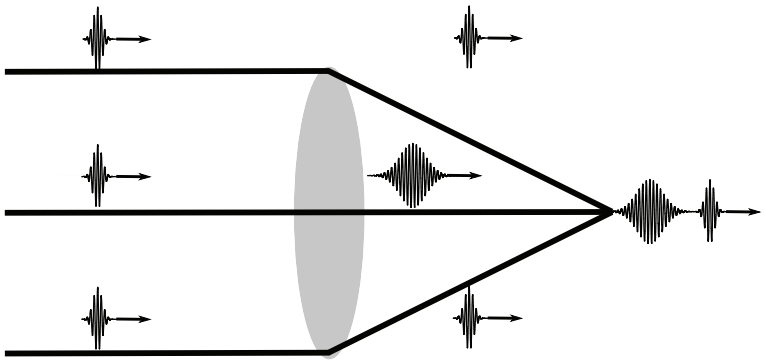

Fig. 2.10 Dispersion effects induced on an ultrashort laser pulse after it propagates through an optical lens with chromatic aberrations.

forms a pixel. Thus, the imaging process on the LSM results from *scanning* the object in a raster-pattern. Such scanning can be done either by moving the sample or simply by changing optically the spot position [98, 101, 105]. On Figure 2.11 panel a the conventional microscope geometry is shown while on panels b-d the three possible geometries of a transmission LSM are depicted and are categorized as "Type 1". It should be acknowledged that the detectors of Type 1 microscopes are incoherent and possess finite dimensions. From Parseval's theorem (or by the energy conservation law) the systems depicted on Figure 2.11 panels b-d are all equivalent, i.e.: the total intensity on the detector plane for all Type 1 LSM configurations is the same [96, 98, 106, 107]. Furthermore, imaging with Type 1 microscopes is equivalent to imaging with conventional imagery (or non-scanning microscopes) if the lenses used in the LSM are replaced by the condenser and the objective of the conventional microscope [107]. Applying the formalism presented in the last section, particularly Equations 2.47 and 2.48, it can be verified that the intensity on the focal plane of a Type 1 LSM whose illumination is a coherent light source is given by Equation 2.57 while the corresponding intensity on the detector plane when an incoherent light source is employed is described by Equation 2.58 [98, 106].

A different kind of LSM is created when a point-like detector is employed on a Type 1 LSM, see Figure 2.12. A hybrid system is obtained and it is termed Type 2 microscope or confocal laser scanning microscope (CLSM) to distinguish it from Type 1 microscopes due to the fact that the imaging characteristics between them are different [98, 108–111]. When coherent laser light is employed, the intensity at the detector of a CLSM can be expressed as [98, 108]:

$$I(x_3, y_3) = |h_1 h_2 \otimes t|^2 \tag{2.59}$$

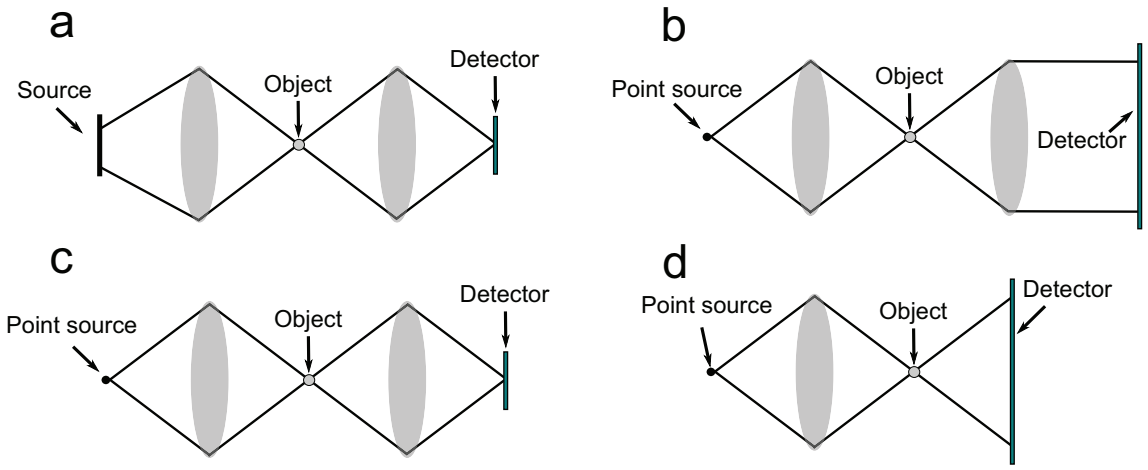

Fig. 2.11 A) Conventional microscope. B)-D) Type 1 LSM geometries. On panels B and C it is assumed that the lenses building each microscope posses the same numerical aperture and pupil function. The detector on Type 1 microscopes is incoherent (i.e. no information about the phase of the detected signal is available) and has finite size dimensions.

Has been reported that the same results are obtained using alternatives to the point-like detector on a Type 2 microscope, i.e. employing coherent detectors [112] or heterodyne detection scheme [113]. Type 2 microscopes provide superior spatial resolution at optical frequencies compared to that obtained with Type 1 microscopes [98, 101, 108–110]. The last statement can be inferred by inspection of Equations 2.57 and 2.59. The spatial confinement of the central peak of the PSF on a CLSM is reduced by 37 % compared to that of Type 1 microscopes, alongside a reduction of the side lobes of the PSF [98]. Such reduction on the sidelobes enables the possibility to use annular objectives and thus increase even more the lateral resolution [114]. Furthermore, the depth of focus on a CLSM is reduced, a result of a discrimination of out of focus light [98, 101, 108, 110].

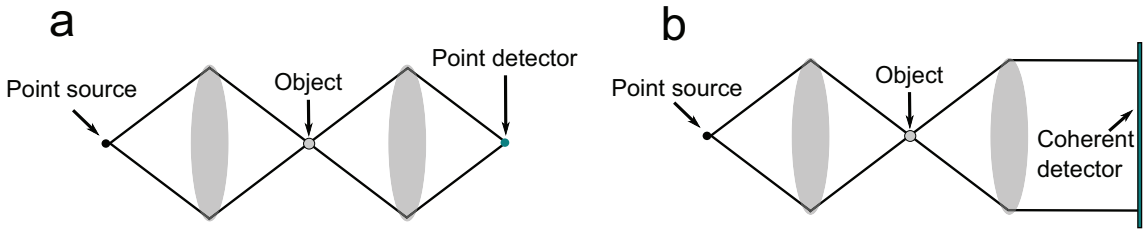

Fig. 2.12 Type 2 LSM. a) LSM geometry employing a detector with infinitesimal dimensions. b) LSM whose detector has information about the phase of the incoming light.

2.6.3 Nonlinear microscopy

Nonlinear microscopy summarizes a set of imaging techniques that exploit the nonlinear response of an object subjected to intense optical fields. As discussed in Section 2.2, the response of a material system to intense optical fields is accompanied by a re-emitted signal, whose source is a time varying polarization nonlinear term $P^{(NL)}(r,t)$, see Equations 2.4 and 2.6. Thus, "nonlinear microscopy" describes those imaging techniques that utilize the signal derived from a nonlinear optical process to generate the contrast of an image, resulting in a map of the nonlinear susceptibility [115–117]. Recall that the contrast on conventional or linear microscopy relies solely on variations of the linear refractive index (which in turn might scatter or induce changes to the phase of the illumination), path lengths or inhomogeneities of the concentration of a particular absorbent agent (extrinsic or intrinsic) of an object or specimen [66].

It is common to nonlinear microscopy techniques to imaging using only the contrast generated by the nonlinear response of endogenous molecules which are intrinsic to the sample. This implies that untreated or unstained specimens can be analyzed with out any possible perturbation induced by exogenous agents [118–125]. Furthermore, it is worth mentioning that some nonlinear microscopy techniques are able to imaging non-emissive objects. Due to the fact that the nonlinear signal is generated only in the focal volume, nonlinear microscopy techniques have inherent optical sectioning capabilities with no need of a confocal pinhole. Therefore, nonlinear spectroscopical techniques have been merged with microscopy, e.g CARS, SHG, THG, two photon fluorescence, pump-probe microscopy [126–131], among others.

Innovative work on the nonlinear microscopy field was done in 1978 by Gannaway and Sheppard [132]. They developed a LSM whose illumination consisted of a CW neodymium YAG laser and its contrast was formed by SHG signals to imaging crystals, revealing inherent characteristics of the sample unobservable to conventional or linear microscopy. However, the authors of the novel SHG microscope were not able to imaging biological specimens due to the high average powers required to induce nonlinear responses [132]. This might be the reason why this outstanding work did not have a large impact on the community. Nonetheless, this work revealed the potential and challenges of nonlinear microscopy: the confinement of the generation of a nonlinear signal to the focal volume of an objective allowing chemical imaging and optical sectioning of a specimen alongside the undesirable laser heating effects which lead to photodamage and/or phototoxicity on the sample. Webb et al. published a seminal work [133] in 1990, parallel to a patent assigned to the Cornell Research Foundation [134], which indeed marked the beginning of a new era of nonlinear microscopy applied to biosciences. They equipped a LSM with a mode-locked dye laser, spectrally centered

at 630 nm with femtosecond pulses (ca. 100 fs pulse width). They focused such pulses on live pig kidney cells (LLC-PK-1) stained with Hoechst 33258 (a DNA marker) recording fluorescence excited through two-photon absorption. They succeed to image live organisms, i.e. pig kidney cells, by reducing the average power delivered to the sample and taking advantage of the large peak powers attainable with femtosecond pulses [59]. Ever since the dominant trend in the scheme of a nonlinear microscope, for biological and material sciences, includes a LSM and a sub-picosecond pulsed laser source. Of course alternatives to this configuration have been reported, including nonlinear multifocus imaging [135], nonlinear structured-illumination microscopy [136] and even hybrid systems of optical and atomic force microscopy [137].

Min Gu and Sheppard [138, 139] compared (theoretically) the image formation of the conventional fluorescence CLSM with its nonlinear analogue, i.e. a LSM using as contrast the fluorescence signal derived from two-photon excitation, which is an incoherent nonlinear signal related to $\chi^{(3)}$ [65]. They concluded that two-photon fluorescence microscopy has lower imaging potential compared to its linear analogue. However, experimental work [140–142] comparing this two microscopes in highly scattering environments, i.e. biological tissues, indicates that the nonlinear version has superior imaging capabilities compared to its linear version. This discrepancy between experimental and theoretical results has been attributed to the fact that the theoretical analysis was done with an ideal point detector, which is in practice unattainable [143]. Furthermore, Naoki Fukutake [144–146], W. Rudolph and co-workers [147] determined that the lateral and depth resolution in nonlinear microscopy depends not only on the wavelengths of the radiation involved and numerical apertures of the objectives. They rather claimed that the spatial resolution improves as the order j of the nonlinear process used as the contrast increases. This was attributed to the fact that the effective PSF (ePSF) of a nonlinear microscope changes as ePSF^j, leading to narrower ePSF compared to that of microscopes employing nonlinear processes with inferior j.

Webb et al. [147, 148] proposed two expressions to estimate the diffraction limited lateral (r_{xy}) and axial (r_z) resolution on a nonlinear microscope. r_{xy} and r_z correspond to the $1/e$ widths of the Gaussian distribution of the excitation intensity whereby a 36.78% of the maximum intensity peak is achieved on the x-y and z axis, respectively. Thus, such expressions can be used to quantitatively describe the resolving power attainable with a nonlinear microscope and were derived from the work reported on reference [149] and fits of the j^{th} power of the volume formed by the excitation intensity at the focal position.

$$r_{xy} \approx \begin{cases} \frac{0.320\lambda}{\sqrt{j}NA}, & \text{if } NA \leq 0.7 \\ \\ \frac{0.325\lambda}{\sqrt{j}NA^{0.91}}, & \text{if } NA > 0.7 \end{cases} \tag{2.60}$$

$$r_z \approx \frac{0.532\lambda}{\sqrt{j}} \left[\frac{1}{n - \sqrt{n^2 - NA^2}} \right] \tag{2.61}$$

Where n is the refractive index of the material and NA the numerical aperture of the excitation objective. Recall that for a pump-probe microscope $j = 3$. Thus with Equations 2.60 and 2.61 the explored volume V_{exc} is given by

$$V_{exc} = \pi^{\frac{3}{2}} r_{xy}^2 r_z \tag{2.62}$$

2.6.4 Pump-Probe Microscopy

As mentioned above, nonlinear microscopic techniques offer means to observe intrinsic properties of a sample that can not be observed with conventional microscopy. A particularly attractive characteristic of pump-probe microscopy is its ability to image emissive and non-emissive electronically excited chemical species. The data contained on a single pixel of a pump-probe image is the digitized value of the recorded signal derived from excited state absorption, stimulated emission or ground state bleach, i.e. the processes depicted in Figure 2.5. However, what really makes pump-probe microscopy unique among all the other nonlinear microscopy techniques is its capacity to imaging a sample at a specific time subsequent to photoexcitation in the femto second time regime. This, in principle, makes it possible to e.g. follow a photoinduced chemical reaction as function of both time and space. An application example of this concept is shown in Figure 2.13 [150]. Platinum octaethylporphyrin (PtOEP) crystals embedded into a polymer matrix appear transparent in a simple phase image, Panel A Figure 2.13. However, when the excited-state of PtOEP is attained by exciting at 535 nm and probed at different times subsequent to the first perturbation of the ground state with a second pulsed beam, in this case centered at 665 nm, images with chemical contrast as those shown in Figure 2.13 Panels B-D can be obtained. Note that this sort of images provides an estimation of the amounts of dye and its particular location on the sample and gives a notion on how the excited molecules evolve *in situ*.

Thus, modifications, which are far from being subtle, to the conventional infrastructure of the nonlinear microscope, including the addition of the femtosecond pulsed pump and probe laser beams, an optical delay stage and suitable detectors, make feasible pump-probe spectroscopy studies with high spatial resolution alongside nonlinear imaging as function

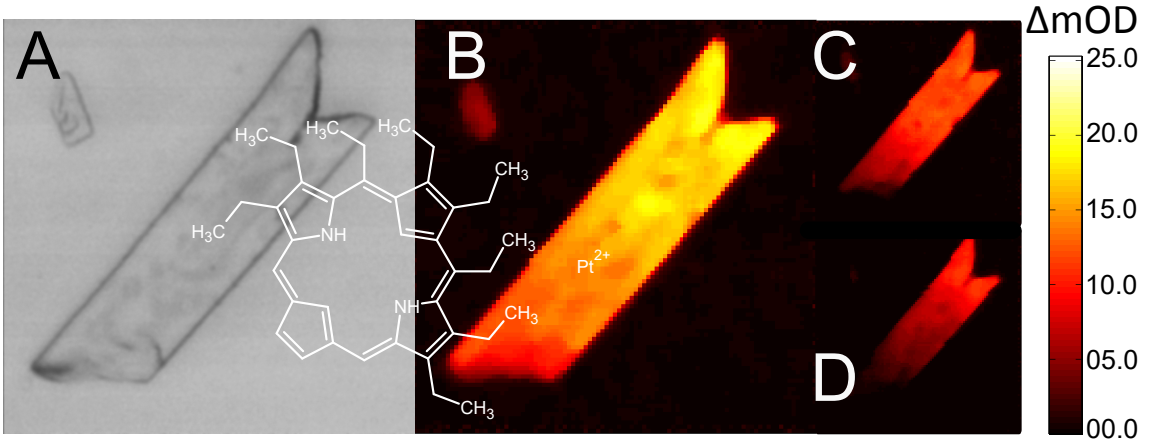

Fig. 2.13 Transient absorption imaging of PtOEP crystals embedded into a polymer matrix. A) Phase image, B-D) Transient-absorption images at $\Delta t = 0$, $\Delta t = 100$ and $\Delta t = 200$ ps respectively. The inset shows the molecular structure of PtOEP, $\lambda_{pump} = 535$ nm and $\lambda_{probe} = 665$ nm.

of time.[16] The nonlinear image and the kinetics traces recorded under optical diffraction limited resolution can provide conclusive and quantitative data describing the distribution of a molecule and its ultrafast dynamics in a particular location of a target medium.

The pump-probe microspectroscopic experiment can be seen different to the corresponding conventional spectroscopic technique due to the fact that in the former the induced nonlinear signals are generated exclusively in the focal volume, where, depending on the objectives, might have attoliter dimensions, see Equation 2.62. Therefore, a reduced total number of explored molecules compared to conventional pump-probe spectroscopic studies is expected. This situation might reveal molecular characteristics obscured by the dynamics observed in solution. In the ideal case, such reduction on the number of probed molecules leads the spectroscopist to a closer view of the single molecule dynamics [151]. Furthermore, in the case of molecules whose chemistry and physics depend strongly on environmental conditions, a drastically different ultrafast dynamics can be observed on model solvents and in target environments, for example, the photoinduced dynamics of Ruthenium-based drugs embedded in eukaryotic cells is different to the photoinduced dynamics exhibited by the same drug dissolved in model solvents [152]. This is deeply discussed in Sections 5.1 and 5.2 due to the fact that finding such differences was a milestone for the research at hand. Another interesting application scenario for pump-probe microspectroscopy lies in the biomedical sciences as diagnostics tool. Its high chemical sensitivity can be used to identify specific molecules inherent to certain diseases, e.g. eumelanin and pheomelanin content in skin cancer [153]. The Warren´s group has studied intensively human skin and conjunctival melanocytic lesions through pump-probe microspectroscopy [120, 153–155],

[16] Hereafter the localized spectroscopic studies with high spatial resolution will be termed microspectroscopic.

noticing that images of tissue recorded with pump-probe microscopy are highly correlated with histopathologic features recorded with adjacent hematoxylin and eosin-stained sections [120]. These findings might be used to gain complementary information in the melanoma diagnosis as well to increase accuracy of the diagnostic [154].

If a conventional LSM, such as those shown in Figure 2.14, assumed to be constructed with aberrations free optics, is arranged in a way that allows to realize pump-probe microspectroscopic experiments, the distribution of the electric fields interacting with the sample at the focal point of the excitation objective is described by the PSF corresponding to each field involved. Since the pump-probe experiment has a coherent nature, the intensity at the detector plane of a LSM corresponding to a particular time delay τ between pump and probe pulses at a specific scan position (x_s) can be expressed as [144–147]:

$$I(x_s,\tau)=\int_{-\infty}^{\infty}\left|\int_{-\infty}^{\infty}h_1(x_o)\gamma(x_o-x_s)h_2(x_i;x_o)dx_o\right|^2 P(x_i)dx_i \tag{2.63}$$

Where $P(x_i)$ is used to account for the finite dimensions and sensitivity of the detector, $h_2(x_i;x_o)$ expresses the impulse response of the collector objective for the re-emitted nonlinear signal. $\gamma(x_o)$ is a function related[17] to the third-order nonlinear susceptibility $\chi^{(3)}$ of the sample and can be though as an object amplitude transmittance. Thus, $\gamma(x_o)$ contains information about the concentration and distribution of molecules giving rise to the nonlinear signal. The optical perturbation at the focal point of the excitation objective is $h_1(x_o)=\prod_{i=1}^{3}E_i(x_o)$ [144, 147]. Here $E_i(x_o)$ represents the PSF experienced by the electric fields involved in the generation of the nonlinear signal, namely a probe field and a pump field, where the latter interacts twice with the sample in order to full-fill the phase matching condition of the pump-probe signal, see Section 2.2. If the system employs a point-like detector, i.e. $P(x_i)=\delta(x_i)$, Equation 3.1 takes the form of Equation 2.59, which is the expression used to describe the imaging process on a CLSM. Another situation occurs when the detector is considered to have finite dimensions and uniform sensitivity, i.e. $P(x_i)=1$. In this case the corresponding expression for the image formation is that of a coherent LSM, see Equation 2.57 [144, 147].

The pump-probe microscope has found several applications in many different fields, examples of such applications include organic optoelectronics, as a tool for investigations of graphene, nanostructures and drug delivery, and even as optical pathology tool. Some of these applications can be found in our review paper [131].

[17] Recall that in this analysis the scalar wave approximation for the involved electric fields is employed and that $\chi^{(3)}$ is a fourth rank tensor [65], which here has been assumed to be homogeneous over all the volume occupied by the object.

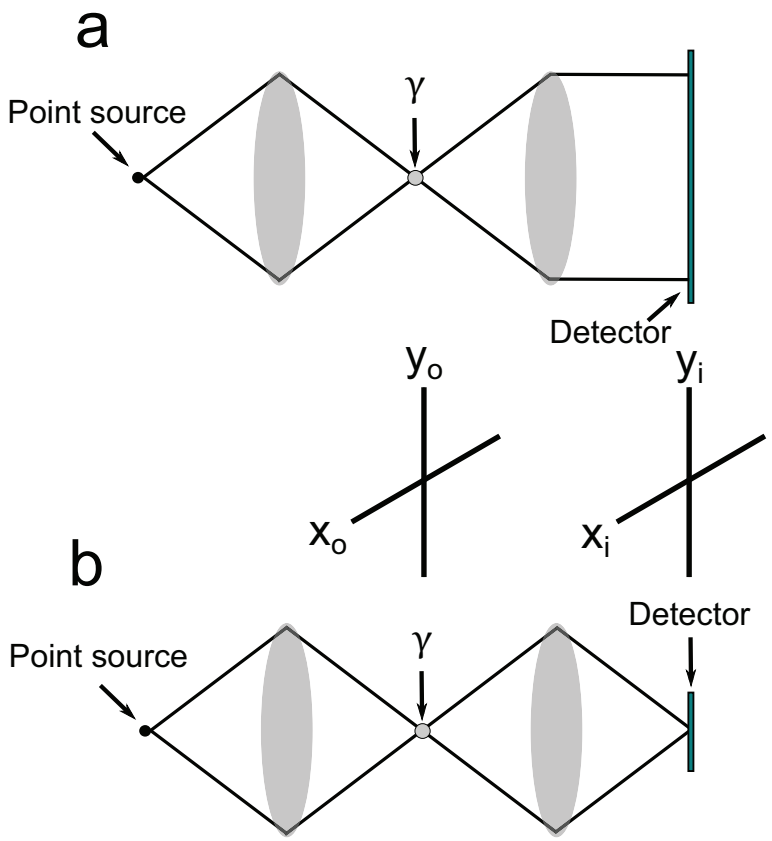

Fig. 2.14 Pump-probe microscopes in transmission mode employing a finite-size detector A) and a point-like detector B). In these idealized pump-probe microscopes there is information about the phase of the acquired signal, i.e. the detectors are coherent.

Chapter 3

Ruthenium polypyridyl complexes

3.1 Ruthenium polypyridyl complexes in the biosciences

The human kind has recognized the effectiveness of organometallic compounds against some cellular organisms that compromise the health condition of an individual since ancient times. The use of metal compounds as therapeutic agents dates back to 2500 bC with the usage of gold in medicine by the Chinese [156]. Nowadays the interest on metal complexes still is an intense research topic in the biosciences. Such interest includes naturally their use as therapeutic agents [2, 5, 12, 13, 16, 17], however their applicability has been extended. Some novel metal-based complexes have found to be useful also as non-toxic cellular markers [17, 157–160].

In modern times coordination compounds possessing transition metal centers with a d^6 electronic configuration coordinated to polypyridine ligands, and specially Ru(II)-based complexes due to their highly evolved chemistry, exhibit a set of interesting characteristics that might give them an important niche in the field of biosciences because they could be applied as novel biomedical imaging (luminescence-based) markers [17, 161], as photoactivated chemotherapeutic agents in photodynamic therapy [162], photoactivated chemotherapy [16] or even as alternative anti pathogen-agents to the worldwide used platinum-based drugs which are usually accompanied by undesired side effects and toxicity[1] [163] during the treatment [164]. The last statements are grounded on the fact that promising results have been obtained by research conducted on these coordination compounds embedded in biological environments by several work groups around the world over the last 30 years [162, 165–171]. Work reporting the use of Ru(II) and other d^6 transition metal ions coordinated to polypyridine ligands in biological environments, e.g. serum DNA or (eukaryotic and

[1] as nephro-, liver-, myelo-, gastrointestinal-, oto- toxicity

prokaryotic) cellular organisms, encompasses complex localization, binding mechanisms between complexes and target sites, cellular uptake, complex stability in target environments, photo-reactivity, toxicity essays and even antitumoral effects studies on living organisms [157–159, 162, 163, 170, 172–183]. Table 3.1 displays the most relevant work reporting the use of d^6 transition-metals on live and fixed cells, where the cellular models utilized include eukaryotic and prokaryotic organisms. As can be seen on Table 3.1, the application of these organometallic complexes has been oriented to therapeutics and to the design of cellular markers. Furthermore, note that the most prevalent metal core in cell related experiments is Ruthenium, which is a result of its well established chemistry. Nevertheless, it is undeniable that Ru(II) polypyridine complexes posses interesting characteristics that make them versatile molecules in the field of the biosciences. On one hand, some complexes are (photo-) chemically stable, non-toxic for the cells and their uptake and localization in cellular compartments can be chemically tuned by modifications of the ligands. In addition, they might posses emissive excited states with considerably high quantum yields, large Stokes shifts compared to that of organic molecules and relative long decay times (ca. 50 ns - 1 μs) [17, 157, 179]. These characteristics not only enable them as cellular markers but also provide some advantages over organic molecules during imaging experiments. For example, the re-absorption of the emitted light is minimized and the removal of the excitation wavelength and the inherent autofluorescence of the cells is easier given a large Stokes shifts [157, 160, 184]. On the other hand, by modifying the ligands, the molecules can be conceived to be inert until an external stimulus (a photon or a charged particle) acts on them, triggering a set of reactions, as ligand dissociation or charge/energy transfer, whose ultimate goal is to induce cytotoxicity [162, 177, 182]. Therefore, this type of complexes can be used in photoactivated chemotherapy (PACT), where according to Farrer [16] et al.[2] their possible anticancer action mechanisms can be classified as:

1. **Photodissociation and/or redox changes**, where the antipathogen mechanism is by inducing a chemical reaction of the metal complex or a moiety of the complex with a biological entity, as DNA or proteins, or by the release of reactive agents as NO or CO after optical excitation.

2. **Photosensitation**, the energy of the excited triplet state of the drug is used to produce the reactive and lethal singlet oxygen. Currently, the therapeutic application of this mechanism is photodynamic therapy.

Since visible light, in moderate doses, is not harmful for cells and tissues, photoactivated drugs provide the possibility to control both time and space of exposure, meaning that the

[2]They also enlisted photo thermal reactions, mainly induced by nanoparticles and quantum dots.

toxic species can be confined to specific time intervals and locations. Of course, all the drugs should be soluble in water or culture media and readily uptake by the cells, independently of the final application.

Table 3.1 EI = emission imaging studies, CU = cellular uptake studies, CT = cellular toxicity studies, EIT = time resolved emission imaging studies, AE = antitumoral activity evaluation, CI = cell imaging and IPC = Inhibition of pathogenic cells.

Applications of transition d^6 metal-centers coordinated to polypyridyl ligands on cells.				
Cell line	Complex	Experiments performed	Target application	Ref.
HeLa	$[Ir(dfpy)_2(bpy)]^+PF_6^-$ $[Ir(dfpy)_2(quqo)]^+PF_6^-$	EI and CT	CI	[185]
HeLa	$[Ir(N-C)_2(MebpyCONH)](PF_6)$	EI	CI	[186]
HeLa	$[Ir(pba)_2(bpyC6biotin)](PF_6)$ $[Ir(pba)_2(bpyTEGbiotin)](PF_6)$ $[Rh(pba)_2(bpyC6biotin)](PF_6)$	EI and CT	CI	[158]
MDCK	$[Ir(ppz)_2(dpq)](PF_6)$	EI and CT	CI	[158]
HeLa	$[Re(N-N)(CO)_3(pbte)](PF_6)$	CU, CT and EI	CI	[176]
Yeast and MCF-7	$[Re(bpy)(CO)_3PyCH_2Cl](PF_6)$	CU, CT and EI	CI	[175]
CHO and SP2	$[Os(bpy)_2(pic-arg_8)]^{10+}$ $[Ru(bpy)_2(pic-arg_8)]^{10+}$	CU, CT, EI and EIT	CI	[177]
HeLa	$[Ir(ppy)_2(tpphz)Ru(bpy)_2]^{3+}$ $[(F_2(ppy)_2Ir(tpphz)Ru(bpy)_2]^{3+}$	CU, CT and EI	CI	[171]
Lymphocytes, rat sperms and NCI-H460	$[Ru(phen)_2(dppz)]^{2+}$ $[Ru(bpy)_2(dppz)]^{2+}$	CU, CT and EI	CI	[159]
HeLa	$[Ru(DIP)_2dppz]^{2+}$	CU and EI	CI	[181]
MCF-7 and L5178Y-R	$[(phen)_2Ru(tpphz)Ru(phen)_2]^{4+}$ $[(bpy)_2Ru(tpphz)Ru(bpy)_2]^{4+}$	CU and EI	CI	[157]
HeLa (xenotransplanted into nude mice)	$[Ru(bpy)_2(HPIP)](ClO_4)_2$	CT and AE	IPC	[163]
HeLa, HepG2, BEL-7402, MG-63, MCF-7, A549, A549-CP/R and LO2	$[Ru(bpy)_2(HPIP)](ClO_4)_2$ $[Ru(bpy)_2(HMIP)](ClO_4)_2$ $[Ru(bpy)_2(HQIP)](ClO_4)_2$	CT and AE	IPC	[187]
HeLa, MCF7, U2OS, A2780, A2780-CP70 and MRC-5	$[Ru(dppz)_2(CppH)]^{2+}$ $[Ru(dppz)_2(CNHC)]^{2+}$	CT and EI	IPC	[183]
HeLa, MCF7, HFF, SQ20B and liver	$[Ru(dppz)_2(PIP)]^{2+}$	CT and EI	IPC	[188]
HL60 and A549	$[Ru(bpy)_2dmdpq]^{2+}$	CT and EI	IPC	[162]
MCF-7, EVSA-T, WIDR, IGROV, M19, A498 and H266	$[Ru-(azpy)_3](PF_6)_2$ $[Ru(azpy)_2(bpy)](PF_6)_2$	CT	IPC	[189]
DH5α	$[Ru(II)(terpy)(tmephen)Cl]^+$	CT	IPC	[180]
HT-29 and MCF-7	$[Ru(bpy)_3]^{2+}$ $[Ru(bpy)_2(phen)]^{2+}$ $[Ru(bpy)_2(dpq)]^{2+}$ $[Ru(bpy)_2(dppz)]^{2+}$ $[Ru(bpy)_2(dppn)]^{2+}$	CU and CT	IPC	[174]
HL-60 and ATCC 25175	$[Ru(bpy)_2(ippy)]^{2+}$	CU and CT	IPC	[182]

List of abbreviations used in Table 3.1:

- **dfpy** = 2-(2,4-difluorophenyl)pyridine.
- **bpy** = 2,2'-Bipyridine.
- **phen** = 1,10-phenanthroline
- **quqo** = 2-(2-quinolinlyl)quinoxaline.
- **N-N** = 4,7-diphenylphenanthroline.
- **pbte** = 3-ethylthioureidyl-5-(N-((2-biotinamido)ethyl)aminocarbonyl)pyridine.
- **arg8** = octaarginine.
- **ppy** = 2-phenyl-pyridine.
- **tpphz** = tetrapyrido[3,2-a:2',3'-c:3'',2''-h:2''',3'''-j]phenazine.
- **ppy** = 2- phenyl-pyridine.
- **dppz** = dipyrido[3,2-a:2',3'-c]phenazine.
- **DIP** = 4,7-diphenyl-1,10-phenanthroline.
- **HPIP** = 2-(2-hydroxyphenyl)imidazo[4,5-f][1,10]phenanthroline.
- **HMIP** = 2-(6-hydroxy-3,4-methylenedioxyphenyl)imidazo[4,5-f] [1,10]-phenanthroline.
- **CppH** = 2-(2'-pyridyl)pyrimidine-4-carboxylic acid.
- **CNHC** = 6-(2-(pyridin-2-yl)pyrimidine-4-carboxamido)hexanoic acid.
- **PIP** = 2-(phenyl)imidazo[4,5-f][1,10]phenanthroline).
- **dmdpq** = 3,6-dimethyl dipyrido[3,2-f:2',3'-h]- quinoxaline.
- **azpy** = 2-phenylazopyridine.
- **terpy** = 2,2';6',2''-terpyridine.
- **tmephen** = tetramethylphenanthroline.
- **dppn** = 4,5,9,16-tetraazadibenzo [a,c]naphthacene
- **dpq**=dipyrido[3,2-f:2',3'-h]quinoxaline
- **dpq**=dipyrido[3,2-f:2',3'-h]quinoxaline
- **ippy** = 2-(1-pyrenyl)-1Himidazo[4,5-f][1,10]phenanthroline
- **MebpyCONH** = Me-bpy-CONH-$C_{18}H_{37}$
- **bpyC6biotin** = 4-[(6-biotinamido)hexylaminocarbonyl]- 4'-methyl-2,2'-bipyridine.
- **bpyTEGbiotin** = 4-[(13-biotinamido-4,7,10-trioxa)tridecylaminocarbonyl]-4'-methyl-2,2'-bipyridine.
- **bpyC6biotin** = 4-[(6-biotinamido)hexylamino hexylaminocarbonyl]-4'-methyl-2,2'-bipyridine.
- **pba** = 4-phenylbutyrate.

3.2 Electronically excited states of Ru(II)-polypyridine complexes

Ru(II) cores have a d^6 electronic structure, allowing them to coordinate up to three bidentate polypyridine ligands. The paradigmatic bpy ligands are colorless molecules containing fully occupied σ_L and π_L donor orbitals and π_L^* acceptor orbitals [190]. The σ_L orbitals are mainly localized on the Nitrogen atoms while the π_L are partially delocalized on the aromatic rings of the ligands [190, 191]. Additionally, most of the Ru-based complexes of the form $[\mathrm{Ru(L)_3}]^{2+}$, with L = bipyridine, exhibit a D_3 symmetry. Thus, in an idealized octahedral Ru(II)-polypyridine complex the orbitals associated to the ligands, i.e. σ_L and π_L, are completely occupied. After complexation the original d electrons of the metal anion will be splitted into two groups with an unneglectable energy difference between them, as depicted in Figure 3.1 panel A. One set contains those electrons whose orbitals are distributed in between the ligands, $t_{2g} = d_{xy}, d_{xz}, d_{yz}$. The second set would contain the electrons whose molecular orbitals "point" directly to the ligands, $e_g = d_{x^2-z^2}, d_{z^2}$ [191]. The orbitals contained in each set are degenerate, hence their respective energies are the same [192]. The magnitude of the difference between the energies of the orbitals e_g and t_{2g} is given by the octahedral ligand-field parameter Δ, and is determined by the ligand´s field strength, the atomic number of the metal ion and its oxidation state, allowing *chemical tunability* of metal complexes containing the same metal center [193]. In the new electronic configuration, produced by the interaction with the ligands, the d electrons will tend to first fill all the t_{2g} orbitals before occupying higher energy orbitals if the ligand field splitting is large. This trend is observed because populating the e_g orbitals would imply an energy investment equal to Δ which results to be energetically more demanding than pairing the electrons in the t_{2g} orbitals [191]. Such arrangement is named low-spin configuration and is depicted in Figure 3.1 Panel A [190–193]. When the energy necessary to pair two electrons in the same orbital is higher than Δ, the electrons tend to be far apart due to spin correlation, allowing electrons to populate high energy orbitals e_g, resulting in a configuration that is termed as "high-spin" [191].

Thus, the pairing of the outermost electrons of the octahedral metal complex formed by a d^6 metal center immersed in a strong field from the ligands results in a ground state with a closed shell, i.e. the ground state of the metal complex possesses a singlet nature [191], see Figure 3.1 Panel A. From successive one electron promotions, alongside the Born-Oppenheimer approximation, a qualitative description of the excited states of $[\mathrm{Ru(L)_3}]^{2+}$, an octahedral metal complex, can be obtained. Each excited state is described by means of its dominant molecular orbital configuration and classified according to the location of the

molecular orbitals involved in the transition between states [193], see Figure 3.1 Panel B. In this way an electron of the complex $[Ru(L)_3]^{2+}$ might undergo four types of electronic transitions after the absorption of a photon by the molecular system. It should be noted - according to the generally accepted picture - the photoinduced reactions on excited metal complexes, e.g. energy transfer or emission, occurring with appreciable quantum yields originate particularly from the lowest excited (triplet) states; in other words, metal complexes obey Kasha's rule [194]. The possible electronic transitions that an electron could experience on an excited metal complex are summarized on Figure 3.1 Panel B and enlisted below [190, 191]:

1. **Metal-centered (MC) or dd transitions** these transitions derive from the promotion of a t_{2g} electron to an e_g orbital. The origin of the name of this type of transition relies on the fact that the molecular orbitals involved on the transition remain on the metal. Since this type of transitions are (Laporte-) forbidden in octahedral complexes [16, 172, 195], the absorption of light associated to these transitions is usually weak [195]. Usually the geometry of the MC excited species is considerably displaced with respect to that of the ground state [196]. If the lowest excited state corresponds to a MC state, the relaxation of the molecule to the ground state might be driven by a quasi instantaneous and radiationless deactivation or the molecule could experience ligand dissociation, which depending on the circumstances might be a desired or undesired effect [162].

2. **Ligand-center transitions (LC) or $\pi\pi^*$ transitions** these transitions result from the promotion of an electron which is originally occupying a π orbital localized in the ligand system to a π^* orbital also localized in the ligands [193].

3. **Charge transfer transitions** as the name suggests, this type of transitions involve the transfer of an electron from one region of the molecule to another. When the origin of the transition is associated with the transfer of the excited electron from an orbital localized in the metal (t_{2g}) to an empty orbital in the ligand ensemble (π^*) is termed **metal to ligand charge transfer (MLCT) or $d\pi^*$ transition.** [190]. Transitions involving charge transfer from an orbital (π) located in the ligand ensemble to an orbital located in the metal (e_g) are called **ligand to metal charge transfer (LMCT) or πd transitions** [190–193]. Charge transfer transitions might induce redox reactions involving the metal complex and molecules surrounding it. When the metal center is reduced and a bond is cleaved radicals might be produced. Such free reactive radicals are known to induce cellular damage [8, 17, 168, 197]. LMCT and MLCT excited states do not show a strong modification of their equilibrium nuclear configuration

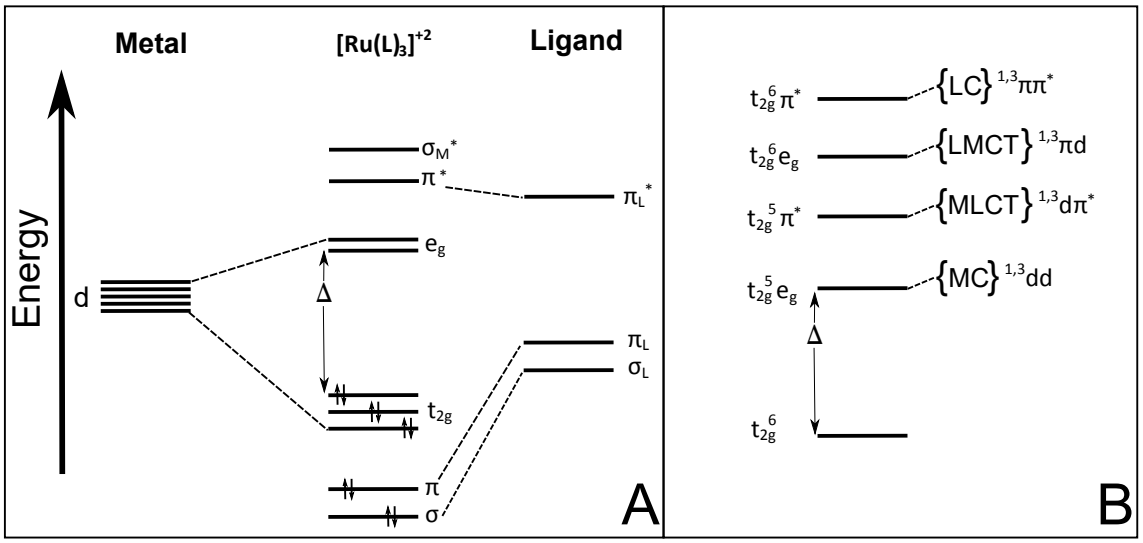

Fig. 3.1 A) Scheme of the molecular orbitals of an idealized octahedral $[\mathrm{Ru(L)_3}]^{+2}$. *B) States resulting from a* d^6 *system surrounded by polypyridine ligands symmetrically located on the corners of an octahedron whose center is the metal cation. The low-spin configuration results from the fact that a strong ligand field has been assumed [193].*

relative to that of the ground state. Thus, when the nature of the lowest excited state is either a LMCT or MLCT the relaxation is often accompanied by emission [191]. Furthermore, promotion of electrons from metal centered orbitals to the orbitals of solvent molecules might occur, however the quantum yields for such transitions are rather low [190]. If the metal complex contains more than one metal center, metal to metal charge transfer becomes feasible. The last two cases of charge transfer transitions are not shown in Figure 3.1. [192, 193, 198]

All the transitions enlisted above and depicted in Figure 3.1 Panel B might have a different spin multiplicity compared to that of the ground state as the promoted electron could either keep or inverse its spin orientation [193]. The multiplicity of the states is taken into account by the addition of corresponding labels in Figure 3.1 Panel B. Recall from Kasha's rule [193, 194] that only the lowest excited state plays a role on the dominant molecular physics observed. In line with this idea any transition involving a change of multiplicity demands[199], i.e. intersystem crossing (ISC), process which in principle is forbidden by the spin-conservation rule [195]. ISC can occur either by spin-orbit coupling of the singlet excited state S_1 to the higher vibrational level of the triplet state T_1 or by spin-orbit coupling between S_1 and a high energy triplet state T_n with a subsequent quasi-instantaneous decay to T_1, i.e. internal conversion between T_n and T_1 [195, 198]. In any case, the resulting triplet state is formed at rates within $10^9 s^{-1} - 10^{12} s^{-1}$ [200, 201]. Those triplet states populated after a transition, Figure 3.1 Panel B, consist of a cluster of different triplet states whose

populations follow a Boltzmann distribution [202]. Each sub-state of the cluster possesses a unique relaxation path and rate associated to it. The energy ordering of these states result from splitting of their energy by spin-orbit coupling [193].

In the study of Ru(II)-polypyridyl metal complexes the transitions, both radiative an non-radiative, involving singlet-triplet changes on multiplicity are of particular interest. Such transitions are forbidden by the spin selection rule [203]. Spin-orbit coupling is the cause that transitions between states with different spin multiplicities become permissible [195, 198, 203]. Its origin is briefly discussed. Due to the fact that an electron is a spinning charged particle and since the probability to find such electron on the vicinity of an atom is described by a wavefunction or molecular orbital, statement that can be simplified by saying that the electron is orbiting an atom, the electron undergoes two types of angular momentum: the spin $\vec{s}$ and orbital angular momentum $\vec{l}$ [203]. The interaction, i.e. the spin-orbit coupling, between $\vec{s}$ and $\vec{l}$ induces a mixing of pure singlet (ψ_1°) and triplet (ψ_3°) states whose Hamiltonian is given by

$$H_{so} = \xi \vec{s} \cdot \vec{l} \tag{3.1}$$

Where ξ is a function of the position and is proportional to the derivative of the electric field of the atom respectively of the position [203]. The wavefunction describing the state resulting from a spin-orbit coupling interaction is given by

$$\psi_{so} = \psi_3^\circ + \alpha \psi_1^\circ \tag{3.2}$$

On Equation 3.2 the superscripts $\circ$ denote "pure" singlet/triplet states and α is the degree of mixing and is

$$\alpha = \frac{\langle \psi_1^\circ | H_{so} | \psi_3^\circ \rangle}{|E_1 - E_3|} \tag{3.3}$$

Where E_1 and E_3 represent the energies of the singlet and triplet states respectively. Thus, the probability amplitude for any transition from a ground singlet state $|\psi_1\rangle$ to a mixed state, along side spin-orbit coupling, can be expressed as:

$$M = \langle \psi_3^\circ | \vec{\mu} | \psi_1 \rangle + \alpha \langle \psi_1^\circ | \vec{\mu} | \psi_1 \rangle \tag{3.4}$$

The first term on Equation 3.4 vanishes for the spin selection rule [195], however the second term contains a singlet-triplet contribution. Note also that due to the fact that H_{so} is proportional to the derivative of the electric field of the nucleus, see above, spin-orbit

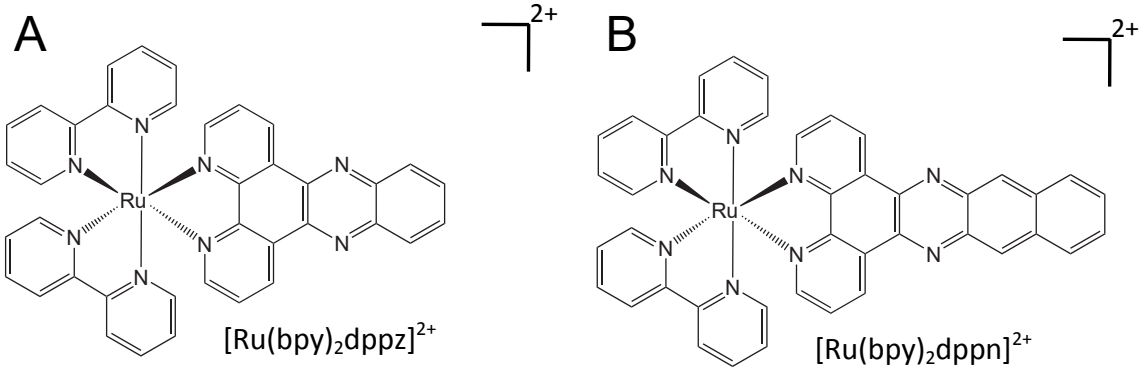

Fig. 3.2 A) The paradigm molecular light switch $[\mathrm{Ru(bpy)_2dppz}]^{2+}$*, a molecule that binds to DNA strands and possesses the light-switch mechanism. Due to its low cytotoxicity it can be used as cellular marker [159]. B)* $[\mathrm{Ru(bpy)_2dppn}]^{2+}$*, a compound that has shown cytotoxicity against cancer cell lines at low concentrations. It has comparable effects to cisplatin [174].*

coupling manifestations increase with an increment of the electronic number of the atom involved, the so-called *heavy atom effect* [198, 199, 203].

As mentioned above, the excited-state properties of a Ru-coordination complex depend on the nature and location of the molecular orbital of its lowest excited state. Since the energy ordering of the possible states (LMCT, MLCT, LC and MC) depend on factors[3] that can be chosen and synthetically modified, the nature and inherent properties of the lowest excited state can be chemically tuned. Figure 3.2 exemplary shows two molecules with a subtle difference: an aromatic ring in the ancillary ligand. This "minimal" modification of the ligand ensemble makes the molecule shown in Panel A a non-cytotoxic DNA marker while such modification makes the molecule shown in Panel B a potent anticancer drug [174]. Thus, "minimal" modification to the ligand ensemble of a molecule affects its behavior, or in the case of the molecules shown in Figure 3.2 the reactivity in cellular environments.

[3]The ligands, the location of the metal cation in the periodic table and its oxidation state, but mainly the ligands field strength when the metal center remains unchanged.

3.3 The paradigm molecular light switch: $[Ru(bpy)_2(dppz)]^{2+}$

At the beginning of the 90's a paper reporting $[Ru(bpy)_2(dppz)]^{2+}$, see Figure 3.2 Panel A, as a "true molecular light switch" for DNA was published [167]. The authors highlighted the fact that, at room temperature, the luminescence of $[Ru(bpy)_2(dppz)]^{2+}$ was effectively quenched in aqueous environments, yet emitting strongly in the presence of (double helical) DNA. They also determined, by absorption titration and equilibrium dialysis experiments, that the complex binds avidly to DNA showing a very high ($> 10^6 M^{-1}$) binding constant. The binding of $[Ru(bpy)_2(dppz)]^{2+}$ to DNA has been attributed to intercalation between the planar dppz and the nucleotides of DNA, followed by π stacking between such molecules [167, 168, 173]. Several groups have reported drastic emission enhancement ($> 10^4$) upon intercalation of $[Ru(bpy)_2(dppz)]^{2+}$ to DNA in aqueous solutions and that the photophysics of $[Ru(bpy)_2(dppz)]^{2+}$ is very sensitive to environmental conditions [167, 169, 170, 197, 200, 204]. Despite the fact that its absorption spectrum remains almost unmodified after dissolution in aqueous and non-aqueous solvents, at room temperature, the molecule shows evident solvatochromatic emission (around a generic peak at 610 nm), luminescence intensity and lifetime differences in media with different dielectric constants (or polarities), viscosity or hydrophilicity [167, 169, 170, 197, 200, 204]. Nair et. al [204] found that, at room temperature, the polarity of the solvent is the main parameter to determine the luminescence lifetime and intensity in non-aqueous environments by noting that such parameter correlates linearly with the photophysical properties: as the polarity of the solvent increased a reduction of both the emission lifetime and intensity was observed. Interestingly, this is not the case for hydrogen bonding solvents. The emission dependence on polarity of $[Ru(bpy)_2(dppz)]^{2+}$ turns attractive and powerful for *in cellulo* experiments where the cytosol[4] is a very polar environment while the DNA[5] and inner regions of membranes posses small dielectric constants resulting in small polarities [205, 206]. Thus, a clear and compartmental delimitation of cells can be obtained since the light switch will be activated in regions with low polarity and would remain off in polar environments, this is exemplary shown in Figure 3.3.

The influence of the inherent chirality of $[Ru(bpy)_2(dppz)]^{2+}$ on binding to DNA has been investigated. Hiort et. al [207] separated the Δ and the Λ enantiomers from a racemic mixture of $[Ru(bpy)_2(dppz)]^{2+}$ and determined that the (relative) emission quantum yield of the intercalated Δ enantiomer in DNA solution is roughly eight times higher compared to the emission arising from the Λ enantiomer. The emission discrepancy between the

[4] $\varepsilon_{cytosol} = 91.5$
[5] $\varepsilon_{DNA} = 16.0$

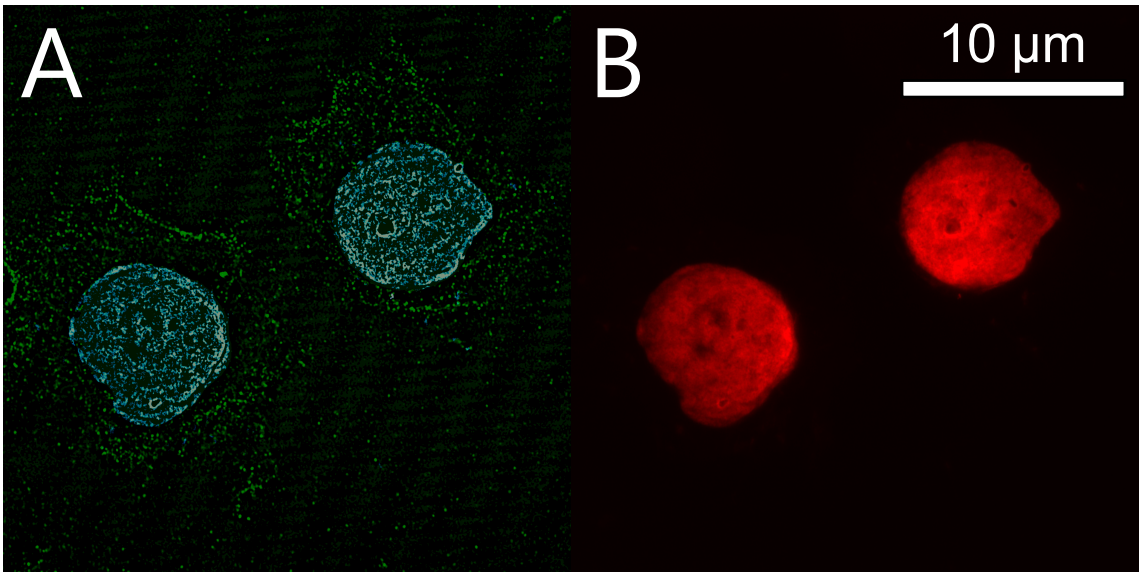

Fig. 3.3 HepG2 (liver hepatocellular carcinoma) doped with A) $[Ru(bpy)_2(dppz)]^{2+}$ *and B) co-stained with standard nuclear and cytosol markers, i.e. DAPI (4', 6-diamidino-2-phenylindole) and Alexa (Alexa Fluor 488 Phalloidin) respectively.*

enantiomers was attributed to differences on intercalation geometries of the dppz ligand of the enantiomers, meaning that for the Δ enantiomer the intercalation, and isolation from water, is more efficient compared to that of the Λ enantiomer. Enantioselective experiments of $[Ru(bpy)_2(dppz)]^{2+}$ *in cellulo* have also been performed [179] and again the dominant enantiomer, in terms of emission intensity, is the Δ enantiomer. Thus, the results are in line with the solution experiments.

Therefore, the environmental sensitivity of $[Ru(bpy)_2(dppz)]^{2+}$ as a spectroscopic probe for cellular scenarios are extensively documented including reports with experiments carried out in DNA solutions, cellular membrane models, lysate and even *in cellulo* [152, 167, 169, 170, 197, 200, 204, 179, 208].

3.3.1 The light-switch mechanism

Upon optical excitation of $[Ru(bpy)_2(dppz)]^{2+}$ by electromagnetic radiation around 450 nm, see Figure 3.4, a *d* electron from the Ru core is transferred to a π^* orbital in the dppz ligand forming a ^{1}MLCT state. Due to the heavy atom effect, see above, ISC occurs with a quantum yield of practically unity. Thus, the resulting (manifold of) ^{3}MLCT is formed in less than 300 fs [201]. The photoinduced species can be expressed as:

$$[Ru^{II}(bpy)_2(dppz)]^{2+} \xrightarrow{h\nu} [Ru^{III}(bpy)_2(dppz^{\bullet -})]^{2+} \tag{3.5}$$

where the promoted electron is located on the dppz ligand. The latter has two low-lying unoccupied molecular orbitals [209] distributed over the ligand: one orbital lies on the phenatroline moiety and the other one on the phenazine. The last statement is supported by molecular orbital calculations [210], electrochemical measurements [172, 211] and femtosecond time resolved experiments [200, 208]. The resulting excited states associated with these orbitals will be termed $^3MLCT_{bright}$ and $^3MLCT_{dark}$ for the states involving the phenatroline and phenazine moieties respectively. Through pump-probe spectroscopy experiments has been determined that the interconversion between $^3MLCT_{bright}$ and $^3MLCT_{dark}$ states is achieved within 20 ps [200, 208].

The emission of $[Ru(bpy)_2(dppz)]^{2+}$, see Figure 3.4, results from a radiative transition from the excited $^3MLCT_{bright}$ state to the ground state, even though the $^3MLCT_{bright}$ has a higher energy than the $^3MLCT_{dark}$ state. The emission lifetime τ varies from solvent to solvent [204], for example, in dichloromethane $\tau = 257$ ns while in formamide $\tau = 25$ ns. Interestingly, the deactivation of the non-emissive $^3MLCT_{dark}$ state in water at room temperature occurs with $\tau = 250$ ps [200, 208]. Such decay times are in agreement with the energy gap law [212], which predicts that the decay rates of a particular excited states would be $k \propto e^{(-\Delta E_{eg})}$, where ΔE_{eg} corresponds to the difference between excited and ground states.

Brennaman and colleagues [213] determined, by temperature-dependent emission lifetime-measurements in protic and aprotic solvents, that the so called light switch effect is the result of a competition between energetic and entropic factors favoring respectively the $^3MLCT_{dark}$ and the $^3MLCT_{bright}$ states. In other words: changes on the enthalpy of the system would set the equilibrium towards the non-emissive $^3MLCT_{dark}$ state while changes on the order or entropy of the system would stabilize the $^3MLCT_{bright}$ state inducing radiative deactivation, see Equation 3.7. They noted that at low temperatures the intensity and emission lifetimes were lower compared to those obtained at higher temperatures. However, after increasing the temperature above certain values they also noted a roll over of both spectroscopic parameters,

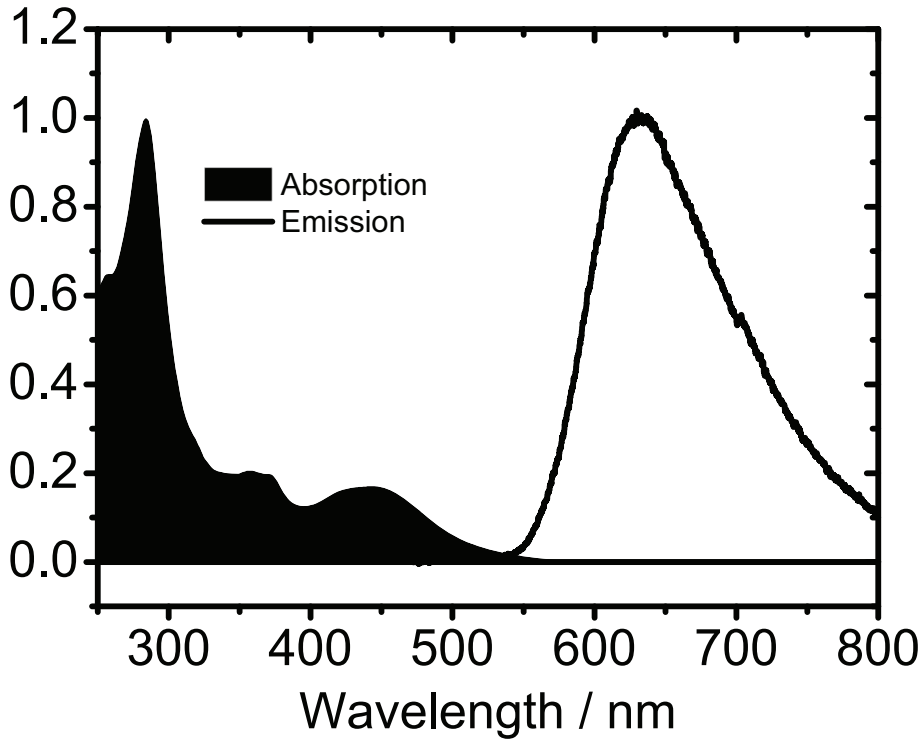

Fig. 3.4 Absorption and emission spectra of $[Ru(bpy)_2(dppz)]^{2+}$ *in acetonitrile (ACN) at room temperature. The emission is the result of a transition between a* ^{3}MLCT *state and the ground state. Since the latter has a singlet multiplicity the luminescence type exhibited by* $[Ru(bpy)_2(dppz)]^{2+}$ *is phosphorescence.*

phenomenon attributed to d-d transitions. From these results they proposed the energy diagram shown on Figure 3.5.

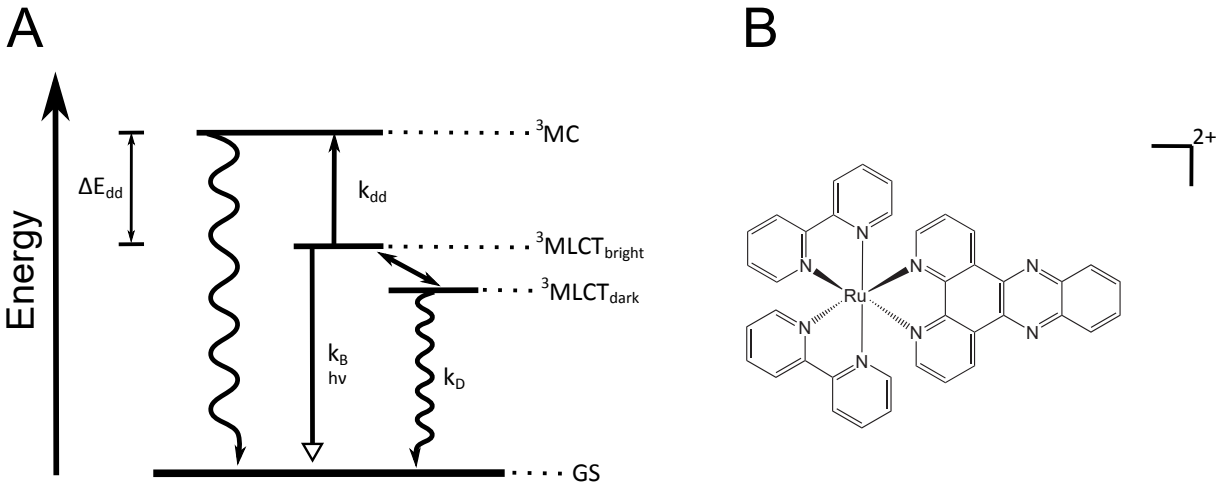

Fig. 3.5 A) The energy diagram of $[Ru(bpy)_2(dppz)]^{2+}$. *The emission results from relaxation of molecules in the* $^3MLCT_{bright}$ *state to the ground state (GS). However, if the* $^3MLCT_{dark}$ *is equilibrated, no emission is observed. When the molecular ensemble has gain enough energy, i.e. above 3000 - 3500* cm^{-1} *from the* ^3MLCT *manifold, a MC state is observed, exhibiting a quasi-instantaneous non-radiative decay [213, 214]. B) Molecular structure of the paradigm light switch* $[Ru(bpy)_2(dppz)]^{2+}$. *Both the* $^3MLCT_{bright}$ *and the* $^3MLCT_{dark}$ *states are associated to the dppz ligand of the complex. The bright state is localized in the phenatroline whereas the dark state lies in the phenazine.*

The ratio of the population on the $^3MLCT_{bright}$ state (ρ_B) to the population on the $^3MLCT_{dark}$ state (ρ_D), i.e. the light switch effect, can be computed with the Boltzmann factors:

$$\frac{\rho_D}{\rho_B} = \exp\left(-\frac{\Delta H - T\Delta S}{kT}\right) \tag{3.6}$$

where k is the Boltzmann constant, T is the temperature, ΔH and ΔS correspond respectively to changes on enthalpy and entropy while the reaction takes place, i.e. "the motion of charge from one portion of the dppz ligand to another" [213]. Brennaman and coworkers [213] determined, by using their experimental data, that ΔH and ΔS must be negative in order to get consistency between the data and the proposed model, an indicative that the reaction is an exothermic spontaneous process.

In aprotic environments the energy gap between $^3MLCT_{bright}$ and $^3MLCT_{dark}$ states is easily overcome by the energy supplied to the system by the environment at room temperature, in this way increasing the population of the $^3MLCT_{bright}$ state at the equilibrium. This is not the case on protic environments, where the energy gap is larger and the minimum

energy needed to set the equilibrium to the ^{3}MLCT$_{\text{bright}}$ state lies above room temperature, facilitating the occupation of the non-emissive ^{3}MLCT$_{\text{dark}}$ state.

The molecular light switch dependence on the polarity of the solvent can also be explained with the discussed model [214]. When an electric field is applied on randomly oriented polar molecules (which are essentially dipoles conforming a dielectric) a torque induced by the field is experienced by the molecules, causing them to (partially) be aligned with the incident electric field. Recall that the induced electric field on the dipoles would tend to oppose to the incident field. The ability of a dielectric to align its dipoles in response to the incident electric field is quantified by the dielectric constant (or polarity). Therefore, the higher the dielectric constant the more ordered the solvent molecules. In addition, the charge distribution of the ^{3}MLCT$_{\text{dark}}$ lies over the phenazine moiety of the dppz, thus the dipole moment of the ^{3}MLCT$_{\text{dark}}$ is higher compared to that of the ^{3}MLCT$_{\text{bright}}$ state. With this, the overall disorder of the molecular ensamble would tend to zero, i.e. $\Delta S \rightarrow 0$, situation that preferentially stabilizes the equilibrium towards the ^{3}MLCT$_{\text{dark}}$ state.

3.4 Biophysics and ion uptake by cells

3.4.1 The cellular membrane

The cellular membrane is the structure that delimitates the borders of a cell. It keeps the cell isolated from the surrounding environment and it is a key element for the maintenance of the internal composition of the cell [215–217]. It must regulate the uptake of necessary molecules, such as ions (e.g. Na^+ or K^+), glucose, amino acids, lipids, etc, and excrete metabolic waste; therefore, it must be selectively permeable to small molecules. In this way the cellular membrane serves as a barrier for the exchange of molecules contained in the cytosol and those in the exterior of the cell. Most cellular membranes are composed by amphiphilic phospholipid bilayers which are kept together by hydrophobic interactions, with a thickness ranging between 6 and 9 nm [216]. The phospholipids posses a hydrophilic polar head group and two hydrophobic non-polar hydrocarbon tails, see Figure 3.6. The hydrophobic parts avoid water and tend to clump together while the polar parts face the aqueous solutions. Thus, the phospholipid bilayer is the structure that builds up the impermeable barrier of the cellular membrane.

The uptake mechanisms of ions through cellular membranes depicted on Figure 3.6 can be summarized in the following way [216, 217]:

1. **Passive diffusion** is the motion of ions from an outer region of the cell with a high ion concentration to another region inside the cell with a low ion concentration. In this type

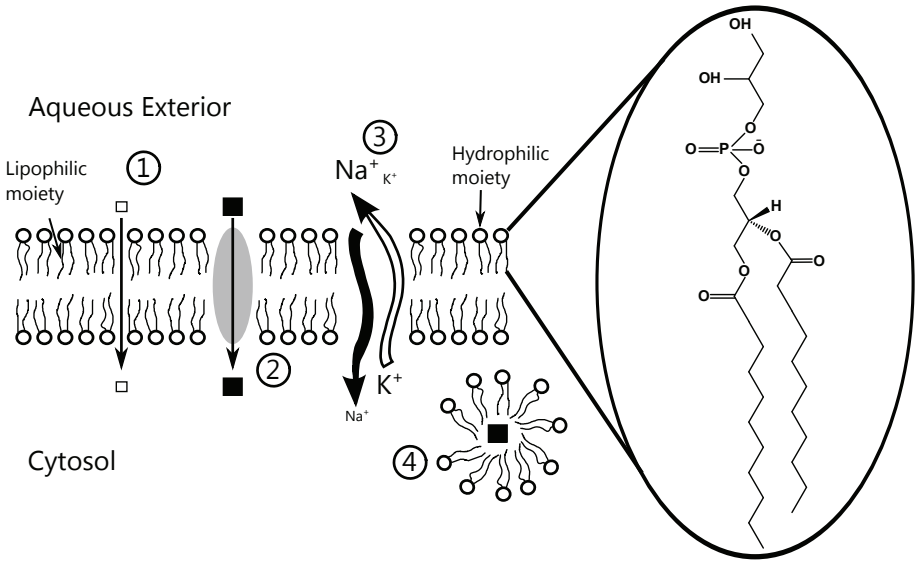

Fig. 3.6 Scheme of the cellular membrane structure and representation of the uptake mechanisms of a cell: 1) Passive diffusion, 2) facilitated diffusion, 3) active transport and 4) endocytosis. This molecular membrane is build up by DPPG phospholipids (1,2-Dipalmitoyl-sn-glycero-3-phosphocholine).

of uptake mechanism diffusion and electric fields (at the cellular membrane interface) play an important roll. The rate of passive diffusion depends on the permeability of the cellular membrane. This uptake mechanism does not demand metabolic energy.

2. **Facilitated diffusion** the uptake mechanism employed by a cell to transport water, ions and small hydrophilic molecules via channel proteins. These type of proteins form a hydrophilic path across the membrane facilitating the diffusion of essential molecules, for which the cellular membrane remains impermeable.

3. **Active transport** this type of uptake mechanism is utilized by the cell to carry out the transport of ions against a chemical concentration gradient and/or an electric potential. In this uptake mechanism, the cell utilizes the energy released during the hydrolysis of ATP to "pump" ions or other solutes across the membrane. As ATP is employed, active transport requires cellular energy.

4. **Endocytosis** an uptake mechanism used by the cell to internalize essential big polar molecules, incapable to propagate through the impermeable cellular membrane. During endocytosis the cell uses its cellular membrane to invaginate such molecules forming pockets and depositing their content in its interior. This uptake mechanism demands metabolic energy from the cell.

The potential energy W that needs to be overcome by a positively charged particle p as a $[\mathrm{Ru(bpy)_2(dppz)}]^{2+}$ molecule in order to diffuse through the cellular membrane and get into

the cell is the result of the sum of two contributions [218, 219]: W_e and W_n. W_e arises from electrostatic interactions between the charged molecule p and the cellular membrane, see Figure 3.7. Since the lipophilic interior of the cellular membrane has a much more lower dielectric constant than that of the hydrophilic part at the interface with aqueous environments, W_e peaks at the core of the membrane[6]. W_n accounts for all the other interactions of an utopical electrically neutral molecule p, i.e. W_n results from lipophilic interactions between the molecule p and the cellular membrane. During the diffusion of the p ion across the membrane its solvation state changes. If p is hydrophobic W_n has a negative contribution, since the energy of the dissolved system or state is less (enthalpy and entropy are reduced). On the other hand, if the molecule is hydrophilic W_n has a positive contribution. From this discussion, is evident that lipophilic cations would accumulate easier inside the cells than non-lipophilic cations [220, 221].

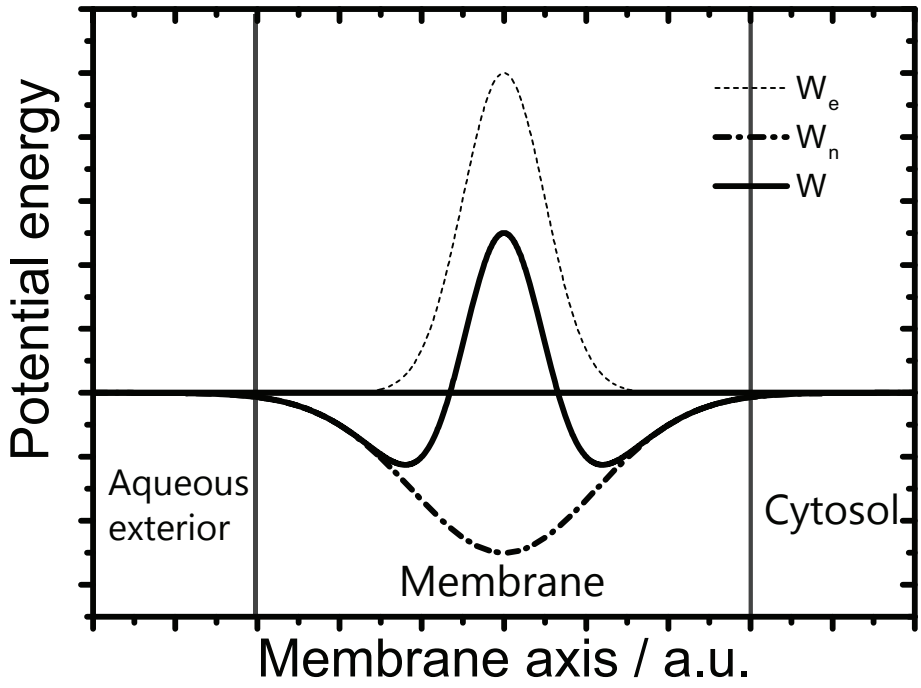

Fig. 3.7 An arbitrary potential energy barrier W to ion transport across a cellular membrane.

Specific transport of electrolyte ions across the membrane generates a difference in the concentration of such ions between the two bulk aqueous phases divided by the cell membrane, i.e. the cytosol and the exterior of the cell [215–217]. This concentration difference of charged particles induces an electric potential across the cellular membrane, being the interior site of the cell more negative respective to the exterior of the cell. The last

[6]Recall that the energy density of an electric field is $U = \frac{1}{2}\varepsilon E^2$ and the electric field itself is given by $E = \frac{q}{4\pi\varepsilon R^2}$.

results from the fact that this electric potential difference favors the uptake of (lipophilic) cations but opposes the uptake of anions [222]. Since the interior of the cellular membrane is formed by dielectric lipoic molecules, it can be modeled as an electric capacitor. Indeed, an estimation of the equilibration of lipophilic cations inside the cell can be obtained with the Nernst equation [220, 223, 224], an expression derived from thermodynamics:

$$V_{in} - V_{out} = \frac{kT}{zq} \ln\left(\frac{C_{in}}{C_{out}}\right) \tag{3.7}$$

Here k is the Boltzmann constant, T the temperature, z the valence of the ion (including sign), q is the electric unit charge, V_{in} (C_{in}) and V_{out} (C_{out}) are the potential (concentration) inside and outside the cell respectively. From Equation 3.7 can be seen that "the more negative the potential the greater the accumulation of positively charged dye"[220].

3.4.2 Cellular uptake of Ruthenium(II) polypyridyl complexes

Barton´s group studied the cellular uptake of a series of Ru(II)-dppz molecules, among them the paradigm molecular light switch $[Ru(bpy)_2(dppz)]^{2+}$, by flow cytometry and CLSM [181]. The dppz ligand was present in all the investigated molecules while the ancillary ligands were varied in order to change the size and lipophilicity of the molecules. They concluded, based on emission images, that the Ru(II)-dppz complexes are indeed internalized into live **HeLa** cells and *accumulated in the cytoplasm*, (likely) linked to mitochondria and endoplasmic reticulum. By means of flow cytometry measurements they estimated the amounts of absorbed dye and, as expected from the discussion above, was determined that the fastest molecule to diffuse into cells was the most lipophilic, i.e.: $[Ru(DIP)_2(dppz)]^{2+}$, even though it was also the biggest molecule (with a length of 20 Å). They also reported that neutral molecules are poorly uptake by cells, which is in accordance with Equation 3.7.

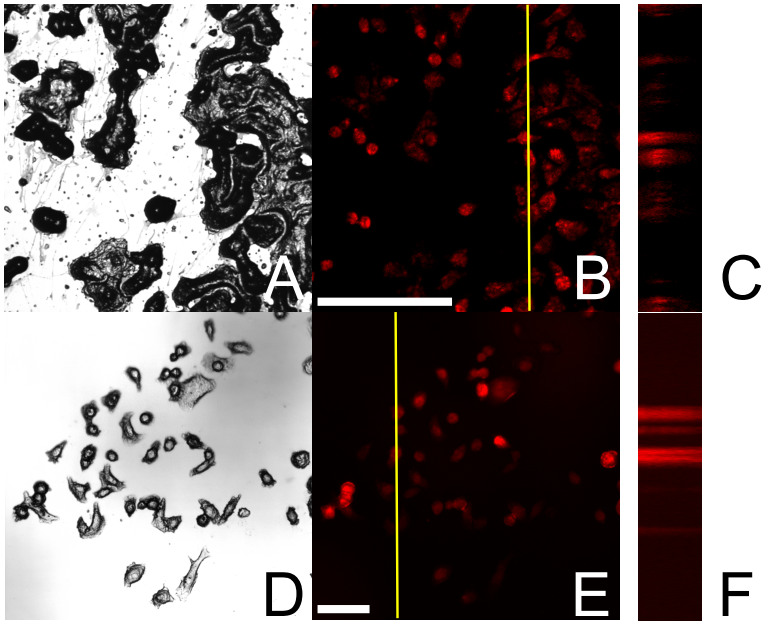

Fig. 3.8 Comparison of the cellular uptake of $[Ru(bpy)_2(dppz)]^{2+}$ *in absence A-B) and presence D-E) of PCP where HepG2 cells were employed as in vitro model. The cells were incubated with* $[Ru(bpy)_2(dppz)]^{2+}$ *for 24 hours. The images were obtained through CLSM, exciting at 450 nm and detecting in the spectral range between 650 and 700 nm. The scale bars correspond to 50 µm. The yellow bars denote the regions probed to generated the y-z images shown in panels C and F.*

The Barton´s group continued studying the cellular uptake of Ruthenium polypyridine complexes [225]. They suggested that the uptake of cationic Ruthenium polypyridine complexes is carried out by passive diffusion, i.e. a metabolic energy free process, see Figure 3.6. These conclusions were given after noticing that the uptake of $[Ru(bpy)_2(DIP)]^{2+}$ by

cells previously treated with deoxyglucose[7] and oligomicyn[8] was similar to the uptake of cells incubated under normal conditions. In addition, they also incubated cells alongside $[Ru(bpy)_2(DIP)]^{2+}$ at different temperatures, i.e. 4.0 ° C, 21.5 °C and 37.0 °C, and observed that the uptake was not sensitive to temperature. They also claimed that the cellular uptake hinges on the membrane potential since cells whose cellular membrane was hyperpolarized adsorbed by a factor of 2.8 more dye compared to those cells whose cellular membranes remained unaltered or depolarized.

Several research groups [181, 179, 160, 226, 184] have mentioned that the cellular uptake of Ruthenium polypyridine cations by living cells is poor when the cellular membrane is intact. Particularly for $[Ru(bpy)_2(dppz)]^{2+}$ it has been claimed that it can not reach the nucleus unless the cells are dead and facilitated by the artifacts induced by fixation. Recently it was reported that the cellular and nuclear uptake of Ru(II)-polypyridyl cationic complexes, and particularly that of $[Ru(bpy)_2(dppz)]^{2+}$, is enhanced (in terms of diffusion rates and nuclear localization) by incubating the cells in a media containing Ru(II)-polypyridyl cations alongside an organochlorine compound: PCP (pentachlorophenol) [179]. The authors reported that the cells were not killed by the solution and suggested that the improved permeability of the paradigm molecular light switch to diffuse through the cellular membrane is the result of an increment on the lipophilicity of the complex by the formation of an ion-pair between $[Ru(bpy)_2(dppz)]^{2+}$ and PCP molecules. To asses this hypothesis and its reproducibility we incubated HepG2 cells with $[Ru(bpy)_2(dppz)]^{2+}$ and PCP in a ratio of 1:3 (1 Ru-complex to 3 PCP). From Figure 3.8 it can be seen that indeed the incubation of eukaryotic cells with $[Ru(bpy)_2(dppz)]^{2+}$ and PCP increases the cellular uptake based on the higher intensity of the recorded emission images of Panels D-E compared to that of Panels B-C, the predominant nuclear localization of the dye as well as a higher penetration depth observed in Panels D-E. However, it should be mentioned that all the research oriented to cellular applications of Ruthenium polypyridine cations has been performed under two common standard conditions for organic lipophilic molecules: low dye concentrations ($<$ 50 μM) and/or low incubation times ($<$ 4 hours). Figure 3.9 shows exemplary HepG2 cells incubated with 50 μM of $[Ru(bpy)_2(dppz)]^{2+}$ for 24 hours co-stained with resazurin (Alamar blue)[9] [227]. As can bee seen on Figure 3.9 panel a the cells were alive while on the same figure but on panel b intense luminescence is observed on nuclear compartments, on both the x-y and x-z planes. The luminescence derives from relaxation of excited $[Ru(bpy)_2(dppz)]^{2+}$ molecules to the ground state.

[7] A glycolysis (the breaking down of glucose) inhibitor that prevents ATP production.

[8] An inhibitor of synthesis of ATP .

[9] An oxidized blue dye which changes its color to pink upon reduction by metabolic activity of cells.

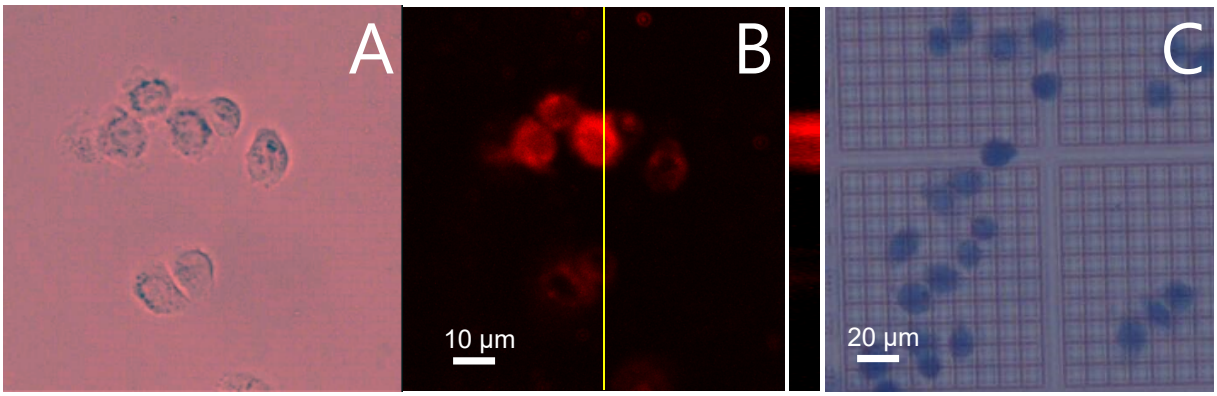

Fig. 3.9 HepG2 cells incbutaed with $[Ru(bpy)_2(dppz)]^{2+}$ *and resazurin. a) Bright field image of doped cells and b) its corresponding emission image. The lack of evident blue pigment on panel a) suggests that the cells were alive during the experiments. Panel c) exemplary shows dead cells doped with* $[Ru(bpy)_2(dppz)]^{2+}$ *and co-stained with resazurin.*

Since the time dependence of the cellular uptake of Ruthenium polypyridine cations has not been reported, HepG2 cells were incubated with 50 μM of $[Ru(bpy)_2(dppz)]^{2+}$, fixed and imaged at different times. The results obtained with this study provide a qualitative[10] description of the localization of the paradigm molecular light switch on the cell as function of time, see Figures 3.10 and 3.11. As expected from reports of other research groups [225, 181, 179] the uptake was poor when the incubation time was below 4 hours, see Figure 3.11 panels a and b. The emission intensity is slightly stronger after 6 hours of incubation, see Figure 3.11 panel c, however the emission intensity scales almost a factor of three when the cells have been in contact with the dye for 24 hours with an evident accumulation of the drug into the nuclei, Figure 3.11 panel d. The results presented on Figures 3.9, 3.10 and 3.11 suggest that Ruthenium polypyridine cations are actually uptaked by living cells with a constant diffusion over time and, as suggested by Barton and colleagues, driven by the membrane potential.

[10]Flow cytometry experiments might provide truly quantitative description of the diffusion rate of the cations into the cells.

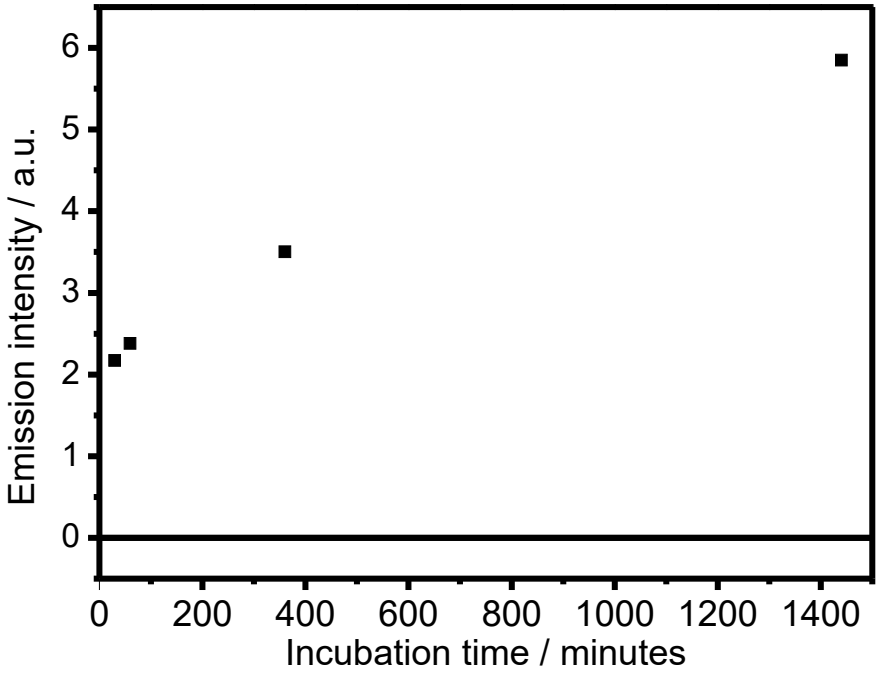

Fig. 3.10 Maximum emission values recorded from HepG2 cells incubated with $[Ru(bpy)_2(dppz)]^{2+}$ *as function of time.*

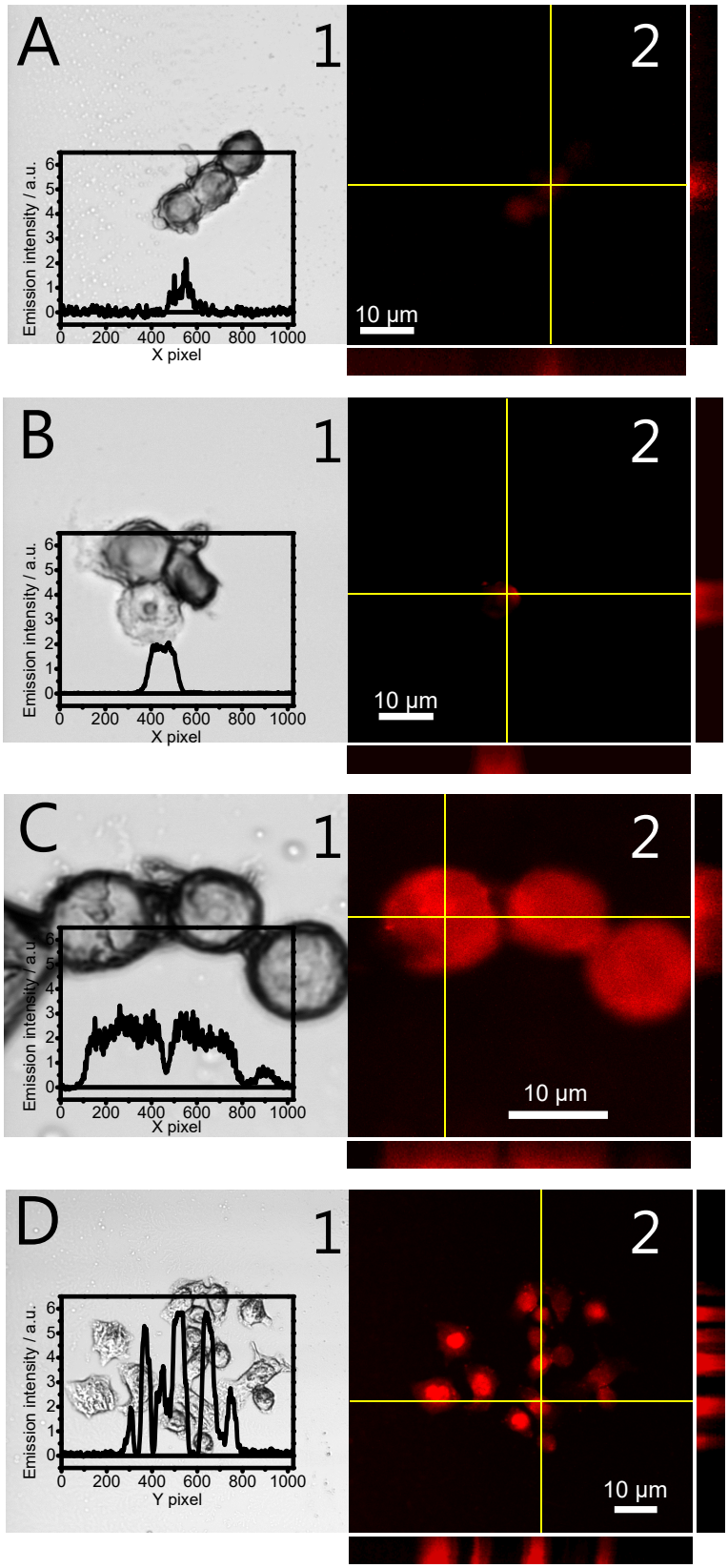

Fig. 3.11 Incubation time dependence of the cellular uptake of $[\mathrm{Ru(bpy)_2(dppz)}]^{2+}$ *by HepG2 cells. Panel A, B, C and D show cells incubated for 30, 60, 360 and 1440 minutes respectively. The sub-panels labeled as 1 show the phase image while sub-panels 2 show the corresponding emission image (long-pass filter at* $\lambda > 650$ *nm). The insets depict the emission intensity as function of the pixel coordinate of the corresponding sub-panel 2.*

Chapter 4

Experimental set-ups

4.1 The light source of the TAM

Once discussed the physics of the processes involved in the amplification of light and creation of certain spectral components, see Sections 2.4 and 2.5, a description of the implementation of such processes to set-up a device which provides the pump and probe beams required to perform pump-probe microspectroscopy can be given. Before that, it is important to mention that two dual-OPA were employed during this research. One of them entirely commercial and based on optical fibers and a second one designed, constructed and characterized "in house" based on bulk materials, namely, second order non-linear crystals.

The reason behind the construction of the second dual-OPA was the necessity to improve the signal to noise ratio (S/N) obtained with the commercial system. The S/N can substantially be affected by artifacts produced by the unavoidable mechanical vibrations and transient changes of the polarization of the beams, however, the most important "source" of noise during pump-probe microspectroscopic experiments performed during this research was *definitely* the pulse to pulse fluctuations (PPF) of the beams. The PPF (50% for the commercial dual-OPA), which affects directly the S/N during an experiment, should not be above 5% for conventional pump-probe spectroscopy, i.e. in solutions, where imaging optics as telescopes, objectives, and other optical elements of a microscope are not present to affect the reference and signal readings and therefore the ratios of such measurements, see Section 4.2. Therefore, considerable effort was invested in the improvement of the S/N due to the fact that such improvement is reflected in a reduction of the acquisition time per pixel/delay-time-position, since less experiments per point (either in space in imaging mode or time in spectroscopic mode) are required to obtain data with a short deviation from the mean experimental value.

The comparably high PPF of the commercial OPA lead to long experiments accompanied of obliteration of the samples. With the self made dual-OPA the fluctuations between pulses were reduced to 5% and the acquisition time, respective to the commercial dual-OPA, was also reduced by a factor of fifteen, however, this came at expenses of a comfortable, computerized and a considerably broad spectral tunability of the beams. Nevertheless, the results obtained with the *in house* dual-OPA were superior, thus, this is the only system that will be discussed, see Figure 4.1.

A key element of the TAM is of course the light source. For the system that will be described below, the light source consists of a diode-pumped laser, which provides two independent optical pulsed-beams. One beam has a repetition rate of 125 kHz whereas the second beam oscillates at 250 kHz, where such repetition rates are set by a couple of acousto-optical modulators. The gain medium of this laser is an Ytterbium-doped fiber, pumped by a fiber-coupled diode laser (DILAS, Coherent) with an emission peak at 976 nm. High output power and power conversion efficiency can be attained with Ytterbium-doped fibers [228, 229]. It is important to mention that the average power of the 250 kHz channel is 5 W while the same parameter for the 125 kHz channel is 3 W. The inherent geometry of the fiber leads to attractive thermo-optical properties, since the large surface to volume ratio and the distribution of heat over all the structure result in an excellent heat dissipation. Therefore, the beam properties, in principle, are not distorted over time. In order to perform the microspectroscopy experiments with the "pump-on" and "pump-off" condition the slow channel is used to produce the pump beam while the fast oscillating channel is employed as the probe, as can be deduced from the repetition rates. Hereafter, the 125 kHz and the 250 kHz channels will be simply termed as the pump channel and the probe channel respectively. The laser cavity has been constructed, by the company Active Fiber, in a way that it provides pulses in the fs regime with ca. 450 fs pulse duration centered at 1030 nm for both the pump and probe beams, see Figure 4.1.

The fundamental pump and probe beams, i.e. radiation with $\lambda = 1030$ nm, are guided to two almost identical OPAs. In each of these OPAs the fundamental beam is separated into two beams by a polarizing beam splitter (PBS). The separated beams will contain, respectively, 70 and 30 % of the incident fundamental beam, where the splitting ratio is tuned easily by a $\lambda/2$ wave plate. The weakest branches of the fundamental beams, i.e. those beams with 30 % of the energy of the fundamental pump and probe beams, are guided to a Sapphire (Al_2O_3) crystal in the case of the pump and to a YAG (Yttrium Aluminium Garnet, $Y_3Al_5O_{12}$) crystal in the case of the probe beam to generate white light super-continuum (WL).

WL, which is optical radiation containing a broader spectrum compared to the radiation originating it, can be achieved by self-phase modulation (SPM) [102]. SPM relies on an

intensity-dependence of the refractive index of a centrosymmetric dielectric material, as in this case the Sapphire and YAG crystals, in response to an applied field [65, 102, 86]. This phenomenon is a third order nonlinear process known as Kerr effect [65]. The induced intensity dependence of the refractive index of the medium is directly reflected in a time dependent phase shift or frequency deviation in the laser pulse. This would produce that the leading oscillations of the pulse shift to lower frequencies (or redder wavelengths) whereas the slowest components would be shifted to higher frequencies (or bluer wavelengths). The peak of the laser pulse would not be shifted, however the oscillations close to the peak would suffer a relatively linear spectral shift. Therefore, extra frequencies will be generated by SPM, without affecting the temporal profile of the pulse[1] since the SPM effects are only present in the phase of the incident field [102]. In Figure 4.1 panels B and C the WL spectra of the YAG and Sapphire crystals are shown.

Each of the independent WL of the pump and probe channels are focused onto corresponding Barium Borate (BaB_2O_4, BBO) plates, non-centrosymmetric crystals with high optical damage threshold [2]. The last is done to amplify particular components of the spectra or modes shown in Figure 4.1 panels B and C. For this reason the BBO plates used to amplify certain modes will be termed BBO_{OPA}. As discussed in Section 2.5, the amplification process requires the coupling of resonant modes through the modulation of the dielectric constant of a material by an intense (optical) source. In this set-up, such intense sources of the pump and probe OPAs are obtained by doubling the frequency of the branches of the fundamental beams containing the 70 % of the radiation using BBO plates, in other words: the intense source used to amplify a particular WL component is obtained with SHG of the fundamental beams, i.e. radiation centered at 515 nm. Once obtained the intense sources these are spatially overlapped with their corresponding WL into their respective BBO_{OPA}.

To tune the amplified wavelength a mechanical translational stage can be used to temporally overlap the desired spectral component with the 515 nm beam alongside an adjustment of the BBO_{OPA} to obtain the phase matching condition required. In the case of the probe, these amplified components are used to explore the excited state dynamics of the studied samples while in the case of the pump beam, a second doubling of the frequency of the amplified components is done in order to excite the blue-shifted bands of the Ruthenium-based complexes investigated during the work at hand.

In summary, the light source of this system makes possible the exploration of excited state dynamics of molecular assembles with diffraction limited spatial-resolution in the optical

[1] In practice, one should take into account the dispersion effects induced by the linear refractive index of the material, e.g. group velocity dispersion, because alongside the spectral broadening induced by SPM a temporal broadening can also be induced.

[2] 5×10^{10} (W/cm^2).

range within 550 - 680 nm and their corresponding idler frequencies (not shown in Figure 4.1). In addition, the fundamental beam at 1030 nm and its second harmonic can also be used as probe for the experiments. Similarly, the pump radiation can be centered in the optical range of 700 - 850 nm and the corresponding second harmonic 350 - 425 nm, and of course, at the fundamental wavelength 1030 nm and its second harmonic.

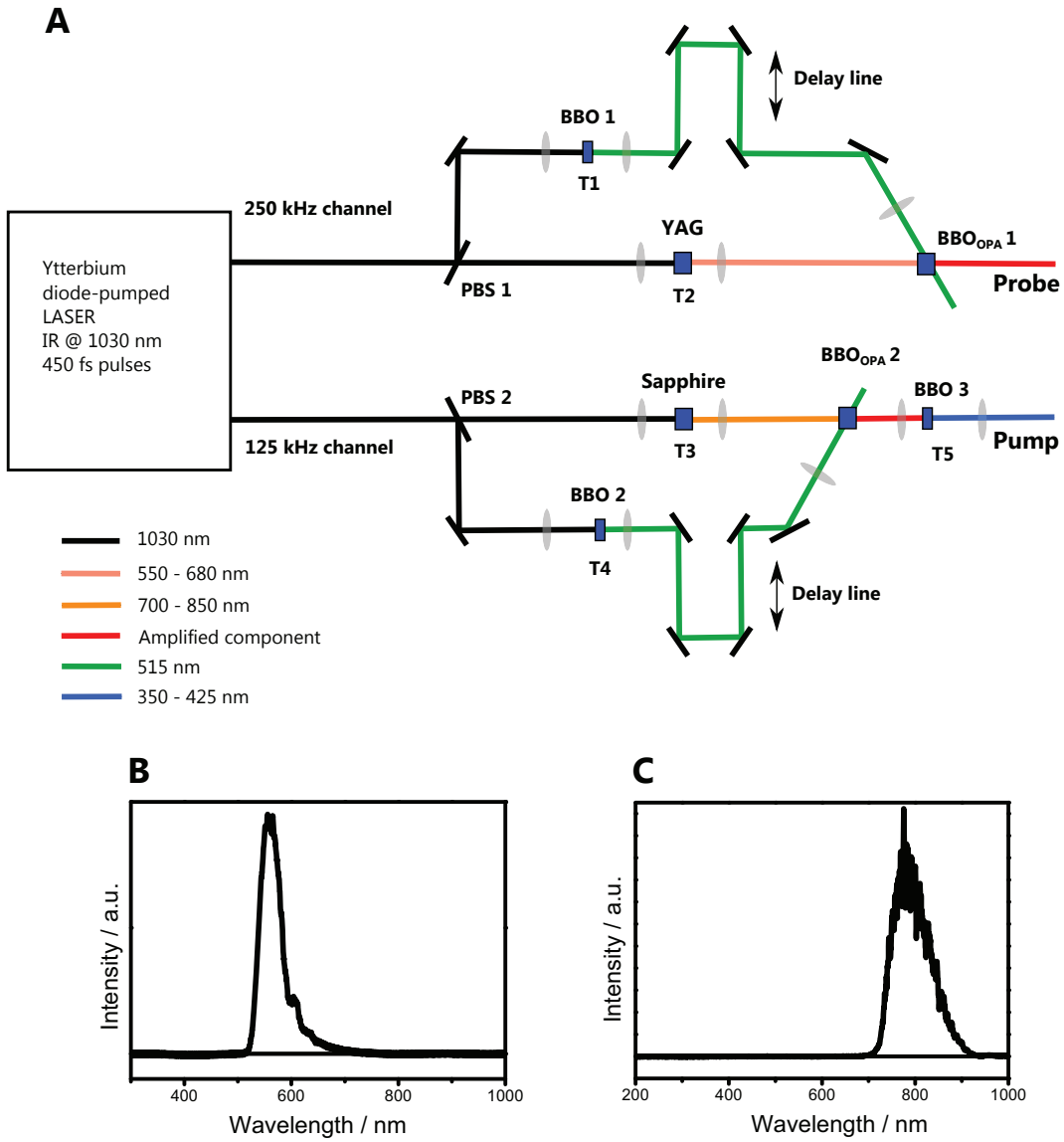

Fig. 4.1 A) Schematic representation of the light source of the TAM. PBS stands for polarizing beam splitter while T for Telescope. See text for a detailed description. B) and C) show the WL spectra generated in a YAG and Sapphire plates respectively.

The temporal resolution of a pump-probe spectroscopy experiment can be taken to be the instrument response function of the system, which is usually assumed to be the cross-correlation of the pump and probe beams, determined from the experimental measurement of

an instantaneous signal, e.g. the SFG signal emerged from a second order nonlinear crystal due to the coupling between the pump and probe beams [61–63, 230]. Thus, this important property of the system was obtained by measuring the SFG of pump and probe pulses, see Figure 4.2. The measured SFG signal was generated in a BBO crystal where the pump and probe beams were focused. The SFG set-up was constructed in a way that resembled the actual experimental conditions of pump-probe microspectroscopic experiments, where the pump and the probe beams propagate collinearly to each other and are focused in the sample by a high numerical aperture (NA) objective. Since every modern objective is constituted by several optical lenses with refractive indexes above of that attained in the free space, dispersion effects distort the pulses in both spatial and temporal dimensions. For this reason, the cross-correlation of the pump-probe beams was obtained changing the focusing device, going from a high (0.75) NA and low NA (0.25) objectives to literally nothing in between the beams and the BBO crystal. A sketch of the SFG set-up is shown in Figure 4.2 Panel A and the results obtained with the pump and probe beams centered at 530 and 610 nm respectively. The full width at a half maximum (FWHM) of the retrieved SFG signals using the NA = 0.75 objective was $\tau_1 = 1.60 \pm 0.02$ ps whereas for the NA = 0.25 objective the FWHM of the detected SFG signal was $\tau_2 = 1.48 \pm 0.02$ ps. For the experiments were any optics was used to focus the beams a FWHM of $\tau_3 = 0.91 \pm 0.01$ ps was obtained. In all the pump-probe microspectroscopy experiments reported in this contribution, the objective employed had a NA of 0.75. Therefore, in the following the term “temporal resolution of the TAM” is mentioned, the τ_1 value would be meant. The uncertainty on the measurements are reliable since the precision of the translational stage employed (PI, M-531.DG) was 20 nm which corresponds to a temporal delay of 7×10^{-17} s.

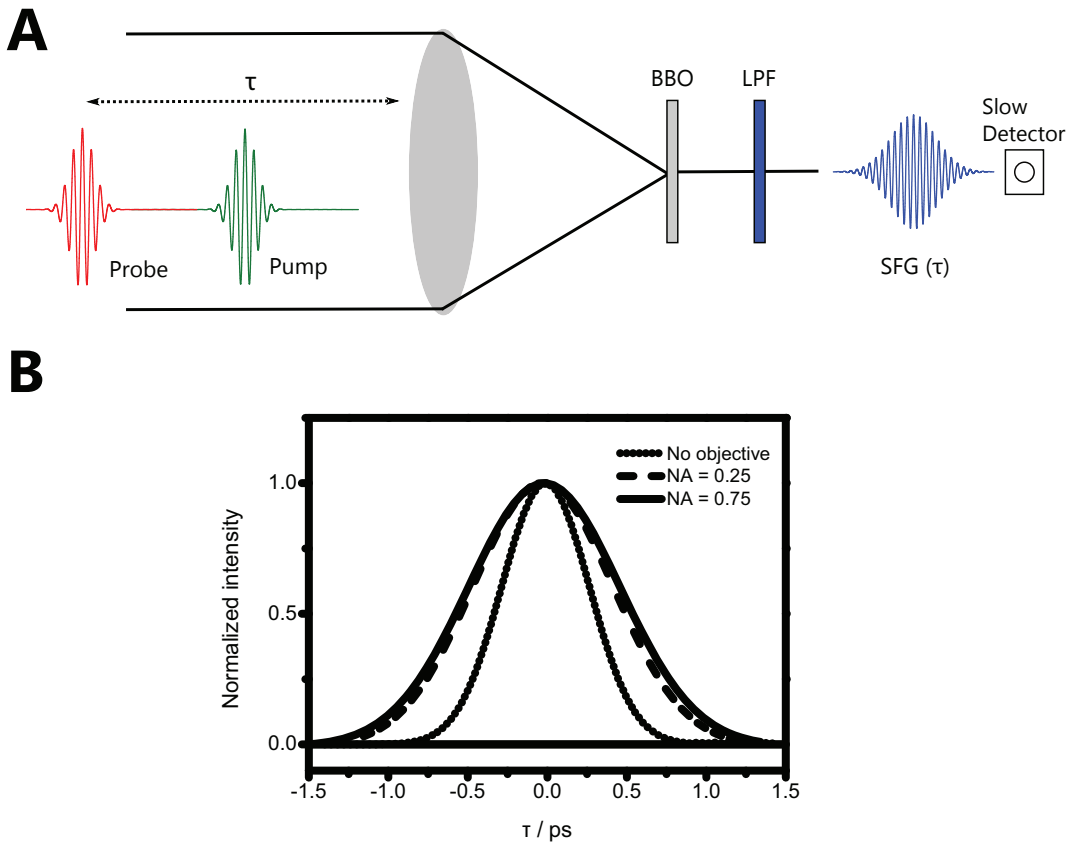

Fig. 4.2 A) Scheme of the experimental set-up constructed to determine the cross correlation of the pump and probe beams. The optical radiation is placed into a BBO crystal where SFG takes place. In this set-up each probe pulse is displaced in time while the pump pulses remain fixed. The probe and pump radiation is filtered out by means of a low pass filter (LPF). B) Fits of the SFG measurements (the data is not shown for the sake of clarity). Note the drastic increment of the FWHM induced by the addition of an optical device.

4.2 The electronics instrumentation of the TAM

The TAM relies on three optical detectors to measure the intensity of the pump and probe beams. It also depends substantially on the photo-detectors to quantify the pulse to pulse fluctuations of the beams. One of the detectors is employed to monitor the pump beam and will be termed PD1, the other two detectors, PD2 and PD3, are used to monitor the probe beam under two different circumstances: PD2 registers all the pulses that have interacted with the sample whereas PD3 accounts for those pulses which have not, serving as reference detector. This configuration of PD2 and PD3 allows to assess the degree of coherence between the pulses reaching PD2 and PD3, which turns out to be very useful to determine any possible issue induced either by the microscope or the sample itself.

The operation mode of each photodector, i.e. PD1-PD3, is based on the so called boxcar integrator (BI) [231–234]. The BI is an electronics device used to increase the S/N of measurements of repetitive signals. The major application of BIs is the detection of the response of a system, namely, biological, physical or chemical, to an external stimulus. In pump-probe experiments the driving signal of the detectors is of course synchronized with every pump pulse. The technique exploits the fact that the measured signal, which is formed by the response of the system to the applied stimulus, is given by

$$V_i(t) = V_s(t) + V_n(t) \tag{4.1}$$

Where $V_s(t)$ and $V_n(t)$ are the signal of interest and noise, respectively. If $V_s(t)$ is truly a repetitive signal, it is coherent[3] and that means it must satisfy the following condition

$$V_s(t) = V_s(t+\Theta) = V_s(t+i\Theta) \tag{4.2}$$

here Θ denotes the period of the stimulus and i is an integer. It should be noted that Θ has to be longer than the time required for the response of the system to the stimulus to die off, see Figure 4.3 panel A. The noise $V_n(t)$, however, is a random signal following a Gaussian distribution with a constant amplitude over a defined spectral range [233].

In the BI scheme the measured signal $V_i(t)$ is fed into an integrator circuit at a time τ_0 subsequent to the excitation for a period of time τ_g, known as gating time, see Figure 4.3 panels A and B. If the signal $V_i(t)$ is measured N times, the random nature of $V_n(t)$ would cause that the noise component averages to zero (usually to another baseline value) with an uncertainty proportional to $1/\sqrt{N}$. Due to its coherent nature $V_s(t)$ would, in principle,

[3] Coherent signals have a constant phase difference and the same frequency.

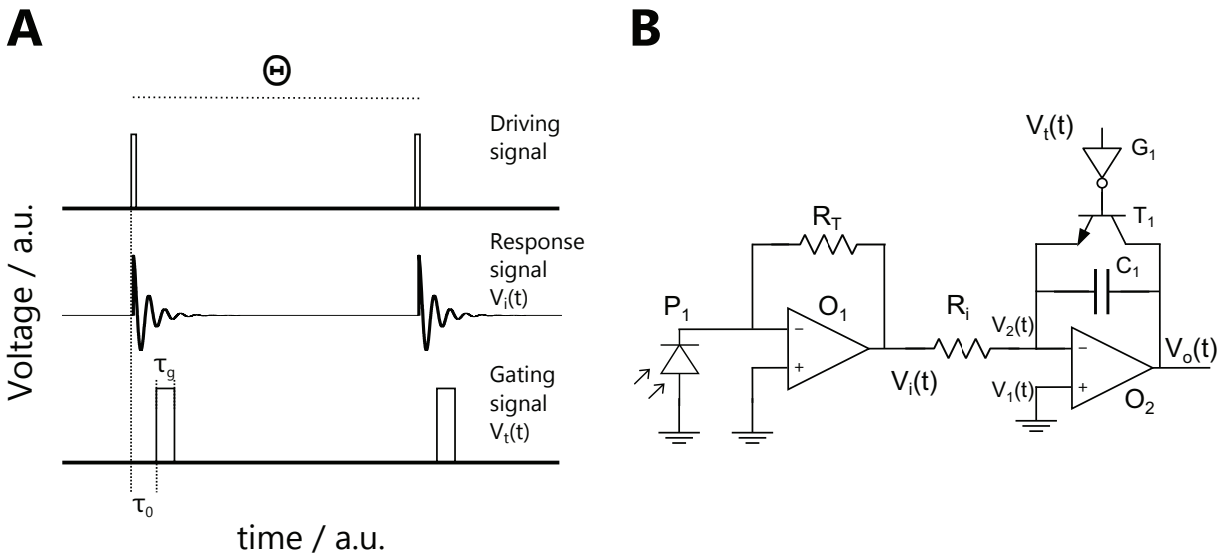

Fig. 4.3 A) The perturbation, and therefore response, induced to an arbitrary system is synchronized with the electronics instrumentation of the TAM through the driving signal. The response signal is tracked and recorded during specific periods of time τ_g every τ_0 seconds after the perturbation. B) The photoinduced currents of a photodiode are converted to voltage via a transimpedance amplifier. Subsequently, this signal will be integrated by a second operational amplifier. Note that the signal will be integrated and registered only during the gating times τ_g.

remain constant[4] over all the N measurements, leading to an increment of the S/N. Thus, the averaged value for every measurement of the BI normalized to the gating time and the number of samples N is expressed mathematically as:

$$V_{ave}(t) = \frac{1}{N}\frac{1}{\tau_g}\sum_{m=0}^{N}\left\{\int_{\tau_0}^{\tau_0+\tau_g}[V_s(t)+V_n(t)]\,dt\right\} \tag{4.3}$$

Another interesting effect appears due to the finite gating time τ_g. The high frequency components of the measurements will be filtered out since proportional factors of the form $1/\omega_m\tau_g$ appear during the integration process, ω_m is the angular frequency of the signal. In addition the measured signals will suffer phase shifts proportional to $\omega_m\tau_g$ [232, 233].

The sensors used in PD1-PD3 are InGaAs photodiodes (G10899, Hamamatsu) which posses a wide spectral range (0.5-1.7 μm) sensitivity and an active area of 2 mm. The photoinduced current in each of the photodiodes (P) is "converted" to voltage, termed $V_i(t)$, by means of a simple, but elegant, transimpedance amplifier (TIA), in this way $V_i(t)$ reflects the amounts of radiation impinging on the detector. In addition, the TIA reduces the effects

[4]In reality, the S/N ratio is also affected by the fluctuations in the repetitive signal itself, however here it is assumed that $V_s(t)$ possess a unitary degree of coherence.

of the inherent parasite capacitance of the photodiode which could lead to a slow response of the sensor [235]. The gain of each TIA can be adjusted through a variable resistor (R_T).

Once obtained a voltage that correlates with the number of photons on the photodetector, $V_i(t)$ is fed into an integrator circuit, however the system will perform the integral of $V_i(t)$ solely during the gating time τ_g of a pulsed voltage train $V_t(t)$ which is synchronized to the laser oscillator through a clock signal set by the trigger output of the laser cavity which repetition rate is 250 kHz. In this way, PD2 and PD3 will have performed two measurements in 8 μs whereas PD1 only one, which directly allows to measure with the pump on and pump off condition.

4.3 The TAM

Once discussed the physics of the technique (Section 2.2), the femto second light source (Section 4.1) and the electronics instrumentation Section (Section 4.2) of the TAM, the last step is to present and discuss the instrument. In Figure 4.4 a schematic representation of the TAM is shown. The Ytterbium-based laser seeds the pump and probe OPAs with pulsed optical beams centered at $\lambda = 1030$ nm, oscillating at 125 and 250 kHz for the pump and probe respectively and with an average pulse duration of 450 fs. The OPAs provide to the TAM the possibility to tune the wavelengths of the radiation employed to access specific excited states of molecular assemblies and the wavelength used to explore the evolution of such photoinduced states.

Each probe pulse is delayed with respect to each pump pulse by means of a gold retro-reflector displaced by a mechanical translational stage (PI, M-531.DG). As discussed in Section 4.2, a set of three photodetectors is used to monitor the intensity of the pump and probe beams. In the case of the probe beam, a beam splitter is used to divide the incident beam into two parts: one used as reference signal and another one to probe the transient absorption signal of the sample. The signal and reference beams of the probe beam are focused into PD2 and PD3 respectively. The pulses of the pump beam are measured to quantify their intensity and fluctuations, in addition, the readings of PD1 also provide a clock signal for the experiment, since each pump pulse is the driving source of the transient absorption experiment. The pump and probe beams are forced to propagate collinearly by means of a dichroic mirror. This superposition of beams is guided to a galvanometer-based scanner system (Cambridge Technologies) to scan the samples in a raster pattern. Subsequently the two collinear beams are expanded with a $4f$ system in order to fill in the entire back aperture of the focusing objective (Nikon, CFI Plan Apo Lambda 20X, NA = 0.75, WD = 1 mm) and with this achieve the maximum resolution. Once the pump and probe beams have propagate

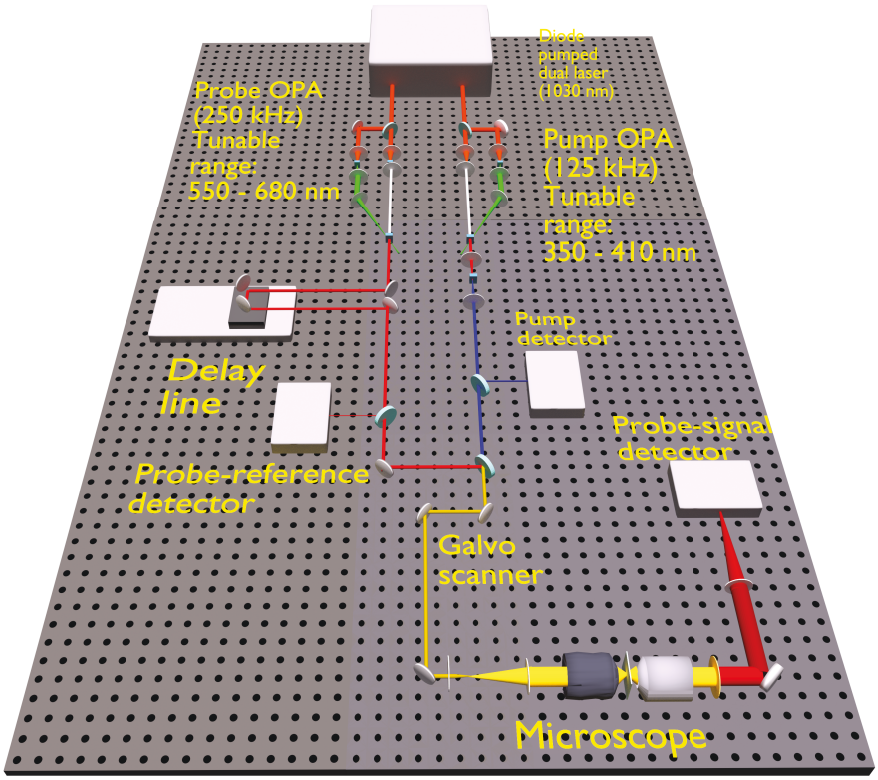

Fig. 4.4 Schematic representation of the transient absorption microscope.

through the sample, the pump beam is filtered out with an absorptive filter, whereas the probe beam is focused into PD2.

4.3.1 The sample holder

In order to map the images of different samples obtained with the TAM and other microscopes, i.e. bright and confocal laser scanning microscopes, a special set of sample holders was designed and constructed. Each sample holder consisted of a quartz plate, transparent in the spectral regions used to pump and probe the samples, with a thickness of 500 μm in which calibrated and ordered grids were drilled by an electron beam. The length of each individual square of the grids was 10 μm, such length was set at this value to easily determine the dimensions of eukaryotic cells. Numbers and letters were drilled in the sample holders to label rows and columns respectively. These sample holders were crucial in the identification of emissive regions of cells dosed with (emissive) Ruthenium-based drugs. The regions imaged with CLSM would be explored with the TAM, guaranteeing that in such regions emissive species of the dye would be localized, see Reference [152] and the next chapter. It is worth mentioning that any nonlinear effect derived from the interaction of the pump/probe beams and the sample holder was observed.

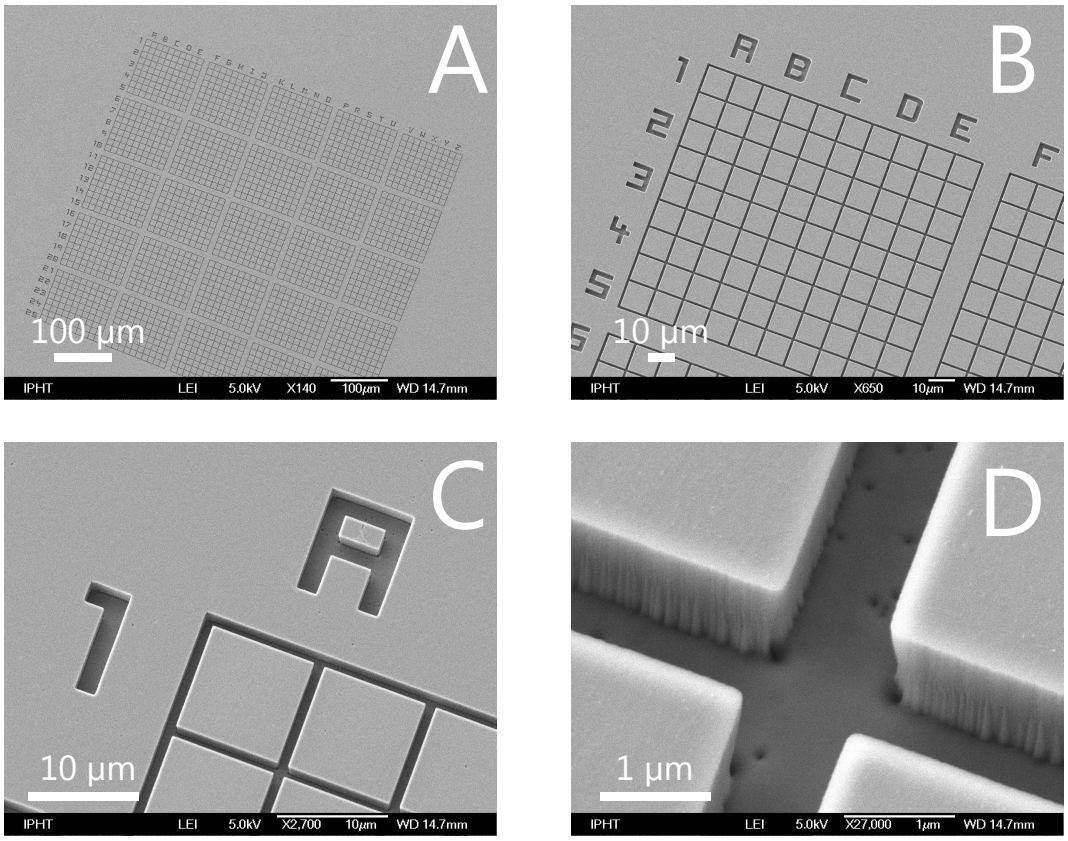

Fig. 4.5 Images of the sampler holder used for exploring cells dosed with emissive Ruthenium species recorded at different field of views. The scale bars in panels A-D) correspond to 100 µm, 10 µm, 10 µm and 1 µm, respectively.

Chapter 5

Results

The main goal of the research presented in this thesis was to investigate the way cellular environments affect a chemical species which has been designed to be used either as a marker of particular cellular components or as a photo activated chemical agent. In order to detect and determine the influence of the environment on the drugs, a systematic observation of their (steady state and time resolved) photophysics in different solvents was performed. The results of such studies served as reference for subsequent studies performed *in cellulo*. Only the results of two molecular systems, i.e. $[Ru(bpy)_2dppz]^{2+}$ and $[Ru(bpy)_2ippy]^{2+}$ will be given in this chapter.

5.1 Microspectroscopy study of $[Ru(bpy)_2dppz]^{2+}$

As discussed in Section 3.3, the photophysics of $[Ru(bpy)_2dppz]^{2+}$ is well known for several years as the steady state photophysics of the molecule has been deeply investigated by several research groups in different solvents and even *in cellulo* [167, 169, 170, 197, 200, 204]. Some scientific data has been published in which the ultrafast photophysics of $[Ru(bpy)_2dppz]^{2+}$ has been reported in aqueous solutions, DNA buffers, protic and aprotic solvents [152, 167, 169, 170, 197, 200, 204, 179, 208]. Thus, to contribute to the knowledge on the photophysics of the paradigm molecular light switch $[Ru(bpy)_2dppz]^{2+}$ in cellular environments, phospholipid vesicles, which are considered as cellular membrane models, were doped with $[Ru(bpy)_2dppz]^{2+}$.

The ultrafast photophysics of $[Ru(bpy)_2dppz]^{2+}$ was studied beforehand in reference solvents, i.e. ACN and water, in order to serve as control experiments. The results can be seen in Figure 5.1. Subsequently to photo excitation in the spectral range of 400 nm, a manifold of ^{3}MLCT is formed, where a competition between energetic and entropic factors would determine whether the equilibrated ^{3}MLCT formed has an emissive or non-radiative deactiva-

tion, in other words, thermodynamic factors would determine which state is formed either an emissive ^{3}MLCT$_{\text{bright}}$ or a dark ^{3}MLCT$_{\text{dark}}$ state. The inherent nature of these two states can be observed through analysis of the transient absorption spectra obtained with pump-probe experiments performed on $[Ru(bpy)_2dppz]^{2+}$ dissolved in protic or aprotic solvents. In Figure 5.1 Panel A the transient absorption spectra of $[Ru(bpy)_2dppz]^{2+}$ dissolved in ACN is shown whereas in Panel B the same spectroscopic property of the paradigm molecular light switch dissolved in water is plotted. The long lived transient absorption observed in ACN is associated to molecules occupying their ^{3}MLCT$_{\text{bright}}$ state while the fast decay of the transient absorption recorded in water is related to $[Ru(bpy)_2dppz]^{2+}$ molecules in which their ^{3}MLCT$_{\text{dark}}$ state has been stabilized. Note how the $[Ru(bpy)_2dppz]^{2+}$ molecules in ACN do not show a significantly relaxation in the time span of the experiments, i.e. 8 ns, while the same molecular system in water is quenched in less than 250 ps, as expected in protic environments. The reasons are detailed in Section 3.3 and the references cited there.

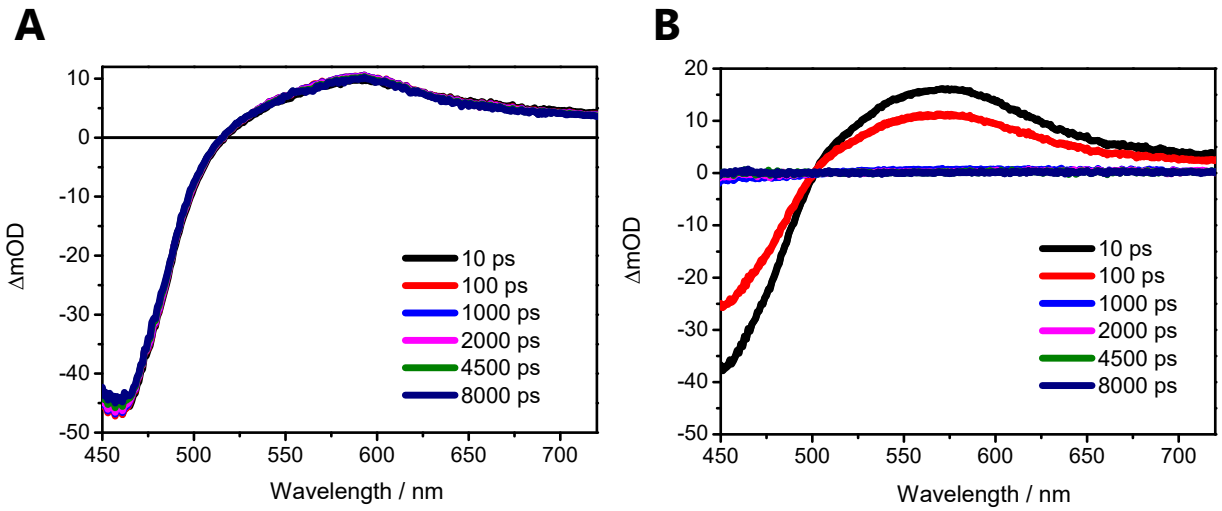

Fig. 5.1 Transient absorption spectra of $[Ru(bpy)_2dppz]^{2+}$ *dissolved in A) Acetonitrile and B) Water. In these experiments* $\lambda_{pump} = 400nm$.

Having characterized the ultrafast photophysics of the paradigm molecular light switch $[Ru(bpy)_2dppz]^{2+}$ in reference solvents, the molecules were dissolved in aqueous suspensions containing the phospholipid vesicles. As discussed in Section 3.3, the emission of $[Ru(bpy)_2dppz]^{2+}$ will be quenched as long as Hydrogen-bonding occurs between the molecules of the solvent (or another Hydrogen donor species) with the Nitrogens of the phenazine moiety of the dppz ligand. Thus, the observed luminescence, which is associated with the ^{3}MLCT$_{\text{bright}}$ state of $[Ru(bpy)_2dppz]^{2+}$ molecules, arose from those molecules which could intercalate into the phospholipid vesicles as depicted in Figure 5.2 Panel A [166]. Note that the complexes would not be fully internalized into the lipophilic moiety of the

vesicles since Coulombic forces of attraction between the hydrophilic moieties of the vesicles, which are formed by negatively charged phosphate groups, and the $[Ru(bpy)_2dppz]^{2+}$ cations take place.

To asses the intercalation of $[Ru(bpy)_2dppz]^{2+}$ molecules into the vesicles steady state emission of the suspensions containing the doped vesicles was acquired, see Figure 5.2 Panel B, where a strong luminescence centered around 680 nm was observed. As control experiments, the luminescence of aqueous solutions containing only $[Ru(bpy)_2dppz]^{2+}$ or just the phospholipid vesicles were recorded and, as expected, no luminescence was detected.

To obtain a more detailed understanding of the photophysics of $[Ru(bpy)_2dppz]^{2+}$ unfolding in an environment that resembles a very important cellular compartment of cells, i.e. the cellular membrane, the ultrafast transient absorption of phospholipid vesicles loaded with the complexes was acquired. The results, which are shown in Figure 5.2 Panel C, were obtained at different pump powers. The $^3MLCT_{bright}$ is manifested in all the experiments through the long lived transient absorption. Interestingly, a substantial quenching of the transient absorption signal was observed when the density of photons exceeded 7.50×10^{18} photons cm^{-2} per pulse. This reduction of the excited state absorption signal suggested a new deactivation path for $[Ru(bpy)_2dppz]^{2+}$ molecules and was associated to intermolecular triplet-triplet annihilation driven by intermolecular energy transfer between individual $[Ru(bpy)_2dppz]^{2+}$ complexes intercalated into the phospholipid vesicles.

In order to discard any possible energy transfer mechanism from an excited $[Ru(bpy)_2dppz]^{2+}$ molecule to the phospholipid vesicles a set of pump-probe experiments, in which the photon density of the pump beam was set at maximum, i.e. 10.00×10^{18} photons cm^{-2} per pulse, and the concentration ratio of phospholipid vesicles to $[Ru(bpy)_2dppz]^{2+}$ molecules was varied were performed. The concentration ratios used for this study were: 20 phospholipid vesicles to 1 Ru-complexes, 50 phospholipid vesicles to 1 Ru-complexes, 100 phospholipid vesicles to 1 Ru-complexes and 200 phospholipid vesicles to 1 Ru-complexes. Notably, the quenching of the long lived transient absorption appeared only in the suspension containing the smallest ratio of vesicles to Ru-complexes, i.e. 20 phospholipid vesicles to 1 Ru-complexes, see Figure 5.2 Panel D. The results observed in this set of experiments provide strong support to the notion of energy transfer between photoexcited $[Ru(bpy)_2dppz]^{2+}$ molecules followed by an exciton-exciton annihilation deactivation process, see Reference [208].

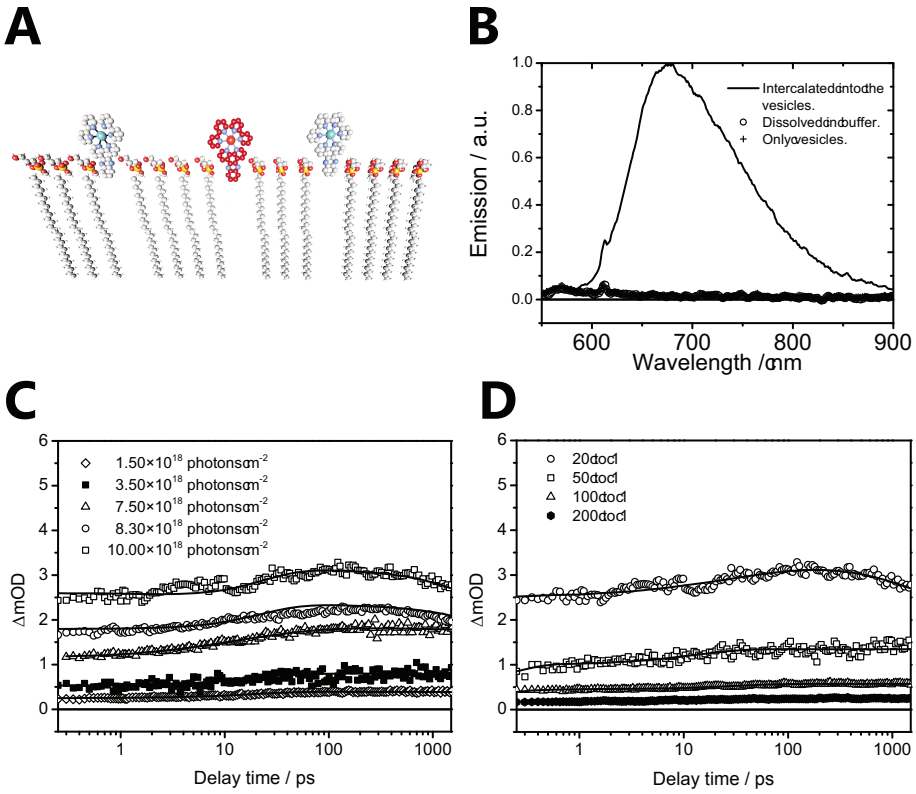

Fig. 5.2 A) Binding mode of the metallointercalator $[\mathrm{Ru(bpy)_2dppz}]^{2+}$. *B) Emission spectra of* $[\mathrm{Ru(bpy)_2dppz}]^{2+}$ *intercalated into the phospholipid vesicles, free in buffer and the corresponding emission spectrum of phospholipid vesicles in the absence of* $[\mathrm{Ru(bpy)_2dppz}]^{2+}$. *C) Excitation-dependent transient absorption kinetics of phospholipid vesicles doped with* $[\mathrm{Ru(bpy)_2dppz}]^{2+}$. *D) Concentration dependent experiments. Transient absorption kinetics pumping with a fixed photon density of* 10.00×10^{18} cm^{-2} *per pulse and a varied concentration of phospholipid vesicles. The pump-probe experiments shown in Panels C and D were carried out pumping at* $\lambda_{pump} = 400$ *nm and probing at* $\lambda_{probe} = 580$ *nm.*

Once studied the photo-induced dynamics of $[Ru(bpy)_2dppz]^{2+}$ molecules in an environment that resembles the cellular membrane, HepG2 cells were dosed[1] with $[Ru(bpy)_2dppz]^{2+}$. The study of $[Ru(bpy)_2dppz]^{2+}$ embedded in eukaryotic cells begun with the characterization of the cellular environment itself. To do this, a lysate of HepG2 was obtained through sonication of cells. This solution, which contained the leftovers of HepG2 cells and was transparent to the human sight, was photo-irradiated with a continuous wave laser centered at $\lambda_{exc} = 400$ nm. This process surprisingly lead to the emission of light, see Figure 5.3 Panel A. The following step was to incorporate $[Ru(bpy)_2dppz]^{2+}$ molecules into the lysate to subsequently study the emission of the sample. Since the lysate was immersed in phosphate-buffered saline (PBS), an aqueous solution, only those $[Ru(bpy)_2dppz]^{2+}$ molecules that managed to intercalate into any cellular structure, e.g. DNA or cellular membrane, and in this way get isolation from water molecules would emit. Strong emission arising from photoexcited $[Ru(bpy)_2dppz]^{2+}$ molecules was indeed observed by exciting the dosed lysate at $\lambda_{exc} = 400$ nm, see Figure 5.3 Panel A. Note that the inherent emission of the lysate (i.e. lysate autofluorescence) centered around 490 nm is present on the emission spectrum of the dosed lysate, however the emission originating from $^3MLCT_{bright}$ states of photoexcited $[Ru(bpy)_2dppz]^{2+}$ molecules was significatively more intense.

Before studying the ultrafast photoinduced dynamics of $[Ru(bpy)_2dppz]^{2+}$ molecules *in cellulo* using the set-up shown in Figure 4.4, the characteristic kinetics trace of control cells, i.e. HepG2 cells which did not contain $[Ru(bpy)_2dppz]^{2+}$, was determined. The arithmetic mean (and the corresponding fit) of more than 50 control cells is shown in Figure 5.3 Panel B. As can be seen in Figure 5.3 Panel B a relatively slow rise in the transient absorption signal is observed. Once the signal reached a maximum value it decayed very fast, reaching zero in ca. 100 ps.

A very similar trace was observed from dosed cells, see Figure 5.3 Panel C in which the characteristic kinetics trace of more than 100 dosed cells is plotted. However such kinetics trace showed two substantial differences: the magnitude of the pinnacle of the signal was almost three times the corresponding value obtained in control cells and a long lived

[1] As an in cellulo model system for the investigation of the photoinduced dynamics shown in this chapter, the HepG2 human liver cancer cell line was chosen. HepG2 cells were cultivated in RPMI 1640 liquid medium with 20 mM HEPES, stable glutamine, 10% fetal bovine serum together with 100 units/mL of penicillin and 100 μg/mL of streptomycin. 75 cm^2 cell culture flasks were used for cultivation. The cells were maintained in 5% CO_2 incubator at 37 °C and every second day the medium was changed until 90% confluence was reached. After cells were detached by a 0.05% of trypsin-EDTA solution, they were transferred onto the sample holders, see Section 4.3.1, and cultivated for 24 hours with either 50 μM of $[Ru(bpy)_2dppz]^{2+}$ or 20 μM of $[Ru(bpy)_2ippy]^{2+}$ solution depending on the study or without Ru-complex for control experiments. Fixation of the cells with 10% neutral buffered formalin solution for 60 minutes was performed with following washing in distillate water step. The slides were dried and stored at +4 °C until the samples were studied with the TAM.

excited state absorption; the latter is a reminiscent of the dynamics shown by photoexcited $[Ru(bpy)_2dppz]^{2+}$ molecules occupying the $^3MLCT_{bright}$ discussed above.

Recent studies performed with the same set-up depicted in Figure 4.4 shown that no excited state signal was obtained from undosed (or control) MCF7 (a different cell line). Thus, the use of MCF7 instead of HepG2 is recommended for future work as no cellular intrinsic back-ground signal is detected.

The results gathered with this set of experiments, and all others concerning the acquisition of kinetics traces, were obtained by recording the transient absorption signal after focusing the pump and probe beams in a particular point of interest in the cells. The software of the microscope together with its hardware are designed in a way that such point of interest would correspond to a pixel of the acquired image allowing the user to determine with high confidence which region of the cell was studied.

In an attempt to determine how the transient absorption kinetics of $[Ru(bpy)_2dppz]^{2+}$ molecules *in cellulo* differ from the kinetics observed in reference samples, the characteristic kinetics of $[Ru(bpy)_2dppz]^{2+}$ embedded in HepG2 cells was compared to the transient absorption kinetics obtained with the conventional fs-set-up and the results are shown in Figure 5.3 Panel D. The long lived transient absorption associated to the $^3MLCT_{bright}$ state and the rapidly quenched transient absorption related to the $^3MLCT_{dark}$ state can readily be observed in the kinetics traces obtained in acetonitrile and water respectively. In the cell lysate, however, a "mixture" of the typical photo induced dynamics of $[Ru(bpy)_2dppz]^{2+}$ dissolved in protic and aprotic solvents is observed. The recorded kinetics trace decays rapidly, in ca. 250 ps, however such decay does not go down to zero since excited state absorption, which is associated to the long lived and emissive $^3MLCT_{bright}$ state, is observed in the long delay times. This can be explained by taking into account that not all the $[Ru(bpy)_2dppz]^{2+}$ molecules could intercalated into any cellular compartment, thus such molecules diffuse freely in the aqueous PBS. Nevertheless, the molecules that were isolated from water molecules due to intercalation to some cellular leftover are set in the $^3MLCT_{bright}$ state upon photoexcitation.

The characteristic transient kinetics observed *in cellulo* is build up by three processes: a fast rise of ca. 1.1 ps, a steep decay and a plateau. The first process can be either an artifact or the natural response of the dye in cellular environments. The former statement is given since the microscope itself can induce such artifacts, e.g. the temporal resolution, see Section 4.1, is in the range of the rise of the kinetics traces. If this is not the case, then coherent artifacts, as two photon absorption, Kerr effect or self phase modulation, could originate the pronounced rise. It is important to mention that such pattern has been observed with different samples and even in different microscopes. The second process building up the characteristic kinetics of

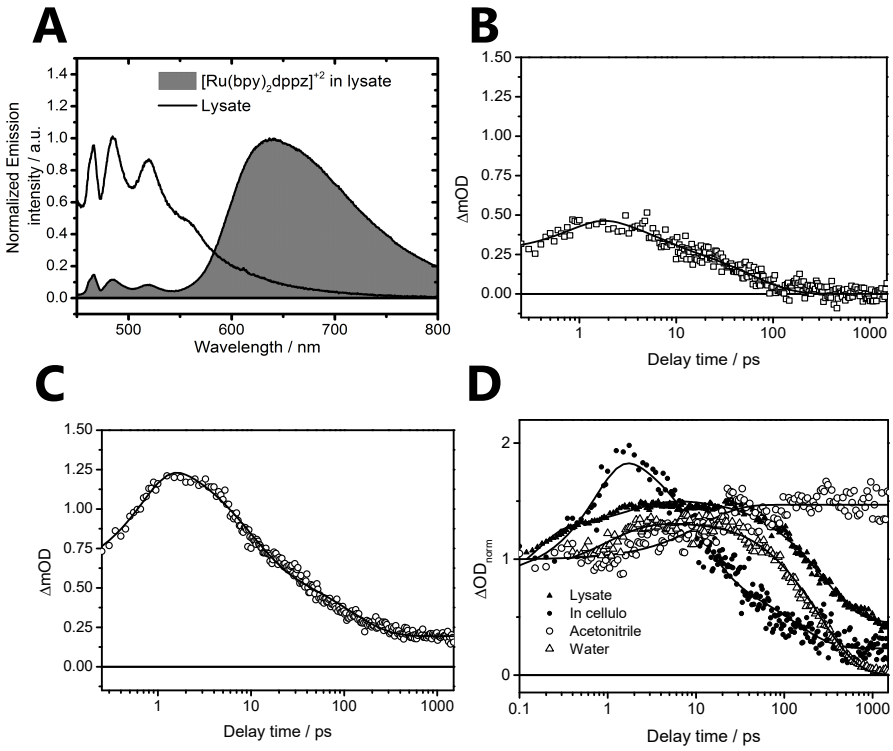

Fig. 5.3 A) Emission spectra of a pure HepG2 lysate alongside a HepG2 lysate dosed with $[Ru(bpy)_2dppz]^{2+}$. *The excitation wavelength was centered at* $\lambda_{exc} = 400$ *nm. B) and C) Are the characteristic transient absorption kinetics obtained from control and dosed HepG2 cells, respectively, pumping at* $\lambda_{pump} = 435$ *nm and probing at* $\lambda_{probe} = 580$ *nm. D) Transient absorption kinetics of* $[Ru(bpy)_2dppz]^{2+}$ *embedded in different environments. The kinetics traces correspond to the spectral region centered at 580 nm. In panel D the pump wavelength was centered at* $\lambda_{pump} = 400$ *nm whereas for the in cellulo experiments* $\lambda_{pump} = 435$ *nm.*

$[Ru(bpy)_2dppz]^{2+}$ is assigned to the stabilization between the $^3MLCT_{bright}$ and $^3MLCT_{dark}$ states whereas the third process is of course the pure manifestation of the $^3MLCT_{bright}$ state.

It is very important to mention that in both types of samples, i.e. control and dosed cells, the studied cells were fixed and that excited states dynamics appeared only in the nuclei of the cells, meaning that region others than the nucleus, e.g. the cytosol, did not show excited state dynamics. In the case of dosed cells this result is in very good agreement with steady state emission imaging of dosed cells, as an example see Figures 3.3, 3.8 and Figure 5.4.

It is needless to say that the kinetics exhibited by $[Ru(bpy)_2dppz]^{2+}$ depends significatively on the environment, but in addition, how and where the paradigm molecular light switch is deposited. A detailed discussion on this research can be found in Reference [152].

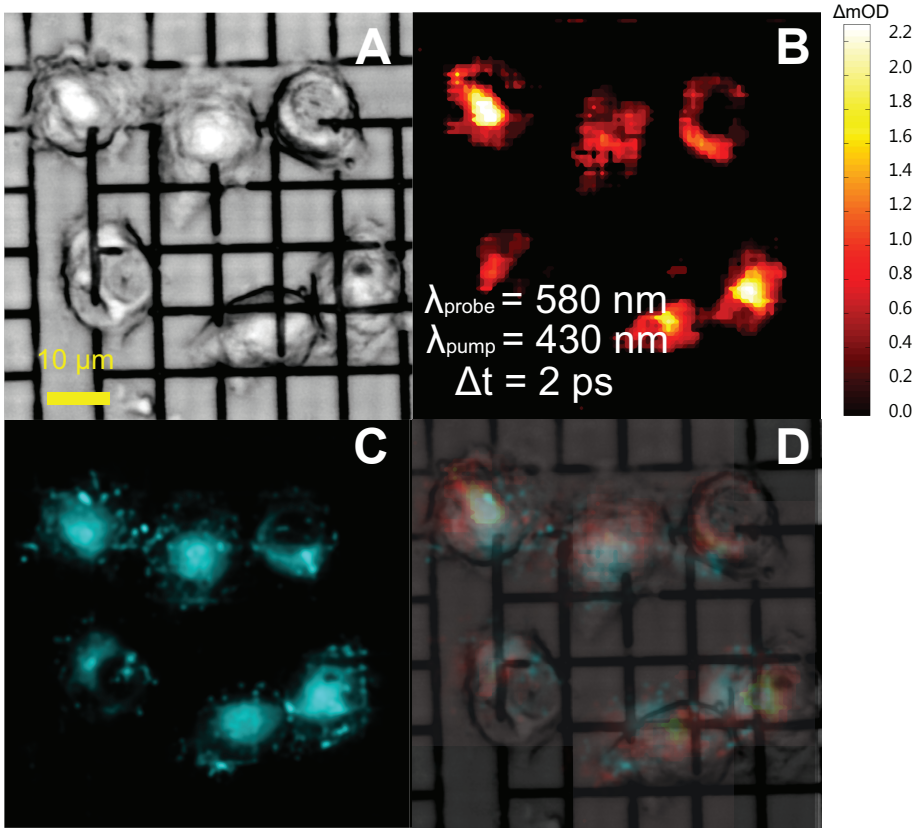

Fig. 5.4 Dosed cells imaged using different microscopy techniques. A) Phase image, B) Transient absorption image, C) Emission image and D) Overlay of panels A-C).

5.2 Microspectroscopy study of $[Ru(bpy)_2ippy]^{2+}$

$[Ru(bpy)_2ippy]^{2+}$ is a potential candidate for being used in photoactivated chemotherapy. The dye, which molecular structure is shown in Figure 5.5, is absorbed relatively fast by living cells requiring only one hour of incubation to obtain substantial amounts of dye inside the cells [182, 236]. This fast diffusion of the dye into the cells could be a result of the high lipophilicity of the ippy ligand and the cationic nature of the molecule, see Section 3.4. Once deposited into the cells, $[Ru(bpy)_2ippy]^{2+}$ is supposed to accumulate into the cytosol, at least this has been reported for HL-60 [182], and in addition the dye has been considered a highly cytotoxic species upon photo-irradiation, capable to photo-cleave DNA [182]. A complete time resolved and steady-state spectroscopic characterization in solutions has been carried out by the group of Professor Dietzek [182, 236].

In order to perform a systematic study of the kinetics traces obtained from different locations of HepG2 cells dosed with $[Ru(bpy)_2ippy]^{2+}$ it is important to know "where" the dye accumulates the most. One way to visualize the deposition of (emissive) $[Ru(bpy)_2ippy]^{2+}$

species in cellular compartments is of course through steady state emission imaging. Therefore HepG2 cells dosed with $[Ru(bpy)_2ippy]^{2+}$ were co-incubated with standard DNA and cytosol markers, namely, DAPI and Alexa, respectively. The images obtained are shown in Figure 5.5. As expected, DAPI binds to DNA whereas Alexa, at the side of $[Ru(bpy)_2ippy]^{2+}$, accumulated in the cytosol.

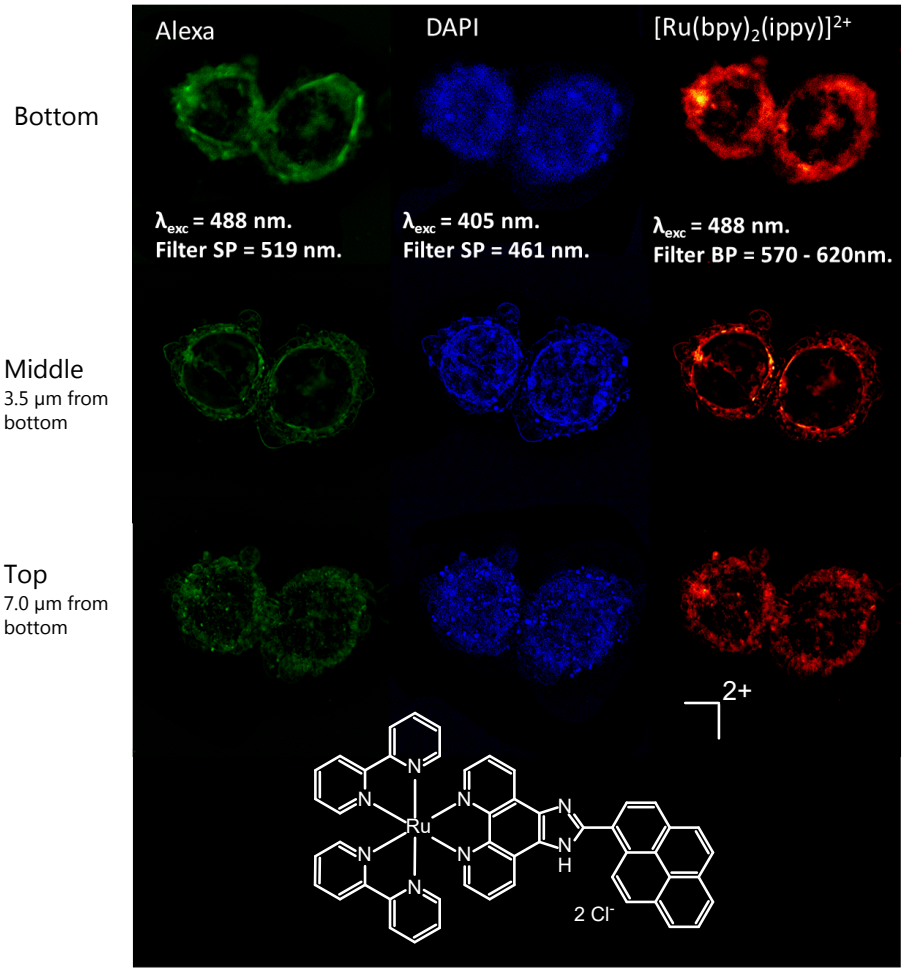

Fig. 5.5 HepG2 cells dosed with $[Ru(bpy)_2ippy]^{2+}$ *were co-incubated with standard cellular markers DAPI and Alexa. As can be seen in the Figure, the emission arising from Alexa overlaps with that of* $[Ru(bpy)_2ippy]^{2+}$. *This suggests that emissive* $[Ru(bpy)_2ippy]^{2+}$ *photoexcited species lay in the cytosol of the cells.*

The following step in this investigation was the systematic measurement of kinetics traces of dosed cells with $[Ru(bpy)_2ippy]^{2+}$. Figure 5.6 shows exemplary the probed cellular regions and the corresponding kinetics traces of cells which nuclei are readily recognized from a simple phase-contrast image. Excited state absorption was recorded from regions outside the nuclei of the cells, however, opposite to the expectations, strong excited state absorption was recorded from the nuclei of the cells. Similarly to the excited state absorption

exhibited by $[Ru(bpy)_2dppz]^{2+}$ *in cellulo* the kinetics traces of $[Ru(bpy)_2ippy]^{2+}$ are again a three steps process, see above. It is worth noticing that the maximum excited state absorption of photo-excited $[Ru(bpy)_2ippy]^{2+}$ species could reach values almost six times higher compared to the maximum value of the characteristic kinetics exhibited by photo-excited $[Ru(bpy)_2dppz]^{2+}$ species *in cellulo*, see Figures 5.3 Panel C and 5.6. This is attributed to a higher cellular uptake of $[Ru(bpy)_2ippy]^{2+}$ compared to $[Ru(bpy)_2dppz]^{2+}$, resulted from the higher lipophilicity of the ippy ligand. The ^{3}MLCT manifold of $[Ru(bpy)_2ippy]^{2+}$ is different to that of $[Ru(bpy)_2dppz]^{2+}$. According to Dietzek and co-workers this manifold is formed by two ^{3}MLCT states. One of them decays by emitting light spontaneously whereas the other ^{3}MLCT exhibits a delayed emission. In addition, they also reported the observation of a long lived non-emissive ^{3}IL state [236]. Therefore the plateau of the kinetics traces recorded in HepG2 cells dosed with $[Ru(bpy)_2ippy]^{2+}$ would correspond to one of the long-lived processes described before [236].

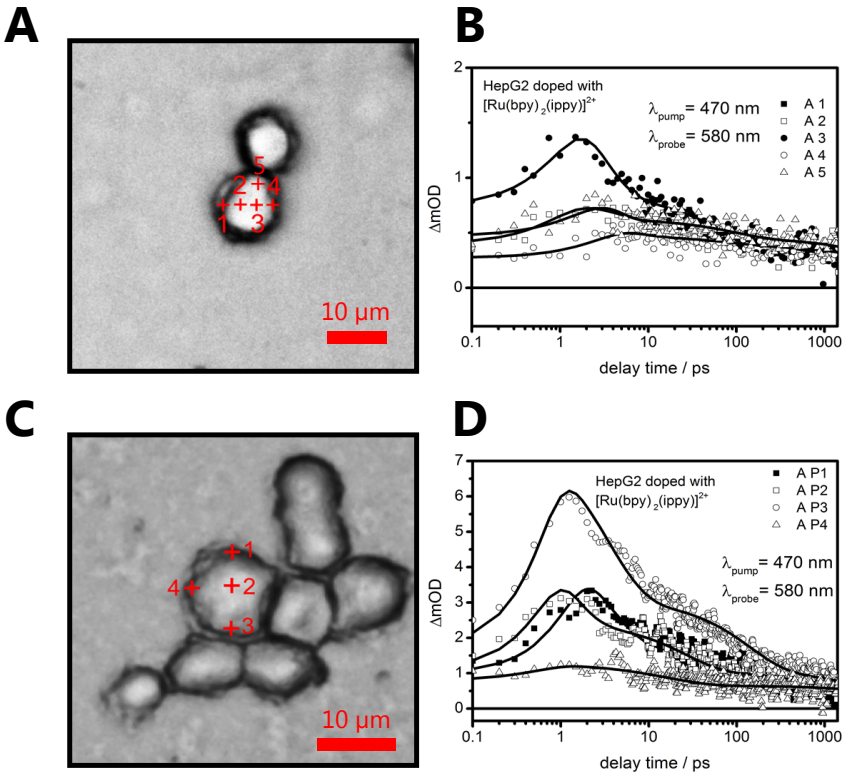

Fig. 5.6 A) and C) show exemplary the selected regions for in cellulo experiments performed on HepG2 cells dosed with $[Ru(bpy)_2ippy]^{2+}$. *Kinetics traces were obtained in specific points all over the cell, including the nuclei and cytosol. The results of the cells shown in Panel A and C were choose due to the fact that the nuclei of the cells could be distinguished without any staining procedure. B) and D) show the corresponding kinetics traces of the points marked on the cells of panels A) and C) respectively.*

It should be remarked that the three processes involved with photo excited $[Ru(bpy)_2ippy]^{2+}$ species posses life times in the micro-second regime, i.e. way longer than the experimentally accessible delay times attained (up to 2 ns) with the set-up shown in Figure 4.4. The last statement implies that, the TAM is capable of imaging both emissive and non-emissive states of photoexcited $[Ru(bpy)_2ippy]^{2+}$ species. The capacity of the TAM to image "dark states" was tested with this molecular system. To do this the steady state emission image of dosed HepG2 cells was acquired and compared to transient absorption images of the same cells. The transient absorption images were obtained after setting the delay line to a specific position that would correspond to a particular delay between pump and probe pulses. Figure 5.7 shows exemplary a set of typical results. As can be seen in Figure 5.7 Panel A emission is observed all over the cell, however, the strongest emission is captured outside the nuclei of the cells. A similar trend is observed in the transient absorption images obtained at short delay times, i.e. < 10 ps, see Figure 5.7 Panels D-E. Interestingly an image, which contrast relies on transient absorption, of a structure that resembles the form of the studied cell was obtained at a delay time of 1850 ps between pump and probe pulses, see Panel F of the same Figure. Based on the inherent photophysics of photoexcited $[Ru(bpy)_2ippy]^{2+}$ species the excited state absorption gathered in each pixel could arise from any of the three long-lived states described above [236], nevertheless, results premature to conclude which of the three possible long lived states could originate the contrast of these images. In order to give a reliable conclusion, this type of samples need be investigated under time resolved imaging systems with longer time spans. This could be achieved by just adding a longer time span to the microscope shown in Figure 4.4 or with time resolved emission systems, e.g. FLIM.

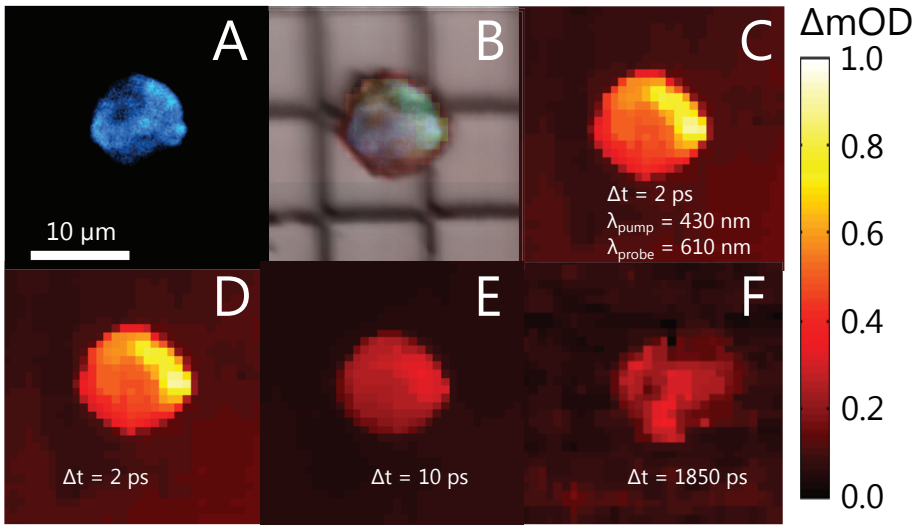

Fig. 5.7 Imaging of dosed HepG2 cells with $[\mathrm{Ru(bpy)_2ippy}]^{2+}$. *A) Emission image, exciting at* $\lambda_{exc} = 450$ *nm and detecting above* 650 *nm, B) Overlay of panels A and C, C-F) Transient absorption images at three different delay times.*

References

[1] Herbert, S. & Darwin, C. Darwin's geology. *Nature Geoscience* **2**, 81–81 (2009).

[2] Prestayko, A. W., D'Aoust, J. C., Issell, B. F. & Crooke, S. T. Cisplatin (cis-diamminedichloroplatinum II). *Cancer Treatment Reviews* **6**, 17–39 (1979).

[3] Siddik, Z. H. Cisplatin: mode of cytotoxic action and molecular basis of resistance. *Oncogene* **22**, 7265–79 (2003). NIHMS150003.

[4] Rajeswaran, A., Trojan, A., Burnand, B. & Giannelli, M. Efficacy and side effects of cisplatin- and carboplatin-based doublet chemotherapeutic regimens versus non-platinum-based doublet chemotherapeutic regimens as first line treatment of metastatic non-small cell lung carcinoma: a systematic review of randomi. *Lung cancer (Amsterdam, Netherlands)* **59**, 1–11 (2008).

[5] Leung, C.-H., Lin, S., Zhong, H.-J. & Ma, D.-L. Metal complexes as potential modulators of inflammatory and autoimmune responses. *Chemical Science* **6**, 871–884 (2015).

[6] Kupcewicz, B. *et al.* Copper(II) complexes with derivatives of pyrazole as potential antioxidant enzyme mimics. *Medicinal Chemistry Research* **22**, 2395–2402 (2013).

[7] Geldmacher, Y., Oleszak, M. & Sheldrick, W. S. Rhodium(III) and iridium(III) complexes as anticancer agents. *Inorganica Chimica Acta* **393**, 84–102 (2012).

[8] Sava, G., Bergamo, A. & Dyson, P. J. Metal-based antitumour drugs in the post-genomic era: what comes next? *Dalton transactions (Cambridge, England : 2003)* **40**, 9069–9075 (2011).

[9] Clavel, C. M., Păunescu, E., Nowak-Sliwinska, P. & Dyson, P. J. Thermoresponsive organometallic arene ruthenium complexes for tumour targeting. *Chemical Science* **5**, 1097 (2014).

[10] Gasser, G., Ott, I. & Metzler-Nolte, N. Organometallic anticancer compounds. *Journal of Medicinal Chemistry* **54**, 3–25 (2011).

[11] Kljun, J. *et al.* New uses for old drugs: Attempts to convert quinolone antibacterials into potential anticancer agents containing ruthenium. *Inorganic Chemistry* **52**, 9039–9052 (2013).

[12] Komor, A. C. & Barton, J. K. The path for metal complexes to a DNA target. *Chemical communications* **49**, 3617–3630 (2013).

[13] Che, C.-M. & Sun, R. W.-Y. Therapeutic applications of gold complexes: lipophilic gold(III) cations and gold(I) complexes for anti-cancer treatment. *Chemical Communications* **34**, 9554–9560 (2011).

[14] Dörr, M. & Meggers, E. Metal complexes as structural templates for targeting proteins. *Current Opinion in Chemical Biology* **19**, 76–81 (2014).

[15] Liu, Z. & Sadler, P. J. Organoiridium complexes: anticancer agents and catalysts. *Accounts of chemical research* **47**, 1174–85 (2014).

[16] Farrer, N. J., Salassa, L. & Sadler, P. J. Photoactivated chemotherapy (PACT): the potential of excited-state d-block metals in medicine. *Dalton transactions (Cambridge, England : 2003)* **44**, 10690–10701 (2009).

[17] Ma, D. L., He, H. Z., Leung, K. H., Chan, D. S. H. & Leung, C. H. Bioactive luminescent transition-metal complexes for biomedical applications. *Angewandte Chemie - International Edition* **52**, 7666–7682 (2013).

[18] Gustafsson, M. G. L. Nonlinear structured-illumination microscopy: wide-field fluorescence imaging with theoretically unlimited resolution. *Proceedings of the National Academy of Sciences of the United States of America* **102**, 13081–13086 (2005).

[19] Hofmann, M., Eggeling, C., Jakobs, S. & Hell, S. W. Breaking the diffraction barrier in fluorescence microscopy at low light intensities by using reversibly photoswitchable proteins. *Proceedings of the National Academy of Sciences* **102**, 17565–17569 (2005).

[20] Willig, K. I., Rizzoli, S. O., Westphal, V., Jahn, R. & Hell, S. W. STED microscopy reveals that synaptotagmin remains clustered after synaptic vesicle exocytosis. *Nature* **440**, 935–939 (2006).

[21] Betzig, E. & Trautman, J. K. Near-field optics: microscopy, spectroscopy, and surface modification beyond the diffraction limit. *Science* **257**, 189–195 (1992).

[22] Betzig, E. *et al.* Imaging intracellular fluorescent proteins at nanometer resolution. *Science (New York, N.Y.)* **313**, 1642–5 (2006).

[23] Mukamel, S. *Principles of Nonlinear Optical Spectroscopy* (Oxford University Press, 1995), first edn.

[24] Zewail, A. H. Femtochemistry: Recent Progress in Studies of Dynamics and Control of Reactions and Their Transition States. *The Journal of Physical Chemistry* **100**, 12701–12724 (1996).

[25] Rosker, M. J., Dantus, M. & Zewail, A. H. Femtosecond Clocking of the Chemical-Bond. *Science* **241**, 1200–1202 (1988).

[26] Dantus, M., Bowman, R. M. & Zewail, A. H. Femtosecond laser observations of molecular vibration and rotation. *Nature* **343**, 737–739 (1990).

[27] Rosker, M. J., Dantus, M. & Zewail, A. H. Femtosecond real-time probing of reactions. I. The technique. *The Journal of Chemical Physics* **89**, 6113 (1988).

[28] Dantus, M., Rosker, M. J. & Zewail, A. H. Femtosecond real-time probing of reactions. II. The dissociation reaction of ICN. *J. Chem. Phys.* **89**, 6128–6140 (1988).

[29] Rosker, M. J., Wise, F. W. & Tang, C. L. Femtosecond relaxation dynamics of large molecules. *Physical Review Letters* **57**, 321–324 (1986).

[30] Zhang, Y. *et al.* UV-Induced Proton-Coupled Electron Transfer in Cyclic DNA Miniduplexes. *Journal of the American Chemical Society* **138**, 7395–7401 (2016).

[31] Gradinaru, C. C., Pascal, A. A., Mourik, F. V., Robert, B. & Horton, P. Ultrafast Evolution of the Excited States in the Chlorophyll a / b Complex CP29 from Green Plants Studied by Energy-Selective Pump - Probe Spectroscopy **2960**, 1143–1149 (1998).

[32] Nagarajan, V., Johnson, E. T., Williams, J. C. & Parson, W. W. Femtosecond Pump-Probe Spectroscopy of the B850 Antenna Complex of Rhodobacter sphaeroides at Room Temperature. *J. Phys. Chem. B* **103**, 2297–2309 (1999).

[33] Freiberg, A., Jackson, J. A., Lin, S. & Woodbury, N. W. Subpicosecond Pump–Supercontinuum Probe Spectroscopy of LH2 Photosynthetic Antenna Proteins at Low Temperature. *The Journal of Physical Chemistry A* **102**, 4372–4380 (1998).

[34] Rosca, F. *et al.* Wavelength selective modulation in femtosecond pump-probe spectroscopy and its application to heme proteins. *Journal of Chemical Physics* **114**, 10884–10898 (2001).

[35] Zhu, L., Sage, J. T. & Champion, P. M. Observation of coherent reaction dynamics in heme proteins. *Science (New York, N.Y.)* **266**, 629–632 (1994).

[36] Cerullo, G., Polli, G., Lanzani, G. & Cogdell, R. J. Photosynthetic light harvesting by carotenoids: detectionof an intermediate excited state. *Science* **298**, 2395–2398 (2002).

[37] Schoenlein, R. W., Peteanu, L. L. A., Mathies, R. A. & Shank, C. V. The first step in vision: femtosecond isomerization of rhodopsin (1991).

[38] Wang, Q., Schoenlein, R. W., Peteanu, L. A., Mathies, R. A. & Shank, C. V. Vibrationally coherent photochemistry in the femtosecond primary event of vision. *Science (New York, N.Y.)* **266**, 422–424 (1994).

[39] Eid, J. *et al.* Ultrafast pump-probe reflectance spectroscopy: Why sodium makes Cu(In,Ga)Se2 solar cells better. *Solar Energy Materials and Solar Cells* **140**, 33–37 (2015).

[40] Chin, K. K. *et al.* Pump-probe spectroscopy and circular dichroism of nanocrystalline benzophenone–towards absolute kinetic measurements in solid state photochemical reactions. *Chemical communications (Cambridge, England)* 4266–4268 (2007).

[41] Grancini, G. *et al.* Hot exciton dissociation in polymer solar cells. *Nature Materials* **11**, 1–5 (2012).

[42] Chen, S.-C. *et al.* In-Situ Probing Plasmonic Energy Transfer in Cu(In, Ga)Se-2 Solar Cells by Ultrabroadband Femtosecond Pump-Probe Spectroscopy. *Scientific Reports* **5**, 1–7 (2015).

[43] Yan, Y. J. & Mukamel, S. Femtosecond pump-probe spectroscopy of polyatomic molecules in condensed phases (1990). arXiv:1011.1669v3.

[44] Bosma, W. B., Yan, Y. J. & Mukamel, S. Impulsive pump-probe and photon-echo spectroscopies of dye molecules in condensed phases (1990).

[45] Knopp, G., Schmitt, M., Materny, A. & Kiefer, W. Femtosecond Time-Resolved Pump- Probe Spectroscopy of NaI in Rare-Gas Environment. *J. Phys. Chem. A* **101**, 4852–4859 (1997).

[46] Settersten, T. B. & Linne, M. A. Picosecond pump-probe absorption spectroscopy in gases: models and experimental validation. *Applied Optics* **41**, 2869–2878 (2002).

[47] Koch, C. P. & Kosloff, R. Pump-Probe spectroscopy of two-Body correlations in ultracold gases. *Physical Review Letters* **103**, 1–4 (2009).

[48] Cerullo, G., Manzoni, C., Lüer, L. & Polli, D. Time-resolved methods in biophysics. 4. Broadband pump-probe spectroscopy system with sub-20 fs temporal resolution for the study of energy transfer processes in photosynthesis. *Photochemical & photobiological sciences : Official journal of the European Photochemistry Association and the European Society for Photobiology* **6**, 135–144 (2007).

[49] Mukamel, S. Femtosecond Optical Spectroscopy - A Direct Look At Elementary Chemical Events. *Annual Review of Physical Chemistry* **41**, 647–681 (1990).

[50] Dioumaev, A. K. Evaluation of intrinsic chemical kinetics and transient product spectra from time-resolved spectroscopic data. *Biophysical Chemistry* **67**, 1–25 (1997).

[51] Van Stokkum, I. H. M., Larsen, D. S. & Van Grondelle, R. Global and target analysis of time-resolved spectra. *Biochimica et Biophysica Acta - Bioenergetics* **1657**, 82–104 (2004).

[52] Puxty, G., Maeder, M. & Hungerbühler, K. Tutorial on the fitting of kinetics models to multivariate spectroscopic measurements with non-linear least-squares regression. *Chemometrics and Intelligent Laboratory Systems* **81**, 149–164 (2006).

[53] Parson, W. W. *Modern Optical Spectroscopy*, vol. 1 (2007).

[54] Bonneau, R., Wirz, J. & Zuberbuhler, A. D. Methods for the analysis of transient absorbance data. *Pure & Appl. Chem.* **69**, 979–992 (1997).

[55] Beechem, J. M., Ameloot, M. & Brand, L. Global and Target Analysis of Complex Decay Phenomena. *Instrumentation Science & Technology* **14**, 379–402 (1985).

[56] Larsen, O. F. a. *et al.* Electronic states in 2-aminopurine revealed by ultrafast transient absorption and target analysis. *Chemical Physics Letters* **371**, 157–163 (2003).

[57] Dyson, R. M., Kaderli, S., Lawrance, G. a., Maeder, M. & Zunderbuhler, a. D. Second order global analysis: the evaluation of series of spectrophotometric titrations for improved determination of equilibrium constants. *Analytica Chimica Acta* **353**, 381–393 (1997).

[58] Lakowicz, J. R. *Topics in Fluorescence Spectroscopy*, vol. 2 (Springer US, 2002), 1 edn.

[59] Rullière, C. *Femtosecond laser pulses* (Springer, 2005), first edn. 1501.00060.

[60] Berera, R., van Grondelle, R. & Kennis, J. T. M. Ultrafast transient absorption spectroscopy: Principles and application to photosynthetic systems (2009).

[61] Ziolek, M., Lorenc, M. & Naskrecki, R. Determination of the temporal response function in femtosecond pump-probe systems. *Applied Physics B-Lasers and Optics* **72**, 843–847 (2001).

[62] Polli, D., Brida, D., Mukamel, S., Lanzani, G. & Cerullo, G. Effective temporal resolution in pump-probe spectroscopy with strongly chirped pulses. *Physical Review A - Atomic, Molecular, and Optical Physics* **82**, 1–8 (2010).

[63] Vardeny, Z. & Tauc, J. Picosecond coherence coupling in the pump and probe technique. *Optics Communications* **39**, 396–400 (1981).

[64] Jackson, J. D. *Classical Electrodynamics* (Wiley, 1998), third edn.

[65] Boyd, R. W. *Nonlinear Optics.* (Academic Press, San Diego, CA, 2003), third edn.

[66] Born, M. & Wolf, E. *Principles of Optics* (Cambridge University Press, 2000), 7th edn.

[67] Armstrong, J. A., Bloembergen, N., Ducuing, J. & Pershan, P. S. Interactions between Light Waves in a Nonlinear Dielectric. *Physical Reviews* **127**, 1918–1939 (1962).

[68] Minck, R. W., Terhune, R. W. & Wang, C. C. Nonlinear Optics. *Appl. Opt.* **5**, 1595–1612 (1996).

[69] Ward, J. F. Calculation of nonlinear optical susceptibilities using diagrammetic perturbation theory. *Reviews of Modern Physics* **37**, 1 (1965).

[70] Bjorkholm, J. Optical Second-Harmonic Generation Using a Focused Gaussian Laser Beam. *Physical Review* **142**, 126–136 (1966).

[71] Ranka, J. K., Windeler, R. S. & Stentz, A. J. Visible continuum generation in air–silica microstructure optical fibers with anomalous dispersion at 800 nm. *Optics Letters* **25**, 25 (2000).

[72] Alfano, R. R. & Shapiro, S. L. Emission in the region 4000 to 7000 via four-photon coupling in glass. *Physical Review Letters* **24**, 584–587 (1970).

[73] Hamm, P. *Principles of Nonlinear Optical Spectroscopy : A Practical Approach or : Mukamel for Dummies* (Zurich, 2005), 1 edn.

[74] Mukamel, S. Liouville-Space Pathways and Phase-Space Wavepackets in Femtosecond Spectroscopy (1996).

[75] Yan, Y. J., Fried, L. E. & Mukamel, S. Ultrafast pump-probe spectroscopy: femtosecond dynamics in Liouville space. *The Journal of Physical Chemistry* **93**, 8149–8162 (1989).

[76] Brewer, R. G. & Shoemaker, R. L. Optical Free Induction Decay. *Physical Review A* **6**, 2001–2007 (1972).

[77] Kohles, N., Aechtner, P. & Laubereau, A. The "coherence peak" in time resolved coherent Raman scattering. *Optics Communications* **65**, 391–396 (1987).

[78] Sukharev, M. & Nitzan, A. Numerical studies of the interaction of an atomic sample with the electromagnetic field in two dimensions. *Physical Review A - Atomic, Molecular, and Optical Physics* **84**, 1–10 (2011). 1104.3325.

[79] Loudon, R. *The quantum theory of light* (Oxford University Press, 2000), 3rd edn.

[80] Marx, C. A., Harbola, U. & Mukamel, S. Nonlinear optical spectroscopy of single, few, and many molecules: Nonequilibrium Green's function QED approach. *Physical Review A* **77**, 22110 (2008). 0711.2094.

[81] Gilbert Grynberg, A. A. & Fabre, C. *Introduction to Quantum Optics From the Semi-classical Approach to Quantized Light* (Cambridge University Press, 2010), first edn.

[82] Boyd, R. W. & Mukamel, S. Origin of spectral holes in pump-probe studies of homogeneously broadened lines (1984). arXiv:1011.1669v3.

[83] Louisell, W. H. *Quantum Statistical Properties of Radiation* (John Wiley & Sons Inc, 1973), first edn.

[84] Berne, B. J. & Harp, G. D. On the calculation of time correlation functions. *Adv. Chem. Phys* **17**, 63–227 (1970).

[85] Shen, Y. R. *The Principles of Nonlinear Optics* (John Wiley & Sons, 2002), 1st edn.

[86] Guang S He, S.-H. L. *Physics of Nonlinear Optics* (World Scientific Publishing Company, 2000).

[87] Broglie, L. *Heisenberg's uncertainties and the probabilistic interpretation of wave mechanics* (1990).

[88] Strekalov, D. V. & Leuchs, G. Nonlinear interactions and non-classical light (2017). 1701.01403.

[89] Louisell, W. H., Yariv, A. & Siegman, a. E. Quantum fluctuations and noise in parametric processes. I. *Physical Review* **124**, 1646–1654 (1961).

[90] Mollow, B. R. & Glauber, R. J. Quantum theory of parametric amplification. i. *Physical Review* **160**, 1076–1096 (1967).

[91] Gerry, C. C., Knight, P. L. & Beck, M. *Introductory Quantum Optics.*, vol. 73 (2005).

[92] Wang, Y. K. & Khoo, I. C. On the Wigner-Weisskopf approximation in quantum optics. *Optics Communications* **11**, 323–326 (1974). 9902013.

[93] Ling, A., Lamas-Linares, A. & Kurtsiefer, C. Absolute emission rates of spontaneous parametric down-conversion into single transverse Gaussian modes. *Physical Review A - Atomic, Molecular, and Optical Physics* **77**, 1–7 (2008). 0801.2220.

[94] Crosignani, B. *et al.* Quantum effects in second harmonic generation. *Journal of Physics A: General Physics* **5**, L119–L121 (1972). 9606014.

[95] Petrov, V. Parametric down-conversion devices: The coverage of the mid-infrared spectral range by solid-state laser sources. *Optical Materials* **34**, 536–554 (2012).

[96] Goodman, J. W. *Introduction to Fourier Optics* (Roberts & Company Publishers, 2005), third edn.

[97] Gu, M. *Advanced Optical Imaging Theory*, vol. 75 (1999).

[98] Wilson, T. & Sheppard, C. *Theory and Practice of Scanning Optical Microscopy* (Academic Press, New York, 1987).

[99] Goodman, J. W. *Statistical Optics* (Wiley-Interscience, 2000), first edn.

[100] Hopkins, H. H. On the Diffraction Theory of Optical Images. *Proc. R. Soc. Lond. A* **217**, 408–432 (1953).

[101] Gu, M. *Principles Of Three-Dimensional Imaging In Confocal Microscopes* (World Scientific, 1996).

[102] Diels, J.-C. & Rudolph, W. *Ultrashort Laser Pulse Phenomena* (Academic Press, 2006), second edn.

[103] Kempe, M. & Rudolph, W. Femtosecond pulses in the focal region of lenses. *Physical Review A* **48**, 4721–4729 (1993).

[104] Sheetz, K. E. & Squier, J. Ultrafast optics: Imaging and manipulating biological systems. *Journal of Applied Physics* **105** (2009).

[105] Davidovits, P. & Egger, M. D. Scanning laser microscope. *Nature* **223**, 831 (1969).

[106] Sheppard, C. J. R. & Choudhury, a. Image formation in the scanning microscope. *Opt. Acta* **24**, 1051–1073 (1977).

[107] Welford, W. On the relationship between the modes of image formation in scanning microscopy and conventional microscopy. *J. Microsc.* **96**, 104–107 (1972).

[108] Sheppard, R. & Wilson, T. Image formation in confocal scanning microscopes. *Optik* **55**, 331–342 (1980).

[109] Sheppard, C. J. & Wilson, T. The theory of the direct-view confocal microscope. *Journal of microscopy* **124**, 107–117 (1981).

[110] Wilson, T. Resolution and optical sectioning in the confocal microscope. *Journal of Microscopy* **244**, 113–121 (2011).

[111] Amos, W. B. & White, J. G. How the confocal laser scanning microscope entered biological research. *Biology of the Cell* **95**, 335–342 (2003).

[112] Lemons, R. A. & Quate, C. F. Acoustic microscope - Scanning version. *Applied Physics Letters* **24**, 163–165 (1974).

[113] Sawatari, T. Optical heterodyne scanning microscope. *Applied optics* **12**, 2768–2772 (1973).

[114] Wilson, T. & Hewlett, S. J. J. The Use of Annular Pupil Plane Filters to Tune the Imaging Properties in Confocal Microscopy. *Journal of Modern Optics* **37**, 2025–2046 (1990).

[115] Mertz, J. Nonlinear microscopy: new techniques and applications. *Current opinion in neurobiology* **14**, 610–616 (2004).

[116] Masters, B. R. & So, P. T. *Handbook Of Biomedical Nonlinear Optical Microscopy* (Oxford University Press, 2008).

[117] Masters, B. R. *Confocal microscopy and multiphoton excitation microscopy: the genesis of Live Cell Imaging* (2006).

[118] Meyer, T., Schmitt, M., Dietzek, B. & Popp, J. Accumulating advantages, reducing limitations: Multimodal nonlinear imaging in biomedical sciences - The synergy of multiple contrast mechanisms. *Journal of Biophotonics* **6**, 887–904 (2013).

[119] Garrett, N. L., Lalatsa, A., Uchegbu, I., Schätzlein, A. & Moger, J. Exploring uptake mechanisms of oral nanomedicines using multimodal nonlinear optical microscopy. *Journal of Biophotonics* **5**, 458–468 (2012).

[120] Wilson, J. W. *et al.* Imaging microscopic pigment chemistry in conjunctival melanocytic lesions using pump-probe laser microscopy. *Investigative ophthalmology & visual science* **54**, 6867–6876 (2013).

[121] Fu, D., Matthews, T. E., Ye, T., Piletic, I. R. & Warren, W. S. Label-free in vivo optical imaging of microvasculature and oxygenation level. *Journal of Biomedical Optics* **13**, 40503 (2008).

[122] Matthews, T. E., Piletic, I. R., Selim, M. A., Simpson, M. J. & Warren, W. S. NIH Public Access **3**, 1–19 (2012).

[123] Fu, D., Matthews, T. E., Ye, T., Yurtserver, G. & Warren, W. S. Two-photon absorption imaging of hemoglobin. *Conference on Lasers and Electro-Optics, 2007, CLEO 2007* 1–2 (2007).

[124] Fu, D., Ye, T., Matthews, T. E., Yurtsever, G. & Warren, W. S. Two-color, two-photon, and excited-state absorption microscopy. *Journal of Biomedical Optics* **12**, 54004 (2007).

[125] Wang, B. G., König, K. & Halbhuber, K. J. Two-photon microscopy of deep intravital tissues and its merits in clinical research. *Journal of Microscopy* **238**, 1–20 (2010).

[126] Hoover, E. E. & Squier, J. A. Advances in multiphoton microscopy. *Nature Photonics* **7**, 93 – 101 (2013).

[127] Evans, C. L. & Xie, X. S. Coherent Anti-Stokes Raman Scattering Microscopy: Chemical Imaging for Biology and Medicine. *Annual Review of Analytical Chemistry* **1**, 883–909 (2008).

[128] Carriles, R. *et al.* Invited Review Article: Imaging techniques for harmonic and multiphoton absorption fluorescence microscopy. *Review of Scientific Instruments* **80**, 1–23 (2009).

[129] Rego, E. H. *et al.* Nonlinear structured-illumination microscopy with a photoswitchable protein reveals cellular structures at 50-nm resolution. *Proceedings of the National Academy of Sciences of the United States of America* **109**, E135———43 (2012).

[130] Svoboda, K. & Yasuda, R. Principles of Two-Photon Excitation Microscopy and Its Applications to Neuroscience. *Neuron* **50**, 823–839 (2006).

[131] Davydova, D., de la Cadena, A., Akimov, D. & Dietzek, B. Transient absorption microscopy: Advances in chemical imaging of photoinduced dynamics. *Laser and Photonics Reviews* **10**, 62–81 (2016).

[132] Gannaway, J. N. & Sheppard, C. J. R. Second-harmonic imaging in the scanning optical microscope. *Optical and Quantum Electronics* **10**, 435–439 (1978).

[133] Denk, W., Strickler, J. H. & Webb, W. W. Two-photon laser scanning fluorescence microscopy. *Science (New York, N.Y.)* **248**, 73–6 (1990). URL http://www.ncbi.nlm.nih.gov/pubmed/2321027. arXiv:1011.1669v3.

[134] Denk, W., Strickler, J. P. & Webb, W. W. Two-photon laser microscopy (1991).

[135] Seo, M. *et al.* Ultrafast optical wide field microscopy. *Optics Express* **21**, 8763–8772 (2013).

[136] Massaro, E. S., Hill, A. H. & Grumstrup, E. M. Super-Resolution Structured Pump-Probe Microscopy. *ACS Photonics* **3**, 501–506 (2016).

[137] Jahng, J. *et al.* Ultrafast pump-probe force microscopy with nanoscale resolution. *Applied Physics Letters* **106** (2015).

[138] Gu, M. & Sheppard, C. J. R. Comparison of three-dimensional imaging properties between two-photon and single-photon fluorescence microscopy. *Journal of Microscopy* **177**, 128–137 (1995).

[139] Sheppard, C. J. R. J. R. & Gu, M. Image formation in two-photon fluorescence microcopy. *Optik* **86** (1990).

[140] Masters, B. & So, P. Confocal microscopy and multi-photon excitation microscopy of human skin in vivo. *Optics express* **8**, 2–10 (2001). URL http://www.ncbi.nlm.nih.gov/pubmed/19417779.

[141] Masters, B. R., So, P. T. & Gratton, E. Multiphoton excitation fluorescence microscopy and spectroscopy of in vivo human skin. *Biophysical journal* **72**, 2405 (1997).

[142] Masters, B. R. & So, P. T. C. C. Multi-photon Excitation Microscopy and Confocal Microscopy Imaging of In Vivo Human Skin: A Comparison. *Microscopy and Microanalysis* **5**, 282–289 (2003). URL http://journals.cambridge.org/abstract_S1431927699990311.

[143] Zipfel, W. R., Williams, R. M. & Webb, W. W. Nonlinear magic: multiphoton microscopy in the biosciences. *Nature biotechnology* **21**, 1369–1377 (2003).

[144] Fukutake, N. Resolution properties of nonlinear. *J. Opt. Soc. Am. A* **27**, 1701–1707 (2010).

[145] Fukutake, N. Coherent transfer function of Fourier transform spectral interferometric coherent anti-Stokes Raman scattering microscopy. *Journal of the Optical Society of America a-Optics Image Science and Vision* **28**, 1689–1694 (2011).

[146] Fukutake, N. Comparison of image-formation properties of coherent nonlinear microscopy by means of double-sided Feynman diagrams. *Journal of the Optical Society of America B-Optical Physics* **30**, 2665–2675 (2013).

[147] Deitche, J., Kempe, M. & Rudolph, W. Resolution in nonlinear laser scanning microscopy (1994).

[148] Isobe, K., Watanabe, W. & Itoh, K. *Functional Imaging by Controlled Nonlinear Optical Phenomena* (John Wiley & Sons, Inc, 2013).

[149] Richards, B. & Wolf, E. Electromagnetic Diffraction in Optical Systems. II. Structure of the Image Field in an Aplanatic System. *Proceedings of the Royal Society A: Mathematical, Physical and Engineering Sciences* **253**, 358–379 (1959).

[150] Davydova, D. *et al.* Ultrafast transient absorption microscopy: Study of excited state dynamics in PtOEP crystals. *Chemical Physics* **464**, 69–77 (2016).

[151] Grancini, G. *et al.* Transient Absorption Imaging of P3HT : PCBM Photovoltaic Blend. *The Journal of Physical Chemistry Letters* **2**, 1099–1105 (2011).

[152] De la Cadena, A. *et al.* Ultrafast in cellulo photoinduced dynamics processes of the paradigm molecular light switch [Ru(bpy)2dppz]2+. *Scientific Reports* **6**, 33547 (2016).

[153] Matthews, T. E., Piletic, I. R., Selim, M. A., Simpson, M. J. & Warren, W. S. Pump-Probe Imaging Differentiates Melanoma from Melanocytic Nevi. *Science Translational Medicine* **3** (2011).

[154] Thompson, A. *et al.* Dual-wavelength pump-probe microscopy analysis of melanin composition. *Scientific Reports* **6**, 36871 (2016). URL http://www.nature.com/articles/srep36871.

[155] Fischer, M. C., Wilson, J. W., Robles, F. E. & Warren, W. S. Invited Review Article: Pump-probe microscopy. *Review of Scientific Instruments* **87** (2016).

[156] Sadler, P. J. Inorganic Chemistry and Drug Design. *Advances in Inorganic Chemistry* **36**, 1–48 (1991).

[157] Gill, M. R. *et al.* A ruthenium(II) polypyridyl complex for direct imaging of DNA structure in living cells. *Nature chemistry* **1**, 662–667 (2009).

[158] Leung, S. K., Kwok, K. Y., Zhang, K. Y. & Lo, K. K. W. Design of luminescent biotinylation reagents derived from cyclometalated iridium(III) and rhodium(III) bis(pyridylbenzaldehyde) complexes. *Inorganic Chemistry* **49**, 4984–4995 (2010).

[159] Rajendiran, V., Palaniandavar, M., Periasamy, V. S. & Akbarsha, M. A. [Ru(phen)2(dppz)]2+ as an efficient optical probe for staining nuclear components. *Journal of Inorganic Biochemistry* **104**, 217–220 (2010).

[160] Jiménez-Hernández, M. E., Orellana, G., Montero, F. & Portolés, M. T. A Ruthenium Probe for Cell Viability Measurement Using Flow Cytometry, Confocal Microscopy and Time-resolved Luminescence ¶. *Photochemistry and Photobiology* **72**, 28–34 (2007).

[161] Fernández-Moreira, V., Thorp-Greenwood, F. L. & Coogan, M. P. Application of d6 transition metal complexes in fluorescence cell imaging. *Chem. Commun.* **46**, 186–202 (2010). URL http://xlink.rsc.org/?DOI=B917757D.

[162] Howerton, B. S., Heidary, D. K. & Glazer, E. C. Strained Ruthenium Complexes Are Potent Light-Activated Anticancer Agents. *Journal of the American Chemical Society* **134**, 8324–8327 (2012).

[163] Wang, J. Q., Zhang, P. Y., Ji, L. N. & Chao, H. A ruthenium(II) complex inhibits tumor growth in vivo with fewer side-effects compared with cisplatin. *Journal of Inorganic Biochemistry* **146**, 89–96 (2015).

[164] Johnstone, T. C., Park, G. Y. & Lippard, S. J. Understanding and improving platinum anticancer drugs - Phenanthriplatin. *Anticancer Research* **34**, 471–476 (2014). NIHMS150003.

[165] Guo, X. Q., Castellano, F. N., Li, L. & Lakowicz, J. R. A long-lifetime Ru(II) metal-ligand complex as a membrane probe. *Biophysical chemistry* **71**, 51–62 (1998).

[166] Jain, A., Xu, W., Demas, J. N. & DeGraff, B. a. Binding of Luminescent Ruthenium(II) Molecular Probes to Vesicles. *Inorganic Chemistry* **37**, 1876–1879 (1998).

[167] Friedman, A., Chambron, JC Turro, N. & Barton, J. A molecular light switch for DNA: Ru (bpy) 2 (dppz) 2+. *Journal of the American Chemical Society* **112**, 4960–4962 (1990).

[168] Gao, F., Chao, H. & Ji, L. N. DNA binding, photocleavage, and topoisomerase inhibition of functionalized ruthenium(II)-polypyridine complexes. *Chemistry and Biodiversity* **5**, 1962–1979 (2008).

[169] Chambron, J.-C. & Sauvage, J.-P. Ru (bipy)2dppz2+ : a highly sensitive luminescent probe for micellar sodium dodecyl sulfate solutions (1991).

[170] Hartshorn, R. M. & Barton, J. K. Novel dipyridophenazine complexes of ruthenium(II): exploring luminescent reporters of DNA. *Journal of the American Chemical Society* **114**, 5919–5925 (1992).

[171] Wragg, A. *et al.* Tuning the Cellular Uptake Properties of Luminescent Heterobimetallic Iridium(III)-Ruthenium(II) DNA Imaging Probes. *Chemistry - A European Journal* **20**, 14004–14011 (2014).

[172] Fees, J., Ketterle, M., Klein, A., Fiedler, J. & Kaim, W. Electrochemical, spectroscopic and EPR study of transition metal complexes of dipyrido[3,2-a : 2,3-c]phenazine. *Journal of the Chemical Society-Dalton Transactions* 2595–2599 (1999).

[173] Zeglis, B. M., Pierre, V. C. & Barton, J. K. Metallo-intercalators and metallo-insertors. *Chemical Communications* **29**, 4565 (2007).

[174] Schatzschneider, U. *et al.* Cellular uptake, cytotoxicity, and metabolic profiling of human cancer cells treated with ruthenium(II) polypyridyl complexes [Ru(bpy)2(N–N)]Cl2 with N–N=bpy, phen, dpq, dppz, and dppn. *ChemMedChem* **3**, 1104–1109 (2008).

[175] Amoroso, A. J. *et al.* 3-Chloromethylpyridyl bipyridine fac-tricarbonyl rhenium: A thiol-reactive luminophore for fluorescence microscopy accumulates in mitochondria. *New Journal of Chemistry* **32**, 1097–1102 (2008).

[176] Lo, K. K. W., Louie, M. W., Sze, K. S. & Lau, J. S. Y. Rhenium(I) polypyridine biotin isothiocyanate complexes as the first luminescent biotinylation reagents: Synthesis, photophysical properties, biological labeling, cytotoxicity, and imaging studies. *Inorganic Chemistry* **47**, 602–611 (2008).

[177] Byrne, A. *et al.* Osmium(II) polypyridyl polyarginine conjugate as a probe for live cell imaging; a comparison of uptake, localization and cytotoxicity with its ruthenium(II) analogue. *Dalton Trans.* **44**, 14323–14332 (2015).

[178] Zhang, K. Y. *et al.* Structure, photophysical and electrochemical properties, biomolecular interactions, and intracellular uptake of luminescent cyclometalated iridium(III) dipyridoquinoxaline complexes. *Inorganic Chemistry* **49**, 2530–2540 (2010).

[179] Zhu, B.-Z., Chao, X.-J., Huang, C.-H. & Li, Y. Delivering the cell-impermeable DNA 'light-switching' Ru(ii) complexes preferentially into live-cell nucleus via an unprecedented ion-pairing method. *Chem. Sci.* **7**, 4016–4023 (2016). URL http://xlink.rsc.org/?DOI=C5SC03796D.

[180] Cheng, C.-C., Lee, W.-L., Su, J.-G. & Liu, C.-L. Covalent Interaction of Ru(terpy)(tmephen)Cl + with DNA: A Potential Ruthenium-Based Anticancer Drug. *Journal of the Chinese Chemical Society* **47**, 213–220 (2000).

[181] Puckett, C. A. & Barton, J. K. Methods to explore cellular uptake of ruthenium complexes. *Journal of the American Chemical Society* **129**, 46–47 (2007).

[182] Stephenson, M. *et al.* Ru(II) dyads derived from 2-(1-pyrenyl)-1H-imidazo[4,5-f][1,10]phenanthroline: Versatile photosensitizers for photodynamic applications. *Journal of Physical Chemistry A* **118**, 10507–10521 (2014).

[183] Pierroz, V. *et al.* Molecular and cellular characterization of the biological effects of ruthenium(II) complexes incorporating 2-pyridyl-2-pyrimidine-4-carboxylic acid. *Journal of the American Chemical Society* **134**, 20376–20387 (2012).

[184] Neugebauer, U. *et al.* Ruthenium polypyridyl peptide conjugates: membrane permeable probes for cellular imaging. *Chemical communications* **2**, 5307–5309 (2008).

[185] Yu, M. *et al.* Cationic iridium(III) complexes for phosphorescence staining in the cytoplasm of living cells. *Chemical communications (Cambridge, England)* 2115–2117 (2008).

[186] Lo, K. K. W., Lee, P. K. & Lau, J. S. Y. Synthesis, characterization, and properties of luminescent organoiridium(III) polypyridine complexes appended with an alkyl chain and their interactions with lipid bilayers, surfactants, and living cells. *Organometallics* **27**, 2998–3006 (2008).

[187] Wang, J. Q. *et al.* Mitochondria are the primary target in the induction of apoptosis by chiral ruthenium(II) polypyridyl complexes in cancer cells. *Journal of Biological Inorganic Chemistry* **19**, 335–348 (2014).

[188] Gill, M. R. *et al.* A ruthenium polypyridyl intercalator stalls DNA replication forks, radiosensitizes human cancer cells and is enhanced by Chk1 inhibition. *Scientific Reports* **6**, 31973 (2016). URL http://www.nature.com/articles/srep31973.

[189] Hotze, A. C. G. *et al.* Characterization by NMR Spectroscopy, X-ray Analysis and Cytotoxic Activity of the Ruthenium(II) Compounds [RuL3](PF6)2(L = 2-Phenylazopyridine or o-Tolylazopyridine) and [RuL'2L"](PF6)2(L', L" = 2-Phenylazopyridine, 2,2'-Bipyridine). *European Journal of Inorganic Chemistry* 2648–2657 (2005).

[190] Balzani, V., Credi, A. & Venturi, M. Photochemistry and photophysics of coordination compounds. An extended view. *Coordination Chemistry Reviews* **171**, 3–16 (1998).

[191] Puntoriero, F., Nastasi, F., Galletta, M. & Campagna, S. Photophysics and Photochemistry of Non-Carbonyl-Containing Coordination and Organometallic Compounds. In *Comprehensive Inorganic Chemistry II (Second Edition): From Elements to Applications*, vol. 8, 255–337 (2013).

[192] Balzani, V., Juris, A., Venturi, M., Campagna, S. & Serroni, S. Luminescent and Redox-Active Polynuclear Transition Metal Complexes ¡sup¿†¡/sup¿. *Chemical Reviews* **96**, 759–834 (1996). URL http://pubs.acs.org/doi/abs/10.1021/cr941154y. 0402594v3.

[193] Crosby, G. A. Spectroscopic investigations of excited states of transition-metal complexes. *Accounts of Chemical Research* **8**, 231–238 (1975).

[194] Kasha, M. Characterization of electronic transitions in complex molecules. *Discussions of the Faraday Society* **9**, 14 (1950).

[195] Rohatgi-Mukherjee, K. Fundamentals of photochemistry 371 (1978).

[196] Salassa, L. *et al.* Ligand-Selective Photodissociation from [Ru(bpy)(4AP) 4] 2+ : a Spectroscopic and Computational Study. *Inorganic Chemistry* **48**, 1469–1481 (2009). URL http://pubs.acs.org/doi/abs/10.1021/ic8015436.

[197] Jenkins, Y., Friedman, a. E., Turro, N. J. & Barton, J. K. Characterization of dipyridophenazine complexes of ruthenium(II): The light switch effect as a function of nucleic acid sequence and conformation. *Biochemistry* **31**, 10809–10816 (1992).

[198] Klessinger, M. & Michl, J. *Excited states and photochemistry of organic molecules*, vol. 53 (John Wiley & Sons, 1995), 1 edn.

[199] Macomber, R. S., Pinhas, A. R., Orchin, M. & Wilson, R. M. *The Vocabulary and Concepts of Organic Chemistry* (John Wiley & Sons, 2005), second edn.

[200] Olson, E. J. C. *et al.* First Observation of the Key Intermediate in the " Light-Switch " Mechanism of [Ru (phen) 2 dppz] 2 +. *Journal of the American Chemical Society* **7863**, 11458–11467 (1997).

[201] Damrauer, N. H. *et al.* Femtosecond Dynamics of Excited-State Evolution in [Ru(bpy)3]2+. *Science* **275**, 54–57 (1997).

[202] Turro, N. J. The Triplet State. *Journal of Chemical Education* **46**, 2–6 (1966).

[203] Atkins, P. W. & Friedman, R. S. *Molecular Quantum Mechanics* (oxford university press, 2010), fifth edn.

[204] Nair, R. B., Cullum, B. M. & Murphy, C. J. Optical Properties of [Ru(phen)(2)dppz](2+) as a Function of Nonaqueous Environment. *Inorganic chemistry* **36**, 962–965 (1997).

[205] Cossins, B. P., Jacobson, M. P. & Guallar, V. A new view of the bacterial cytosol environment. *PLoS Computational Biology* **7** (2011).

[206] Fumagalli, L., Esteban-Ferrer, D., Cuervo, A., Carrascosa, J. L. & Gomila, G. Label-free identification of single dielectric nanoparticles and viruses with ultraweak polarization forces. *Nature materials* **11**, 808–16 (2012).

[207] Hiort, C., Lincoln, P. & Norden, B. DNA binding of .DELTA.- and .LAMBDA.-[Ru(phen)2DPPZ]2+. Tech. Rep. 1395 (1998).

[208] De la Cadena, A. *et al.* Intermolecular exciton-exciton annihilation in phospholipid vesicles doped with [Ru(bpy)2dppz]2+. *Chemical Physics Letters* **644**, 56–61 (2016).

[209] Horvath, R. & Gordon, K. C. Excited state vibrational spectroscopy of metal complexes of dipyrido[3,2-a:2,3-c]phenazine (2011).

[210] Klein, A., Kaim, W., Waldhor, E. & Hausen, H.-d. Different orbital occupation by an added single electron in 1,10-phenanthroline and its 3,4,7,8-tetramethyl derivative. Evidence from electron paramagnetic resonance spectroscopy of the anion radicals and of their dimesitylplatinum(II) complexes. X-Ray mo. *Journal of the Chemical Society, Perkin Transactions 2* 2121 (1995).

[211] Fees, J., Kaim, W., Matheb, M. W., Krej, M. & Mi, S. Electronic structure of the ”molecular light switch” bis(bipyridine)dipyrido[3,2-a:2’,3’-c]phenazineruthenium(2+). Cyclic voltammetric, UV/visible and EPR/ENDOR study of multiply reduced complexes and ligands. *Inorganic Chemistry* **32**, 166–174 (1993).

[212] Bixon, M., Jortner, J., Cortes, J., Heitele, H. & Michel-Beyerle, M. E. Energy Gap Law for Nonradiative and Radiative Charge Transfer in Isolated and in Solvated Supermolecules. *The Journal of Physical Chemistry* **98**, 7289–7299 (1994).

[213] Brennaman, M. K. *et al.* Turning the [Ru(bpy) 2 dppz] 2+ Light-Switch On and Off with Temperature. *Journal of the American Chemical Society* **124**, 15094–15098 (2002).

[214] Brennaman, M. K., Meyer, T. J. & Papanikolas, J. M. [Ru(bpy)2dppz]2+ Light-switch mechanism in protic solvents as studied through temperature-dependent lifetime measurements. *Journal of Physical Chemistry A* **108**, 9938–9944 (2004).

[215] Tanaka, M., Schneck, E., Yoshikawa, H. Y. & Rossetti, F. F. Physical chemistry of biological interfaces: Generic and specific roles of soft interlayers (2011).

[216] Alberts, B. *et al. Molecular Biology of the Cell* (Garland Science, New York, 2002), 4th. edn.

[217] Lodish, H. *et al. Molecular Cell Biology* (W.H.Freeman, 2007), 6th edn.

[218] Ketterer, B., Neumcke, B. & Läuger, P. Transport mechanism of hydrophobic ions through lipid bilayer membranes. *The Journal of Membrane Biology* **5**, 225–245 (1971).

[219] Andersen, O. S. & Fuchs, M. Potential energy barriers to ion transport within lipid bilayers: Studies with tetraphenylborate. *Biophysical journal* **15**, 795–830 (1975).

[220] Ehrenberg, B., Montana, V., Wei, M. D., Wuskell, J. P. & Loew, L. M. Membrane potential can be determined in individual cells from the nernstian distribution of cationic dyes. *Biophysical journal* **53**, 785–94 (1988).

[221] Chen, L. B. Mitochondrial membrane potential in living cells. *Annual Review of Cell Biology* **4**, 155–81 (1988).

[222] McLaughlin, S. Electrostatic Potentials at Membrane-Solution Interfaces. *Current Topics in Membranes and Transport* **9**, 71–144 (1977).

[223] Hodgkin, A., Huxley, A. & Katz, B. Measurement of current-voltage relations in the membrane of the giant axon of Loligo. *Journal of Physiology* **116**, 424–448 (1951).

[224] Hodgkin, A. L. & Huxley, A. F. The dual effect of membrane potential on sodium conductance in the giant axon of Loligo. *The Journal of Physiology* **116**, 497–506 (1952).

[225] Puckett, C. A. & Barton, J. K. Mechanism of cellular uptake of a ruthenium polypyridyl complex. *Biochemistry* **47**, 11711–11716 (2008). NIHMS150003.

[226] Önfelt, B., Göstring, L., Lincoln, P., Nordén, B. & Önfelt, A. {C}ell studies of the {DNA} bis-intercalator {Δ}-{Δ} \left[\mu-{C}4(cpdppz)_2-(phen)_4{R}u_2\right]^{4+}: toxic effects and properties as a light emitting {DNA} probe in {V}79 {C}hinese hamster cells. *Mutagenesis* **17**, 317–320 (2002).

[227] O'Brien, J., Wilson, I., Orton, T. & Pognan, F. Investigation of the Alamar Blue (resazurin) fluorescent dye for the assessment of mammalian cell cytotoxicity. *European Journal of Biochemistry* **267**, 5421–5426 (2000).

[228] Limpert, J. *et al.* High-power femtosecond Yb-doped fiber amplifier. *Optics express* **10**, 628–38 (2002).

[229] Paschotta, R., Nilsson, J., Tropper, A. C. & Hanna, D. C. Ytterbium-doped fiber amplifiers. *IEEE Journal of Quantum Electronics* **33**, 1049–1056 (1997).

[230] Polli, D. *et al.* Broadband pump-probe spectroscopy with sub-10-fs resolution for probing ultrafast internal conversion and coherent phonons in carotenoids. *Chemical Physics* **350**, 45–55 (2008).

[231] Blume, R. J. "Boxcar" integrator with long holding times. *Review of Scientific Instruments* **32**, 1016–1018 (1961).

[232] Collier, J. L., Goddard, B. J., Goode, D. C., Marka, S. & Telle, H. H. A low-cost gated integrator boxcar averager. *Measurement Science and Technology* **7**, 1204–1211 (1996).

[233] Swain, D. W. Boxcar integrator attachment for oscilloscopes. *Review of Scientific Instruments* **41**, 545–547 (1970).

[234] Ware, D. & Mansfield, P. High stability "boxcar" integrator for fast NMR transients in solids. *Review of Scientific Instruments* **37**, 1167–1171 (1966).

[235] Ferrari, G. & Sampietro, M. Wide bandwidth transimpedance amplifier for extremely high sensitivity continuous measurements. *Review of Scientific Instruments* **78** (2007).

[236] Reichardt, C. *et al.* Photophysics of Ru(II) Dyads Derived from Pyrenyl-Substitued Imidazo[4,5-f][1,10]phenanthroline Ligands. *Journal of Physical Chemistry A* **119**, 3986–3994 (2015).

Summary

This thesis presents the construction and characterization of a microscope based on pump-probe spectroscopy and its application to observe and study the evolution of photoinduced reactions. As compared to the typical pump-probe systems reported in the literature, which utilizes either 1 kHz or 80 MHz pulse-trains, the developed microscope was fed by pump pulse-trains at 125 kHz and probe pulse-trains at 250 kHz repetition rates in order to perform transient absorption microscopy (TAM). The use of such intermediate repetition rate reduces the unnecessary exposure of the sample to input field leading to risk of photo-induced damage and it also relaxes the use of lock-in detection, an unavoidable element for any MHz system, which increases the cost and complexity of the system. This gives the possibility to perform microspectroscopic studies of micro-structures with minimal photo-induced damage, a property that is especially important to the study of biological samples, without the incorporation of lock-in detection. Therefore, the developed TAM system by itself is a proof of concept.

The special demands from the laser source including low pulse to pulse fluctuations, high energy per pulse, as well as moderate repetition rates, were fulfilled by a tailor-made dual-channel Ytterbium-fiber based femtosecond laser source. The two outputs of the Ytterbium laser provide pulse-trains at 125 and 250 kHz respectively but each centered at 1030 nm wavelength. These two channels separately focused on a Sahpphire and a YAG crystal respectively for white light generation. Then these two supercontinuum were utilized to separately and synchronously seed two optical parametric amplifiers (OPAs) operating at 125 and 250 kHz respectively. The two OPA outputs served as the pump and probe pulse-trains for the TAM.

The conclusions described in the literature derived from photophysical studies in model solvents indicate that the photophysics of Ru(II)-based complexes is highly affected by the their surroundings. However, the ultrafast photophysics of Ru(II) based molecular markers or photodrugs has never been studied *in cellulo*. The TAM system was employed to study the ultrafast photoinduced-dynamics through localized pump-probe spectroscopy and to get the distribution of such Ru-based drugs within a cell. The behavior of the molecular

system of interest *in cellulo* was investigated with diffraction-limited resolution and with the additional facility to record transient absorption contrast images at specific time intervals after photoexcitation. This information in fact gives a glimpse on how the studied drug would behave in the targeted cellular compartment. The implemented microscope enables inherently the advantage of the TAM technique over emission based microscopy to visualize even non-emissive species. It is worth mentioning that before performing experiments on biological samples, the TAM system was tested and validated using reference samples such as fluorescent polystyrene beads and platinum octaethylporphyrin (PtOEP) crystals embedded into a polymer matrix. With this characterization, the microscope was employed to study the ultrafast dynamics as well as the location of Ru-polyprydine based drugs in eukaryotic cells. The main interest in this research was to determine the influence of the heterogeneous cellular environment on the excited states of the investigated complexes rather than the study of the effects induced by those excited states on the cells. In other words: the cytotoxic effects of the drugs were not taken into consideration. In fact, they were neglected since all the experiments involving dosed cells reported in this thesis were carried out using drug-concentrations that lie below the corresponding half maximal inhibitory concentration (IC_{50}) of the drug. Additionally, all of the cells employed on this research were fixated.

The benchmark molecule $[Ru(bpy)_2(dppz)]^{2+}$ was used for dosing the cells to investigate the influences of the cellular environment on Ru-based drugs. This particular molecule was chosen because it binds avidly to DNA, shows low cytotoxicity and has a long lived strong red-shifted emission. The $[Ru(bpy)_2(dppz)]^{2+}$ also acts like a "molecular light-switch" due to its extreme sensitiveness to the solvent. In fact, it displays solvatochromatism and its emission can even completely be deactivated. Several scientific groups have investigated $[Ru(bpy)_2(dppz)]^{2+}$ and related Ru(II)-polypridine complexes. This has led to the accumulation of a broad database including its photophysical and electrochemical properties. Also there has been studies on living and fixed cells dosed with this molecule, giving rise to the debate whether it is uptaken by living cells or not. Based on such a priori knowledge, we conceived and performed key spectroscopic experiments to characterize the same molecule in the environments which resemble the interior of an eukaryotic cell using solutions that mimic the nuclei, the cellular membrane and the cytosol. We used the $[Ru(bpy)_2(dppz)]^{2+}$ molecule along with DAPI (a standard nuclei marker) to dosed HepG2 cells. It was observed, through emission-based microscopy, a stronger luminescence signal with respect to DAPI both arising from the nuclei of viable and fixed cells. This information was utilized to cross-validate the transient-absorption imaging. It is worth to mention that yet, as to best of my knowledge, there is no such report on pump-probe microspectroscopic study of cellular organisms dosed with metal complexes.

The work above described spurred the TAM study of another set of molecules which were conceived, designed and synthesized specifically to serve as either lumophore or photo-triggered drug. These sets of molecules including $[(bpy)_2Ru(tpphz)Ru(bpy)_2]^{4+}$, $[Ru(bpy)_2ippy]^{2+}$, and Ruthenium(II)-Arene-Curcumin based dyes, were investigated separately following the same methodology as performed for the $[Ru(bpy)_2(dppz)]^{2+}$. These molecular sets exhibited a higher uptake respective to the $[Ru(bpy)_2(dppz)]^{2+}$, attributed to their more lipophilic ligands, providing promising results. An important finding in this work was the dependence of the photoinduced dynamics shown by the molecular system under study as function of the occupied cellular compartment. Thus, the TAM concept profiles itself as a powerful tool with potential for the research and industry of pharmaceutics.

The immediate application of the TAM is the study of well established and characterized cellular lumophores *in cellulo*, followed by the study of non-emissive molecular systems conceived to destroy pathogens, extending the research to other metal complexes or organic-based drugs. In addition, the TAM opens-up the possibility to increase the understanding of the action mechanisms of drugs in clinical trials or drugs routinely employed nowadays in therapy. In the realm of physical optics, the TAM can be employed to determine, experimentally, the optical resolution of the nonlinear microscope, as well as its improvement by merging the non-linear technique with super resolution imaging.

Zusammenfassung

In der vorliegenden Arbeit wurde die Konstruktion, Wirkungsweise und Anwendung eines mikroskopgestützten Pump-Probe Spektroskops Mikroskops sowie dessen Einsatz zu Lokalisierung und Beobachtung photoneninduzierter Reaktionen beschrieben. Sie soll sowohl als Einführung in die Pump-Probe Mikroskopie dienen als auch die Möglichkeiten dieser Technik herausstellen, welche Wissenschaftlern neue Sichtweisen auf ultraschnelle photonenindizierte Prozesse sowie Informationen zur Verteilung von medizinischen Wirkstoffen innerhalb einer Zelle liefern könnten. Dies kann ein Hinweis darauf liefern, wie sich ein untersuchtes Medikament in der Zelle bzw. des jeweiligen Zellbestandteils verhält. Ein solches mikrospektroskopisches Werkzeug ermöglicht nun die Charakterisierung von ausgewählten Molek ülen in cellulo bezüglich ihrer photo-physikalischen Eigenschaften. Es wurde gezeigt, dass durch die spezifischen Eigenschaften der Pump-Probe Mikroskopie die Möglichkeit besteht die zeitliche Entwicklung von photoaktivierter Stoffe mit beugungsbegrenzter Auflösung zu untersuchen.

Das gebaute und beschriebene übergangsabsorbtionsmikroskop Transiente-Absorptions-Mikroskop (TAM, transient absorption microscope) wurde mit neuen Laserparametern konstruiert. Die Wiederholungsrate der (zwei-Kanal) Lichtquelle des übergangsabsorbtionsmikroskops Pump-Probe-Mikroskops weicht grundlegend von denen ab, welche in den üblichen Systemen in der Literatur beschrieben werden. Diese Experimente wurden mit gepulsten Lasern, welche mit 1 kHz oder 80 MHz oszillieren Repetitionsrate arbeiten, betrieben. Der größte Nachteil eines Systems mit MHz Wiederholrate ist die Notwendigkeit des Einsatzes von schnellen Lock-in Verstärkern welche die Kosten und Komplexität des Aufbaus erhöhen können. Die Anforderungen an ein übergangsabsorptionsmikroskop Pump-Probe-Mikroskop wie Puls zu Puls Fluktuationen, Pulsenergie und Wiederholrate, wurden durch den Einsatz eines maßgefertigten Femtosekunden Ytterbium-Faserlasers. Diese Lichtquelle liefert zwei gepulste Strahlen mit 250 kHz bzw. 125 kHz Wiederholrate. Als zentrale Wellenlänge wurde für beide Kanäle λ=1030 nm gewählt, was einen geeigneten Spektralbereich für die Erzeugung von nicht-linearen optischen Effekten darstellt, welcher verstellbare Laserquelle für Pump-Probe Pulse genutzt wird. Die Wiederholraten beider Strahlen nehmen Werte

zwischen denen welche in der Literatur für solche Systeme gefunden werden können. Sie ermöglichen hohe Pulsenergien bei einer (relativ) hohen Anzahl an Pulsen pro Sekunde, wodurch lange Belichtungszeiten der Proben mit Laserstrahlung sowie der Einsatz von schnellen Lock-in Verstärkern vermieden wird. Dadurch wurde gezeigt, dass die Umsetzung des hier vorgestellten Setups mikrospektroskopische Studien von Mikrostrukturen mit minimalem photo-induziertem Schaden, eine Eigenschaft die insbesondere bei der Untersuchung von biologischen Proben von großer Bedeutung ist, und ohne dem Einsatz von schnellen Lock-in Verstärkern ermöglicht. Demzufolge stellt das System ein Machbarkeitsbeweis dar.

Die wichtigsten Methoden und die dafür benötigten Komponenten zur Messung der experimentellen Daten, wurden ebenfalls beschrieben. Eine wesentliche Komponente desübergangsabsorbtionsmikroskop (TAM) ist die Lichtquelle. Wegen der spezifischen Eigenschaften des Pump-Probe Signals, es wird durch heterodyne Detektion gemessen, besteht die Notwendigkeit eine stabile und zuverlässige Puls zu Puls Fluktuation (≤ 5 %). Um eine spektral durchstimmbare Lichtquelle zu ermöglichen, wurde in Zuge der Experimente dieser Arbeit, ein für die Pump-Probe Spektroskopie für jeden Strahl benötigter OPA gebaut. Sowohl Steady-State Emissions-Spektroskopie als auch Bildgebung wurde genutzt um die jeweiligen Emissionspeaks und deren Lage in eukaryotischen Zellen zu bestimmen. Es wurde UV-VIS Steady-State Absorbtions-Spektroskopie genutzt um zu untersuchen welche elektronischen übergänge in den Pump-Probe Spektroskopie Experimenten angeregt wurden. Als Referenzmessung zur Validierung der jeweiligen mikrospektroskopischen Experimente wurden Standard Femtosekunden Pump-Probe Experimente, z.B. solche in denen die Probe aus einer Lösung des untersuchten Molekülsystems bestand. Deshalb enthält die vorliegende Arbeit einen Abschnitt über Optik, Laser Physik, nicht-lineare Optik, Biophysik, Zellkulturen und physikalische Chemie. Erwähnenswert ist, dass vor den Experimenten an biologischen Proben dasübergangsabsorbtionsmikroskop, durch die Messung von Referenzproben wie fluoreszente Polystyrol Kugeln und Platin octaethylporhyrin (PtOEP) Kristalle in einer Polymermatrix, kalibriert und getestet wurde; beide Proben besitzen mikroskopische Dimensionen und haben eine emissive Natur. Die Experimente in dieser Arbeit waren hauptsächlich verbunden mit der Untersuchung von Ruthenium(II)-Komplexen innerhalb eukaryotischer Zellen. Es sollte hervorgehoben werden, dass der wichtigste Punkt dieser Arbeit war eher den Einfluss der heterogenen Zellumgebung auf die angeregten Zustände der untersuchten Komplexe zu erforschen als der induzierten Effekte dieser angeregten Zustände auf die Zellen. In anderen Worten: die zellschädigenden Effekte der Medikamente wurden nicht berücksichtigt und wurden vernachlässigt, da alle Experimente behandelte Zellen mit Wirkstoffkonzentrationen unterhalb der mittleren inhibitorischen Konzentration (IC50) durchgeführt wurden. Zusätzlich wurden alle in dieser Arbeit genutzten Zellen fixiert.

Als Richt-gut untersuchtes molekulares Modell Molekül zur Charakterisierung und Abschätzung der Leistung (und des Mikroskops selbst) wurde beispielhaft der molekulare Lichtschalter $[Ru(bpy)_2(dppz)]^{2+}$. Neben vielen anderen interessanten Eigenschaften ist dieses Molekül bekannt dafür sich begierig an DNA zu binden. Es zeigt geringe Zellschädigung und hat eine langlebige rotverschobene Emission. Da das letztgenannte extrem empfindlich gegenüber des Lösungsmittels ist, ist das Molekül unter dem Namen "molekularer Lichtschalter" bekannt. Die lange Tradition der Forschergemeinde dieses Molekül und verwandte Ru(II)-polypridin Komplexe zu untersuchen, führte zu einer großen Anhäufung von Wissen, welches zu einer vollständigen Charakterisierung seiner spektroskopischen und elektrochemischen Eigenschaften führte. Obwohl sowohl die Menge an verfügbaren Daten für $[Ru(bpy)_2(dppz)]^{2+}$ als auch die Fülle an Experimenten welche zur deren Messung genutzt wurden, konzipierten und führten wir dennoch Schlüsselexperiemnte aus, welche gedacht sind Moleküle in einer Umgebung zu charakterisieren, welche in eukaryotischen Zellen gefunden werden können, da die Moleküle in einer Lösung untersucht wurden, welche einen Nukleus, die Zellmembran und das Cytosol imitierten. Demzufolge dienten diese Experimente als eine Referenz zu den mikrospektroskopischen Experimenten. Das Wissen über dieses Molekülsystem ist nicht ausschließlich auf den Bereich der physikalischen Chemie begrenzt, da es in lebenden und fixierten Zellen untersucht wurde, was Debatten auslöst z.B über die Aufnahme bei lebenden Zellen oder ob es überhaupt aufgenommen werden kann. In jeden Fall haben wir es genutzt um den Nukleus von lebensfähigen und fixierten HepG2 Zellen, von denen, relativ zu DAPI (Standard Nukleus Marker), starke Emissionssignale aufgenommen wurden, zu färben, um anschließend eine Vergleichsprüfung derübergangsabsorbtionsbildgebung mit der Emissionsbasierten konfokalen Laserscanning Mikroskopie, dem Goldstandard der modernen Mikroskopie bei Anwendungen bei in cellulo Experimenten in Biowissenschaften, durchzuführen. Es sollte erwähnt werden, dass es (meines Wissens nach) bis zum Zeitpunkt zu welchem die hier präsentierten Daten aufgenommen wurden, keine Berichte über Studien zu Pump-Probe mikrospektrokopischen Untersuchungen von zellulären Organismen existierten, welche mit Metallkomplexen behandelt wurden. Daher zeigt diese Arbeit eine neue Anwendung der Pump-Probe Mikrospektroskopie. Anschließend wurde demonstriert und etabliert, dass das TAM sowie die Pump-Probe Mikrospektroskopie Methode geeignet ist, mit $[Ru(bpy)_2(dppz)]^{2+}$ behandelte Zellen zu untersuchen. Dies beflügelte die Studie eine weitere Reihe von Molekülen zu erdenken, speziell konstruiert und synthetisiert um als Luminophor oder photoaktivierter Wirkstoff beim Einsatz des TAM zu dienen. Diese Gruppe von Molekülen zeigen eine höhere Aufnahme im Vergleich zu $[Ru(bpy)_2(dppz)]^{2+}$, welches ihren erhöt lipophilen Liganden zugeschrieben wird. Diese Gruppe beinhaltet $[(bpy)_2(Ru(tpphz)Ru(bpy)_2]^{4+}$,

$[Ru(bpy)_2ippy]^{2+}$ und Farbstoffe basierend auf Ruthernium(II)-Aren-Curcumin, welche vielversprechende Ergebnisse versprechen, wenn sie mit denselben Methoden angewendet werden. Es muss erwähnt werden, dass die beobachteten photoinduzierten Dynamiken in Referenzlösungen von den Beobachtungen in cellulo (in manchen Fällen erheblich) abwichen. Allerdings ist die photoinduzierte Natur wünschenswert, welche z.B. mit den mit den spektroskopisch beobachtbaren Absorbtionskinetik des Molekülsystems in Verbindung gebracht wird. Diese Aussage erscheint möglicherweise offensichtlich, wurde jedoch vor dieser Arbeit nicht nicht bewiesen. Ein wichtiges Ergebnis dieser Arbeit ist außerdem die gefundenen Abhängigkeiten der photoinduzierten Dynamiken welche das Molekülsystem während der Studie vom Zellbestandteil zeigte. Demnach zeigt sich das Prinzip des TAM als leistungsfähiges Werkzeug mit potentiellem Einsatz für Forschung und industrielle Pharmazie. Vom Einsatz der übergangsabsorbtionsbildgebung zur Untersuchung räumlicher Verteilungen und in einigen Fällen Bestandteilzuordnung des Molekülsystems in "Wirt"-mikrostrukturen Mikrostrukturen wurde bereits vor der vorgestellten Arbeit berichtet, da weder die übergangsabsorbtionsbildgebung noch die Behandlung von eukaryotischen Zellen mit Ru(II)-Polypyridin Komplexen von uns entwickelt wurde. Der hauptsächliche Beitrag und das Ziel dieser Arbeit war es ein Werkzeug, das TAM, und eine Methode zu liefern, welche gedacht ist, ultraschnelle photoinduzierte Dynamiken von Medikamenten in cellulo zu studieren und interpretieren. Das TAM ermöglicht es quantitativ zu bestimmen wo sich ein Medikament anreichert und wie sich seine photoinduzierten Dynamiken zeitabhängig in bestimmten Zellbestandteilen entwickeln. Letztgenanntes gibt die Möglichkeit darauf anzudeuten, wie sich das Molekülsystem unter Beobachtung in einer bestimmten Position der Zelle verhält. Folglich können sowohl die Anwendungsmöglichkeit, die wir, kreuzvalidiert und in manchen Fällen ergänzt durch emissionsbasierte Bildgebung, für das TEM aufgezeigt haben, als auch die entwickelte Methodik zur Erfassung und Interpretation der Daten als neu im Vergleich zur Literatur gesehen werden. Die selbstverständliche direkte Anwendung des TAM, ist sein Einsatz zur systematischen und mikrospektroskopischen Erforschung wohletablierter und charakterisierter zellularer Luminophore in cellulo, gefolgt von Untersuchungen von Molekülsystemen mit fehlenden strahlenden Zustand, erstellt zur Zerstörung von Pathogenen und erweitert um die Forschung mit anderen Metallkomplexen oder organischen Medikamenten. Außerdem eröffnet das TAM die Möglichkeit das Verständnis des Wirkmechanismus von Medikamenten in klinischen Studien zu erhöhen, welche heutzutage üblicherweise für Behandlungen eingesetzt werden. Im Bereich der Optik kann das TAM eingesetzt werden um die optische Auflösung nicht-linearer Mikroskope experimentell zu bestimmen und durch die Zusammenführung der nicht-linearen Methode mit hochaufgelöster Bildgebung (super resolution imaging).

Acknowledgements

I would like to thank the support, trust and teachings of Professor Dr. Benjamin Dietzek, who taught me the righteous way of a scientist. To Dr. Armando Pérez Leija, whom was to me a mentor and a friend during the time I spent in Jena; thank you for showing me the value of discipline and constancy in life. To Dr. Ramsés Gallegos Monterrosa who privileged me with his friendship and in addition showed me the importance of doing science with passion. I also want to acknowledge the teachings of the best experimentalist mentors I could have had: Prof. Dr. Jens Limpert, Dr. Denis Akimov and Dr. Torbjörn Pascher, thank you for all your support, patience and friendship. It is also important to thank all the people who gave me some knowledge, the people who supported me to carry out my research and to those who collaborated with me. Especially to Dar'ya Davydova, Dr. Tatiana Tolstik, Fisseha Bekele, Dr. Sandro Heuke, Dr. Nadine Vogler, Benita Göbel and all the members of the AGDietzek I had the priviledge to work with: thank you all. To the staff of the IPHT Jena and the FSU, the institutions where I became a scientist: many thanks. To my friends Fernando Rosales, José Medina and Viviana Sagredo for your unvaluable friendship and moral support thank you. To my aunts Patricia Pérez-Gallardo Dupont and Roxana De la Cadena Valenzuela, for all the love and experiences they gave me. And of course to my parents: Silvia Pérez-Gallardo Dupont and Alejandro De la Cadena Valenzuela, for their uninterrupted and unconditioned love and support, thank you.

Selbstständigkeitserklärung

Ich erkläre, dass ich die vorliegende Arbeit selbstständig und unter Verwendung der angegebenen Hilfsmittel, persönlichen Mitteilungen und Quellen angefertigt habe.

Mailand, Italien den...

Alejandro De la Cadena Pérez-Gallardo